Title

Covalent Conjugation of Active Proteins to Single-Walled Carbon Nanotubes

Author

Ledesma, Francis

Publication Date

2024

Peer reviewed|Thesis/dissertation

Covalent Conjugation of Active Proteins to Single-Walled Carbon Nanotubes

By

Francis Ledesma

A dissertation submitted in partial satisfaction of the

requirements for the degree of

Doctor of Philosophy

in

Chemical Engineering

in the

Graduate Division

of the

University of California, Berkeley

Committee in charge:

Professor Markita P. Landry, Chair
Professor David Schaffer
Professor Niren Murthy

Spring 2024

Covalent Conjugation of Active Proteins to Single-Walled Carbon Nanotubes

Francis Ledesma

Abstract

Covalent Conjugation of Active Proteins to Single-Walled Carbon Nanotubes

by

Francis Ledesma

Doctor of Philosophy in Chemical Engineering

University of California, Berkeley

Professor Markita P. Landry, Chair

Nanoparticles are nanometer-scale materials capable of interacting with biomolecules on various size scales from small molecules to oligonucleotides to proteins. Their unique ability to distribute throughout the body and internalize into cells has led to their recent use as signal transducers for analyte sensing and therapeutic cargo carriers. Current techniques for attaching biomolecular cargo to nanoparticles typically rely on affinity between the two species, especially noncovalent adsorption via hydrophobic interactions. Proteins in particular have complex tertiary structures that must be maintained for biosensing and delivery applications. This is difficult to achieve when attaching proteins to nanoparticles by noncovalent adsorption due to the propensity of proteins to denature and desorb in complex biological environments such as blood plasma. Additionally, the large variability among proteins and their affinity for nanoparticles makes it difficult to predict the successful generation of potential protein-nanoparticle systems. Control of the interactions between nanoparticles and proteins is thus crucial to the successful development of tools to understand and interface with biological systems.

Towards this end, exploring protein conjugation to single-walled carbon nanotubes (SWCNTs) could advance the study of nanoparticle-protein conjugates. SWCNTs have shown utility as biosensing signal transducers due to their intrinsic, photostable, and minimally attenuated fluorescence emission in biological environments. Furthermore, their small size and large surface area make them ideal vehicles for cellular cargo delivery. Several noncovalent protein-SWCNT constructs for sensing and delivery have been developed but are susceptible to instability and loss of function when applied in biological systems. Covalent conjugation of proteins to SWCNTs could mitigate these effects and produce stable constructs to monitor disease progression and deliver therapeutics.

This dissertation presents the development of an adaptable platform for the covalent attachment of proteins to SWCNTs for analyte sensing and protein delivery. We first optimized the platform and workflow by attaching a model enzyme, Horseradish Peroxidase, to SWCNTs for hydrogen peroxide (H_2O_2) sensing. We find that it is possible to maintain both intrinsic SWCNT fluorescence and peroxidase enzymatic activity via triazine-thiol-SMCC crosslinker chemistry, which are key to subsequent function as a sensor. The resulting sensor shows sensitive, stable, and repeatable fluorescence modulation when exposed to H_2O_2 in solution and immobilized on glass. After demonstrating the utility of the platform, we have applied this methodology to covalently

conjugate the CRISPR-Cas9 ribonucleoprotein to SWCNTs for delivery to cells for targeted gene editing. Using an *in vitro* DNA cleavage assay, we verified that Cas9 activity is maintained after SWCNT conjugation and dependent on crosslinker:protein ratio. This also suggests that the covalent conjugation platform is adaptable to other proteins, but reaction optimization should be completed every time to elucidate the optimal conditions for each protein.

The findings presented in this dissertation review the creation and optimization of a platform for the development of covalent protein-SWCNT constructs for increased stability and function in biological environments. Prioritizing covalent attachment of recognition elements and functional groups will lead to nanoparticle-based sensors and delivery vehicles with enhanced efficiency compared to previous efforts. Future directions of inquiry are also discussed and guidelines for efficiently exploring these new directions are summarized within.

This thesis is dedicated to my parents, Francisco and Shirley, for their unwavering love and support of their family. Thank you for giving us the world.

Table of Contents

List of Figures

List of Tables

Acknowledgements

"Even Superman has his Kryptonite." This quote, first told to me by my good friend TJ Famighetti in college, reminds us that if even the most powerful, virtuous, and courageous superhero in existence has a weakness and can be defeated, why on earth would we mortal humans to expect to be perfect in everything we do? It was a long journey for me to come to grips with this reality, fighting my perfectionist tendencies from kindergarten all the way through getting my Ph.D. now. I've gotten better about it over my time at UC Berkeley, and trust me, if I hadn't, I wouldn't have finished. I'm at a place now where giving my best effort is all I need to be happy, and getting to this point at all would not have been possible without a support system filled with many, many people who were always there for me, personally and professionally.

First off, I want to thank my PI and mentor, Professor Markita P. Landry. Thank you so much for your compassion, advice, and support over these past 5 years. I can't even begin to count how many times I've started off a research meeting with "I'm sorry I don't have as much data for you as I should" and you immediately responded with enough reassurance, understanding, and compassion that I left each meeting feeling better about myself and my progress than when I entered. You gave me total freedom to pursue my projects at my own pace, explore the directions that intrigued me, and helped me realize that "failed" experiments are not "bad" experiments, they're just results to learn from. Thank you for the endless support and for being the best PI I could have asked for.

I owe my gratitude to the Landry Lab members past and present as well for keeping my head above water when research was pulling me under. Thank you to everyone who was in the lab when I joined – Abraham Beyene, Darwin Yang, Gözde Demirer, Huan Zhang, Travis Del Bonis O' Donnell, Ian McFarlane, Eduardo Grandío, Sanghwa Jeong, Nat Goh, Chris Jackson, Frankie Cunningham, Jeff Wang, and Nick Ouassil. You all welcomed me with open arms and made me feel like part of the lab from Day 1. I'll never forget how much fun we had that first lab retreat! I want to give Linda Chio a special thank you for training me and basically giving me my research area in my first days of the lab, and I wish a global pandemic didn't cut that time short before you graduated. Speaking of global pandemic, I want to especially thank Rebecca Pinals for keeping me sane in lab (from 6 feet away with masks on of course!) during the early pandemic stages. It was a blast working with you and being bench buddies! I also want to thank Sarah Yang for being my mentor during my GSAC Presidency and being an outlet to voice frustrations and craft solutions with. I was and still am grateful to have you as a role model. I also must thank my fellow kiddos, Nicole Navarro, Madeline Klinger, and Josh Hubbard, for being the mischievous bunch that made me look forward to coming to lab every day and supporting me in all aspects of life. To those carrying on the lab legacy after me, Liz Voke, Henry Squire, Sophie Tomatz, Juliana Matos, Shoichi Nishitani, Jaewan Mun, Dabin Yim, Roxana Coreas, Owen Lin, and Kevin Ao, thank you for continuing to make the lab a second home and I wish you all the best in your scientific journeys. I want to particularly shoutout Jaquesta Adams, my crossword buddy, sensor subgroup sustainer, and Cöerner member protecting us from the Feds. Thank you for many years of laughs and hot takes. Thank you as well to Natsumi Komatsu for the K-pop lessons, occasional scientific discussion in between, and for being the only lab member taller than me. Special shoutout to my undergraduate mentees Bora Ozcan and Xiaoqi Sun for giving me the opportunity to pay forward some of the mentorship I received. I hope you learned as much from me as I did from you. During

my time in graduate school, there was so much paperwork and administrative hoops that I didn't have to jump through because of the tireless work of Sigrid Allen and Carlet Altamirano, and I am grateful for your support. In that vein, special thank you to Ruby Nelson for being the greatest lab manager of all time and keeping the lab running. I have never met someone as good at organizing people and plans as you and I thank you for being the backstop both in the lab and on the softball field.

Thank you to my qual and dissertation committee, Professors David Schaffer, Wenjun Zhang, and Niren Murthy for your feedback and guidance over the course of my time in graduate school. I also want to thank Professor Karthik Shekhar for being a fantastic instructor to serve as a GSI for. I learned so much from you about teaching and compassion, both virtually and in person over the two times we worked together.

I would be remiss in not thanking the other educators and mentors who helped me get to where I am. Thank you to Dan Chilowicz for being instilling a love of chemistry in me as a high-schooler. Mr. Chil helped me discover my love of science and education, giving me my first opportunities to help others learn and for that I am ever grateful. Thank you as well to Mike Rogers and Christopher Henry for giving me my love and appreciation of history. I grew tremendously as a person in your classes and learned how to think critically instead of accepting things at face value, skills that would help me tremendously in college and grad school. Similarly, I want to thank my undergraduate PI Professor Chris Alabi and my graduate student mentors Josh Walker and Michelle Sorkin. Thank you for giving me a chance to grow from a fledgling scientist who had never held a pipette to a Ph.D. holder. I also need to thank Professor T. Michael Duncan for giving me three chances to be your TA and learn what it means to be a good teacher. You supported me and my growth as an educator, helping me every step of the way as I began to develop my own style of teaching excellence and I am forever grateful. Thank you as well to my summer research mentors at UC Berkeley, Professor David Sedlak and Joe Charbonnet for their advice and support as I struggled to learn a whole new research field in 10 weeks. Thank you, Joe, for continuing to check in with me regularly even to this day. My fellow Ph.D. students have been great mentors to me as well, particularly Julie Fornaciari, Lorena Grundy, and Helen Bergstrom. Thank you all for your advice and support over the years both academically and personally.

They say you're only as good as the people around you, and I am very lucky to have had many good people as friends over the years help me grow as a person. To my high school best friends Nathan Santelli and Kevin Biernat, thank you for pushing me to be the best version of myself and giving me a reason to come back to Clifton for more tomfoolery. Thank you to all the friends who helped me as I struggled through college, especially TJ Famighetti, Andrea Clinch, Emma Renner, Kanha Matai, Liz Cantlebary, Daniel Pyrek, Sam Dimmer, Greg Bielat, Greta Sloan, Conner Parkinson, Blake Goodwyn, Dara Canchester, Miranda Kasher, Nathan Barr, Walter Johnsen, Hope McGovern, Amelia Sugianto, Olivia Young, Peter Haddad, and Ben Gassaway. That's a lot of people but I promise that you all significantly influenced my life for the better and I cannot thank you enough for that. Special thank you to Hannah Doyle for being the best backpacking co-guide ever and helping us climb Mt. Haystack safely. Thank you as well to my Crazy Creatures of Spring Buffet, Erik Lech, John Woltornist, and Ryan Wu. I wouldn't have done those all-nighters with anyone else. Shoutout to The Square as well, Shreya Nayar, Emma Mayer, and Ryan Wu. Thanks for making classes more fun than they had any right to be. Thank you to the 2017 NSF

REU cohort for a fantastic summer of memories, Chris Luthers, Haley Kodak, Emily Pujadas, Kassina Kim-Hayes, Angeline Chemel, Brenda Cruzy, Elijah Blank, Puneet Sanghera, Nick Reid, and Grayson Barker. Finally, thank you to my best friends Kara Guse and Joe Adas. We've been on so many adventures both in Ithaca and around the world and I can't wait for what shenanigans we get up to next.

I was lucky enough to meet many amazing people in graduate school that made the rough times not so rough. Thank you to the Cohort of 2019, especially Morgan Seidler, Josh Hahn, Darby Hickson, Salwan Butrus, Matt Dods, Kimberly Chan, and Ahmad Alkadri. I'll never forget our cohort trips and endless (mis)adventures. Thank you to the greatest Chemical Engineering Softball Team ever, the 2023 CoC Softball Champion Lewis Base Stealers for making summers even more fun than they normally are. Thank you to my two-time IM Ultimate Frisbee Champions Team Doug for letting me use my height to compensate for my lack of speed. Thank you to my volleyball team, the Ohlone Park Volleyball Club, for making the pandemic a little less lonely. Finally, thank you to the original Eddy Boys, Alec Ho, Matt Crafton, Zach Lipel, and Zach Hoffman. You welcomed me with open arms into your home and we made unforgettable memories at Edwards Street. There is no better group of people I could have spent a global pandemic stuck indoors with.

Lastly, I want to thank my family for their support throughout my life. I have a very large family, for which I am grateful, and I could not have done this without their love. Dad, Mom, Dylan, and Shesca, thank you so much for loving and supporting me as I have searched for my place in the scientific world, despite not knowing what I'm doing half the time. Thank you for giving me a loving family to return home to. Dad, thank you for always making sacrifices to help our family grow and thrive, taking us on trips around the world, and putting smiles on our faces all the while. Mom, thank you for always reminding us of how important family is, keeping us happy and healthy, and making sure we have everything we need. You both have sacrificed so much for our family and there is not enough money, gifts, or words we could give you to encompass how grateful we are. Dylan, thank you for continuing to be the brother I always wanted. I am excited for your future and all the adventures we have yet to embark on. Shesca, thank you for reminding me that I am old yet always keeping me young at heart. I'm looking forward to continuing seeing you grow into the amazing person you are. Finally, thank you to Alison Lui. You are my rock to cling on when the weather is stormy, my trampoline to bounce off when I fall down, and my sunlight through the trees as I climb the tallest mountains. I am so happy that we met and bonded over our love of volleyball, the outdoors, cooking, and music way back in those unprecedented times. Thank you for always challenging, grounding, and uplifting me throughout our Ph.D. rollercoaster. We've been through so much together in such a short amount of time, and even now I find myself bewildered at how far we've come together (can you believe we have a dog? I know he can't read but hi Freddie, I love you!). Your love of adventure, curiosity, and laughter fill me with joy and make me grateful for every day I get to spend with you. I don't know where life will take us next, but I feel excited and ready for any challenge that comes our way knowing you are on my team.

Chapter 1: Introduction

1.1 Nanoparticles for Biological Applications*

Nanoparticles (NPs) are nano-scale tailorable platforms that range in size from 1 to 100 nm and can be constructed from different materials such as polymers, metals, and lipids.[1] Since their length scale is on the order of many biologically-relevant molecules such as small-molecule drugs, hormones and proteins, and toxic byproducts, NPs have been investigated for a wide variety of biological applications including as drug-delivery vehicles and nanosensors for health and environmental diagnostics.[2–5] A broad range of NPs are available for these applications, but each comes with limitations. Such limitations should be considered when constructing a NP-based system for a particular application and these limitations can be overcome by leveraging the distinct advantages each NP class offers. For example, an ideal NP system for cargo delivery should employ facile cargo conjugation, protect its cargo from degradation *in vivo*, exhibit low toxicity and immunogenicity, be effectively uptaken by cells, provide stability and endosomal escape, biodegrade on a timescale that avoids accumulation, and release its cargo at the target location.[6] Similarly, an ideal NP system for analyte sensing should be stable over time, selective for its target analyte over other molecules, sensitive enough to detect low amounts present in the application system, and able to translate the detection of analyte to a detectable signal.[2]

Simultaneously achieving all figures of merit is challenging, thus NP design is typically approached by considering the application and optimizing for the features most important therein. Because NP structure is closely related to its advantages, the most commonly used NP classes are outlined in this section by discussing their structures, advantages, and limitations in the context of cargo delivery (Figure 1.1). However, most of these qualities are also applicable for designing biosensing systems as the application environments, such as cells, tissue, *in vivo*, environmental ecosystems, and food and beverage products, all require mitigation of toxicity and degradation for effective use.

* Portions of this section are adapted from Ledesma, F., Ozcan, B., Sun, X., Medina, S. M. & Landry, M. P. Nanomaterial Strategies for Delivery of Therapeutic Cargoes. *Adv Funct Materials* **32**, 2107174 (2022).

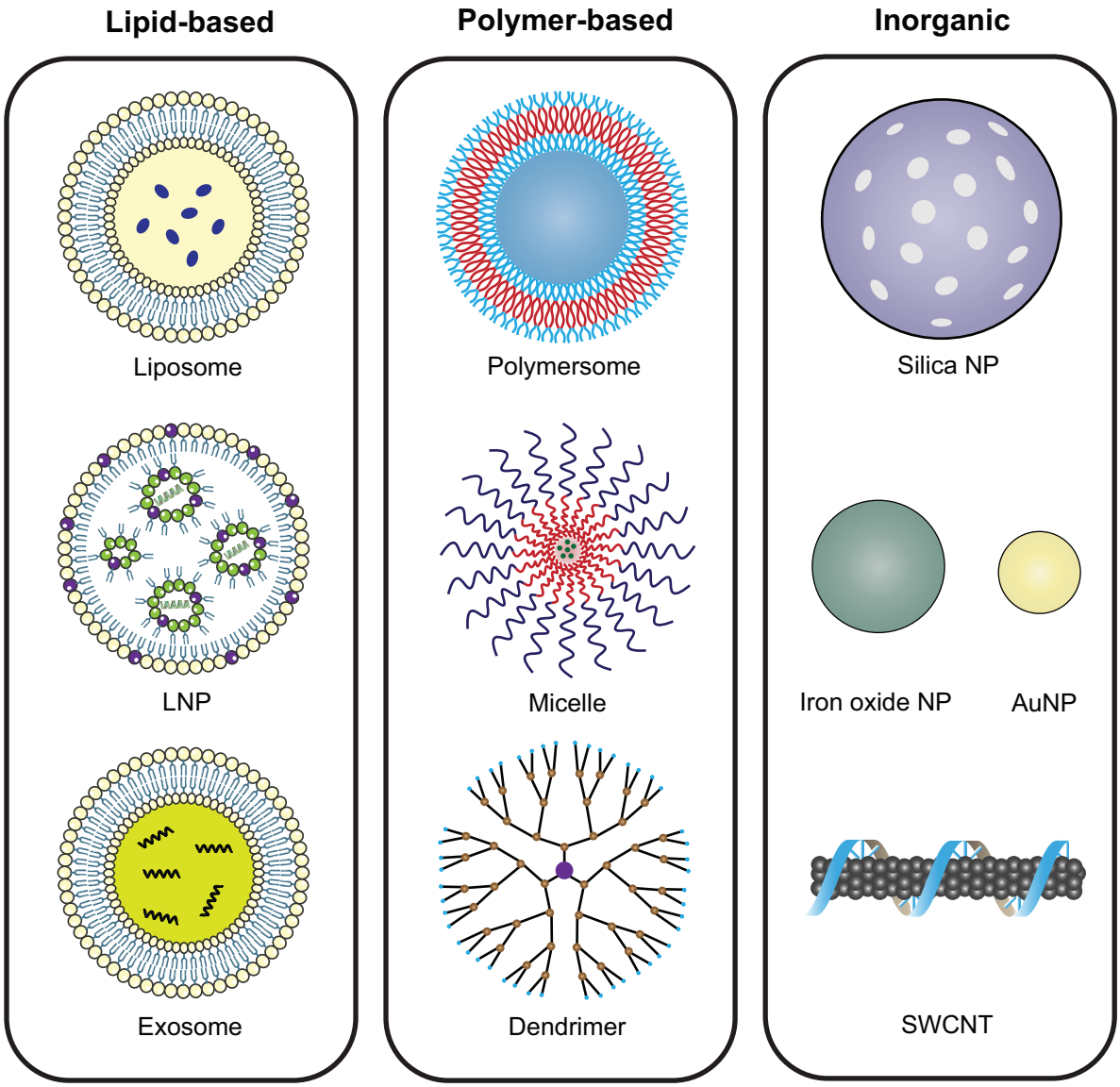

Figure 1.1. Schematic structures of NPs used for the delivery of small molecule drugs, nucleic acids, and proteins. Some images in this figure are adapted with permission from Servier Medical Art by Servier (http://smart.servier.com), licensed under a Creative Commons Attribution 3.0 Unported License.

1.1.1 Lipid-based NPs

Lipid-based NPs are the most broadly used NPs for delivery in mammalian systems, with several lipid NP-based drugs on the market.[7] Their advantages include high bioavailability, biocompatibility, biodegradability, low toxicity, self-assembly, ease of surface modifications, and ability to carry a wide range of cargos that vary in size. However, the main drawbacks associated with lipid-based NPs include low encapsulation efficiency and limited systemic delivery to locations other than the liver.[7]

Liposomes, one of the most widely used types of lipid-based NPs, measure ~30 nm through several micrometers. Liposomes are composed of a spherical assembly of phospholipid bilayers, providing the ability to simultaneously encapsulate hydrophilic, hydrophobic, and lipophilic cargo. Thus, liposomes are favorable for co-delivery of a broad spectrum of cargos such as proteins, oligonucleotides, and small molecules.[6,8] Their *in vitro* and *in vivo* stability can be improved using surface modifications involving the incorporation of ligands or polymers such as polyethylene glycol (PEG)[9] or chitosan.[10]

Lipid nanoparticles (LNPs), another subset of lipid-based NPs, range in size from 50 to 1000 nm and have structures similar to that of liposomes, but the main difference lies in the micellar structures formed in their cores. LNPs are typically composed of cationic or ionizable lipids that facilitate conjugation with cargo, phospholipids, and cholesterol that provide membrane stability, and PEGylated lipids that improve stability and extend circulation.[7,11] Although permanently-charged cationic lipids were developed in early systems to overcome low cargo encapsulation limitations, their permanent positive charge was found to cause high toxicity and immunogenicity.[12] More recently, ionizable lipids have been developed and offer a modular alternative to permanently-charged cationic lipids. The ionizable lipid core of LNPs remains neutral at physiological pH but becomes protonated in the acidic environment of endosomes, thus allowing both endosomal escape and reduced toxicity.[11–13] Such advantages make ionizable LNPs especially promising for nucleic acid delivery, including the co-delivery of functionally distinct nucleic acid therapies.[7,11,14,15]

Exosomes are nanosized (30-120 nm) extracellular vesicles that are naturally secreted by cells to facilitate intercellular communication. Exosomes are composed of a cell-derived lipid bilayer membrane that surrounds their hydrophilic core, which allows for encapsulation of hydrophobic and hydrophilic cargoes ranging from small molecules to oligonucleotides.[16] Exosomes are promising *in vivo* delivery vehicles due to their high biocompatibility, low immunogenicity, and intrinsic ability to cross biological barriers. However, the clinical translation of exosomes is limited by the lack of standardized techniques for their purification and challenges in their isolation from biological fluids.[16–18]

1.1.2 Polymer-based NPs

Polymeric NPs, a class consisting of natural and synthetic polymers, range in size from 1 to 1000 nm and are widely used as delivery vehicles. Additionally, some polymers are also used as surface modification tools. Cargo can be encapsulated in their core, entrapped in the polymer matrix, or chemically conjugated to the NP surface or to the polymer itself.[7] Therefore, the facile synthesis and functionalization of polymers enables control over the NP's characteristics and flexibility in the types of cargo that can be loaded and delivered. Similar to lipid-based NPs, polymeric NPs can load a wide range of cargo, including hydrophilic and hydrophobic compounds that vary in size from small molecules to macromolecules like proteins.[7] Other advantages of polymeric NPs include biocompatibility and biodegradability.[19] However, polymeric NPs are limited by toxicity risks that are caused by aggregation or the interaction of highly positively charged polymers with blood.[7,20]

Two common forms of polymeric NPs are nanospheres, which encapsulate cargo within their core and nanocapsules, which distribute cargo within their polymer matrix. Micelles are a type of polymeric NP that self-assemble to form nanocapsules with a hydrophobic core and hydrophilic coating to protect cargo and provide stability.[7] Dendrimers are hyperbranched globular polymers consisting of an atomic or molecular core in the center and tunable branches and functional groups on the surface, which allow precise control over size, shape, and surface chemistry for cargo conjugation.[6] Cargo can be loaded either by encapsulation or conjugation to the dendrimer surface. One type of dendrimer that is well-studied is polyamidoamine (PAMAM). PAMAM has protonatable amine groups that enable escape from endosomal degradation, simple and flexible encapsulation, non-immunogenicity, and suitability for oral delivery owing to enhanced penetration of the gut epithelial barrier.[6]

Other polymers can be used to form NPs for delivery, such as chitosan, polyethylenimine (PEI), polylactic acid (PLA), polyglycolic acid (PGA), and polylactic-co-glycolic acid (PLGA). Chitosan is a natural polymer that is mucoadhesive, highly biocompatible and biodegradable with low toxicity, has high affinity to cell membranes, facilitates endosomal escape, and can load a wide range of cargos such as nucleic acids, anticancer agents, proteins, and antibiotics. However, chitosan is limited by poor solubility due to its low protonation percent at physiological pH.[6,21] PEI is a cationic synthetic polymer with a high positive charge that makes it favorable for the delivery of negatively charged drugs, nucleic acids, and bioactive molecules, and allows efficient cellular uptake. The main drawback associated with PEI is that its high positive charge leads to toxicity because negatively charged components in blood could form aggregates with PEI. Therefore, to find the balance between efficiency and toxicity, a trending approach is to coat PEI surfaces with PEG, chitosan, or other passivating molecules.[6] Other synthetic polymers that can form NPs include PLA, PGA, and PLGA, which have similar properties and advantages including high biocompatibility and biodegradability.[6] In particular, PLGA offers flexibility through adjusting its lactic acid to glycolic acid ratio.[22] Another polymeric NP type is polymersomes, which are artificial vesicles composed of amphiphilic block copolymers, resembling the structure of liposomes. Polymersomes are reported to have improved stability and cargo-retention efficiency, making them effective vehicles for the delivery of therapeutics to the cytosol.[7]

1.1.3 Inorganic NPs

Inorganic NPs are mostly used for research purposes in sensing and imaging and are sparsely used in clinical applications due to their inability to biodegrade. Inorganic NPs typically measure between ~2-100 nm, with advantages including tunable optical, magnetic, and electric properties in addition to facile modification of their size and geometry.[7] Major drawbacks associated with inorganic NPs besides their non-biodegradability include low as-synthesized solubility and toxicity risks arising from the nature of their constituent heavy metals. Due to the toxicity risks associated with inorganic NPs, only biodegradable and nontoxic inorganic NPs are suitable for *in vivo* delivery purposes, whereas the unique optical properties of each inorganic NP can be explored in imaging and sensing. Iron oxide NPs, silica NPs, gold NPs (AuNPs), and carbon-based NPs such as carbon nanotubes (CNTs) are the most common nanoparticles of this class.

Iron oxide NPs comprise the majority of FDA-approved inorganic NP-based therapeutics.[7] Favorable properties of iron oxide NPs include biodegradability, biocompatibility, and unique

magnetic properties.[22–24] Iron is an essential trace element, so iron transport pathways and iron homeostasis are well-understood, which leads to greater confidence in its low toxicity relative to other inorganic NPs whose toxicity and biodegradability are less understood.[22]

Silica NPs also exhibit biodegradability and low toxicity, but the unique advantage of silica NPs lies in their excellent tunability in physical features such as size (surface area and volume), shape, porosity (mesoporous silica NPs), and surface modifications such as conjugation to targeting ligands or imaging agents. Such flexibility in the potential physical and chemical modifications make silica NPs favorable for carrying various types of cargo.[23,25,26] However, the main limitation of silica NPs include a lack of understanding of their long-term stability *in vivo*.[23]

AuNPs are among the most studied inorganic NPs because of their unique optical and photothermal properties (arising from free electrons on the surface) that can be tailored through modifications in size, shape, structure, and composition.[7] While AuNPs are not biodegradable,[27] their inherent inertness is believed to result in low toxicity.[23] Concerns regarding long-term biocompatibility and accumulation-based toxicity limit the use of AuNPs.[23,28]

Other emerging inorganic NPs include metal-organic frameworks (MOFs) and quantum dots (QDs), particularly graphene QDs. MOFs are crystalline porous coordination polymers that are composed of inorganic metal subunits linked to organic ligands. As a result of their large surface area, highly ordered structure, and easily tunable pore size and shape, nano-sized MOFs offer flexibility in loading a wide range of cargoes.[29,30] QDs are inorganic semiconducting nanocrystals with high fluorescence intensity and photostability as well as broad excitation and narrow emission spectra, which make QDs especially promising for *in vivo* imaging. When integrated into drug delivery systems, QDs can provide real-time tracking *in vivo*. However, like most inorganic NPs, they are limited by their non-biodegradability and toxicity.[31] Graphene QDs are an attractive alternative to conventional QDs for delivery purposes because they maintain the favorable optical properties of QDs while simultaneously offering improved mechanical strength, greater biocompatibility, and lower toxicity.[32]

While this large library of NPs has been developed for delivery of various cargo to cells, not many are simultaneously suitable for sensing applications. Lipid- and polymer-based NPs exhibit good biocompatibility but require external signal transduction mechanisms, such as fluorescent dye molecules, to transduce or communicate the binding of an analyte. Inorganic NPs are best suited for this purpose, relying on a variety of intrinsic signal transduction modes such as aggregation, colorimetry, and fluorescence. In particular, single-walled carbon nanotubes (SWCNTs) are an interesting class of inorganic NPs that can serve as both cargo delivery vehicles and biosensing platforms owing to their unique physical and optical properties such as intrinsic fluorescence, high surface area, high mechanical strength, and electrical and thermal conductivity.[33]

1.2 Single-Walled Carbon Nanotubes as Versatile Nanoparticles

After being discovered by Ijima and Ichihashi in 1993, SWCNTs have emerged as a versatile NP class for both cargo delivery and optical biosensing.[34,35] For example, SWCNTs have shown successful facilitation of both plasmid DNA and RNA delivery to plants while protecting cargo from degradation and avoiding direct cellular toxicity.[36,37] SWCNTs have also been successfully

leveraged as optical biosensors for a variety of relevant biological analytes including dopamine, insulin, and the SARS-CoV-2 virus.[38–40] These applications rely on the unique physical and optical properties of SWCNTs, including their high-aspect ratio for plant cell wall penetration, high-surface area for cargo loading, and intrinsic near-infrared fluorescence emission for signal transduction of analyte sensing.[33] These beneficial qualities motivate further investigation of these NPs for biological applications.

Chemically, SWCNTs are carbon allotropes composed of a cylindrically-rolled graphene sheet (one plane of covalently bound sp^2-hybridized carbon atoms). With average lengths of 1 μm and diameters of 1 nm, these NPs can be considered essentially one-dimensional (Figure 1.2a). The direction of rolling along the graphene sheet imparts handedness or chirality to SWCNTs, denoted by two integers (n,m) depending on the vector direction, v (Figure 1.2b). Depending on their chirality, SWCNTs experience varying electronic band structures that enable them to be metallic, conducting, or semiconducting in nature.[41,42]

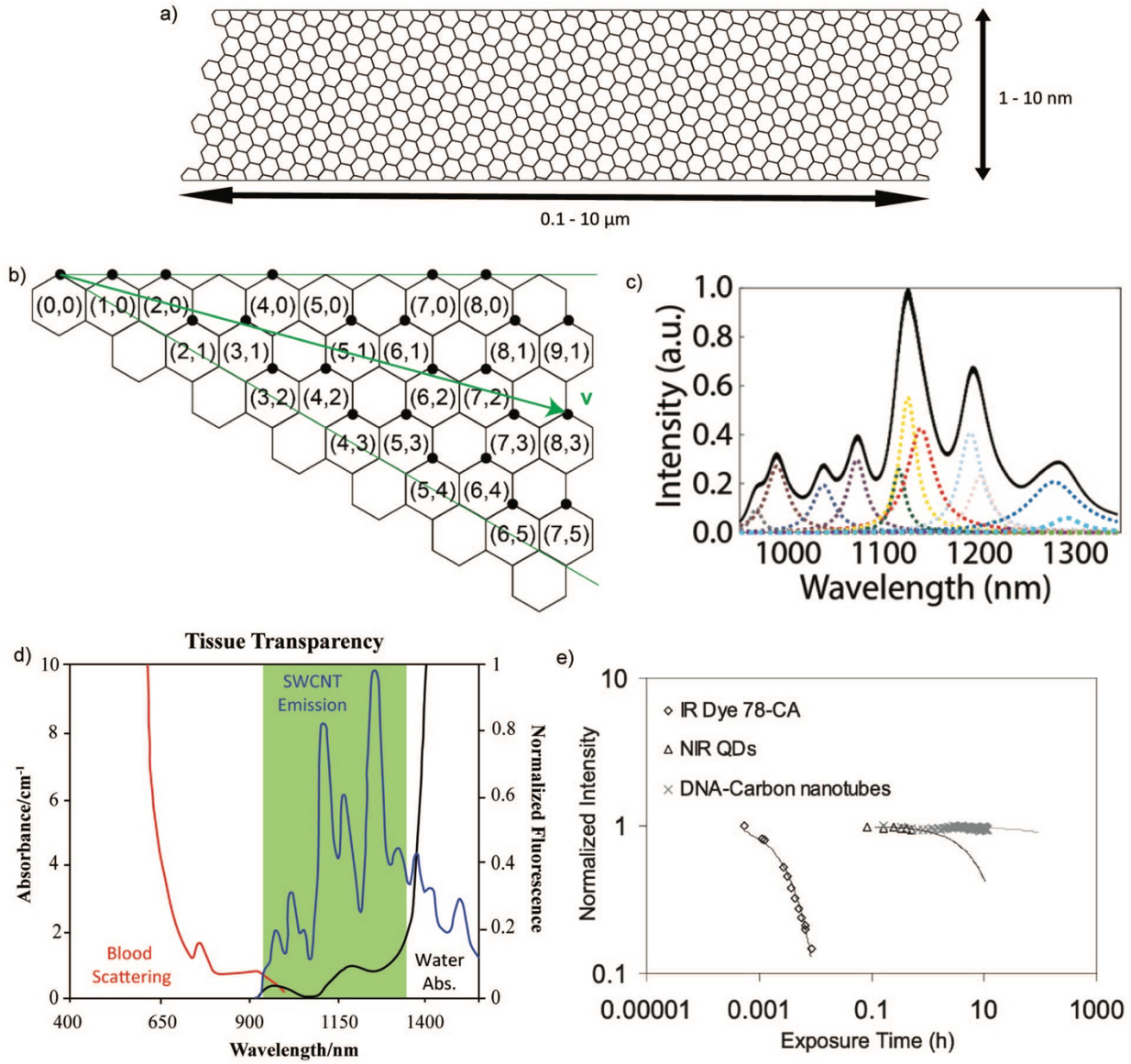

Figure 1.2. Schematic depiction of SWCNT and their advantageous properties. (a) SWCNTs consist of a cylindrically-rolled sp^2-hybridized hexagonal carbon lattice with an aspect ratio that renders them one-dimensional. (b) Semiconducting SWCNT chirality diameter and electronic natures are dependent on the vector rolling direction from (0,0). (c) Mixtures of semiconducting SWCNT exhibit an overall nIR fluorescence emission spectra (black) composed of the sum of all SWCNT single chirality emissions present in the sample (dotted). (d) SWCNT fluorescence in the nIR range (850-1350 nm) exists between the wavelengths at which blood scatters and water absorbs. This window renders SWCNT tissue-transparent and thus ideal for *in vivo* imaging applications. (e) SWCNTs (x) show excellent photostability compared to other IR fluorophores like dye molecules (diamond) and quantum dots (triangle), maintaining their fluorescence intensity over 10 hours of exposure without photobleaching. Portions of this figure adapted from Boghossian, A. A. *et al.* Near-Infrared Fluorescent Sensors based on Single-Walled Carbon Nanotubes for Life Sciences Applications. *ChemSusChem* **4**, 848–863 (2011).

These differences in band-gap energies among SWCNT chiralities affect their fluorescence, as SWCNT fluorescence is excitonic in nature.[43,44] Briefly, the semiconducting nature of SWCNTs renders the valence electrons in the sp^2-hybridized lattice mobile and excitable to a higher energy state by visible light. When external photons excite an electron to the higher energy state, it creates an exciton, which is composed of the excited electron and the hole in the valence shell it leaves behind, bound by Coulombic attraction. As this excited electron decays from its higher energy state and combines with the hole, energy is released in the form of fluorescent emission in the near infrared (nIR) range from 850-1350 nm. Since SWCNT band-gap energies vary by chirality, the wavelength of fluorescence emission varies accordingly (Figure 1.2c). A sample of pure chirality SWCNT thus emits fluorescence at a single wavelength and a mixture of SWCNT chiralities results in several emission peaks over the nIR range. In addition to chirality, SWCNT fluorescence is also influenced by the dielectric constant of the surrounding medium and the presence of charged or redox active molecules near the SWCNT surface, shifting the emission wavelength or enhancing/quenching emission intensity.[33,45] The modularity of SWCNT fluorescence in this manner enables its use as a signal transducer in various sensor applications when paired with molecular recognition elements to selectively bind analytes of interest.

Uniquely, SWCNT fluorescence emission is intrinsic to the SWCNT itself, requiring no external moieties to produce the signal. The wavelength range of SWCNT emission also falls in a window of biological relevance, being greater than the wavelengths at which blood scatters light and lesser than the wavelengths at which water absorbs light (Figure 1.2d). These properties render SWCNT tissue-transparent, enabling their use for *in-vivo* nIR sensing. Furthermore, SWCNT show excellent photostability, maintaining their fluorescence emission intensity over the course of 10 hours without photobleaching (Figure 1.2e). This enables longer use applications for SWCNT-based sensors compared to other fluorescent molecules like IR dyes and quantum dots, which photobleach quickly in comparison. Altogether, these advantageous properties make SWCNT an ideal NP for sensor and cargo delivery.

1.3 SWCNT Functionalization for Sensing and Delivery

Towards these ends, previous strategies for generating SWCNT-based constructs for cargo delivery and sensing have leveraged nonspecific adsorption of cargo or sensing modalities to the hydrophobic SWCNT surface that often rely on compatibility between the cargo and SWCNT or engineering new molecular recognition elements. For example, the hydrophobic surface of SWCNT typically causes them to aggregate in aqueous environments and prevents their use in cellular systems. However, this surface feature can be harnessed to noncovalently adsorb biomolecules directly to the SWNCT surface such as small interfering ribonucleic acids (siRNA), taking advantage of π-π stacking interactions between the RNA bases and the SWCNT sp^2-hybridized lattice to produce stable SWCNT-RNA constructs in aqueous solution.[37] These constructs can then be delivered to plant cells and show greater targeted gene knockdown than delivering the siRNA alone. Furthermore, plasmid DNA has been successfully attached to SWCNTs and delivered to plant cells by leveraging electrostatic charge interactions between negatively charged plasmid DNA and positively charged poly-ethylen-imine (PEI) attached to the SWCNT surface.[36]

Similarly for sensing applications, molecular recognition elements have been adsorbed to SWCNTs to selectively bind analytes of interest and modulate SWCNT fluorescence to signal successful binding. Many recognition element options have been demonstrated for SWCNT, including single-stranded DNA (ssDNA) to both disperse SWCNT in aqueous solution via π-π stacking and bind analytes like dopamine and serotonin, two important neuromodulators for brain activity.[38,45,46] Proteins have also been demonstrated as viable molecular recognition elements, leveraging the natural affinity of proteins like enzymes, receptors, and antibodies for their substrates to selectively bind analytes and subsequently modulate SWCNT fluorescence. For example, the ACE2 cell surface receptor can be noncovalently adsorbed to ssDNA-dispersed SWCNTs to generate a nanosensor for the SARS-CoV-2 Spike protein, enabling rapid point-of-care COVID diagnostics.[40]

However, these examples of SWCNT-based constructs succeeded in performing their intended function due to the biomolecules in question being amenable to noncovalent attachment to SWCNTs. In the case of cargo delivery, π-π stacking and electrostatic attraction work for RNA, DNA, and plasmid delivery, but would not be reliable methods for attaching other cargo such as small molecule drugs for cytotoxicity or large proteins like the CRISPR-Cas9 ribonucleoprotein (Cas9 RNP) for gene editing. It is possible that some molecules could be adsorbed to SWCNTs via hydrophobic interactions if they feature hydrophobic groups/pockets, but this is not a guaranteed possibility for every cargo and requires extensive and costly low-throughput screening to identify molecules amenable to attachment. Thus, non-covalent adsorption is not a generalizable strategy when designing SWCNT-based cargo delivery. Additionally, delivery of non-specifically adsorbed cargo via SWCNT could suffer from a lack of stability in complex biological environments such as in the plant cytosol or mammalian blood stream, leading to the premature desorption of cargo from the SWCNT and loss of efficacy.

In the case of sensor development, similar limitations exist when relying on noncovalent adsorption of recognition elements like DNA and proteins to the SWCNT surface. For example, directed evolution can be performed on ssDNA sequences to find those that effectively bind to both SWCNT and the analyte of interest, but these processes require extensive time and labor to perform.[46] For protein recognition elements, each protein exhibits differing net charge states at various pH values, requiring extensive screens of conditions for each protein of interest to be adequately adsorbed to the SWCNT surface. Furthermore, some proteins contain large hydrophobic pockets of amino acids within their core, which could unintentionally interact with the hydrophobic SWCNT surface after adsorption, causing the protein to denature and lose its natural affinity for the target analyte.

On the other hand, a generalizable platform for covalent attachment of biomolecules to SWCNTs could overcome these limitations. Rational design of conjugation sites on the biomolecule could remove the dependence on favorable biomolecule properties for successful attachment and avoid unintended protein denaturing. Stable covalent bonds between SWCNT and the biomolecule would mitigate biomolecule desorption in the intended application environment, ensuring constructs remain stable and active in complex biological fluids. These principles would shift SWCNT construct design away from extensive screening and towards rational design, eliminating the need for costly and labor-intensive screening to identify good molecular recognition elements and conditions for cargo loading.

1.4 Scope of Dissertation

This dissertation will describe a flexible platform for generating SWCNT constructs with covalently-bound proteins for biological applications, using Horseradish Peroxidase (HRP) as a model protein for platform development. Chapter 2 will discuss the motivation and chemical strategy for covalent-SWCNT conjugation of HRP. Chapter 3 will detail various characterization techniques available to validate successful conjugation of HRP while maintaining both SWCNT characteristic properties and HRP enzymatic activity. Chapter 4 will discuss the performance of the resulting nanosensor in various form factors and propose a mechanism by which the sensor operates. Chapter 5 will demonstrate the utility of the platform by extending it towards other complex proteins for further nanosensor and cargo delivery applications. Finally, Chapter 6 will summarize the conclusions from developing the platform in Chapters 2-5 and suggest routes for further investigation enabled by the platform.

Chapter 2: A Platform for Covalent SWCNT-Protein Conjugation[†]

2.1 Chapter Abstract

Single-walled carbon nanotubes (SWCNTs) are desirable nanoparticles for sensing biological analytes due to their photostability and intrinsic near-infrared fluorescence. Previous strategies for generating SWCNT nanosensors have leveraged nonspecific adsorption of sensing modalities to the hydrophobic SWCNT surface that often require engineering new molecular recognition elements. An attractive alternate strategy is to leverage the pre-existing molecular recognition of proteins for analyte specificity, yet attaching proteins to SWCNT for nanosensor generation remains challenging. Towards this end, we detail previous strategies for developing SWCNT-based nanosensors, introduce our platform for covalent protein-SWCNT nanosensor generation, and outline techniques for assessing the viability of our model protein, Horseradish Peroxidase (HRP), for optimizing and developing this platform. We demonstrate successful singular SMCC functionalization of HRP for conjugation to SWCNTs by QTOF-MS analysis, maintained SWCNT sp^2-hybridized lattice integrity upon HRP functionalization by characteristic absorbance and fluorescence peaks, minimal free HRP in the final nanosensor product after purification by SDS-PAGE and UV-Vis-IR absorbance of purification flowthroughs, and negligible nonspecific adsorption of HRP to dispersed SWCNT by a corona exchange dynamics assay. This platform can be extended to any proteins of interest and followed to ensure successful nanosensor generation.

2.2 Chemical Strategies for Development of Protein-SWCNT Sensors

Single-walled carbon nanotubes (SWCNTs) possess unique optical and physical properties that make them attractive materials for biomedical applications.[34] In particular, their intrinsic photoluminescence in the near-infrared (nIR) region and lack of photobleaching are ideal traits for *in vivo* and *ex vivo* sensing and imaging in biological systems.[47,48] Another advantage of SWCNTs as nanosensors is the diversity of functionalization that add synergistic functions to the SWCNT conjugates. For instance, the functionalization of SWCNTs with biomolecules, such as single-stranded DNA (ssDNA), creates a corona phase at the proximity of SWCNT surfaces which can interact specifically with analytes of interest, resulting in modulation of the SWCNT optical signal.[49] Owing to their sequence modularity, various ssDNA sequences have been identified to play this corona phase molecular recognition (CoPhMoRe) role through screening for selective recognition of target molecules.[50] Furthermore, ssDNA can be evolved to have a selective interaction with an analyte through systematic evolution of ssDNA ligands by exponential enrichment.[46] While these ssDNA-SWCNT conjugates have shown promising analyte-specific fluorescence signal modulation, the platform fails to guarantee nanosensor generation for a specific analyte of interest as the molecular recognition element of these nanosensors is not rationally designed.

[†] Portions of this chapter are adapted from Ledesma, F. *et al.* Covalent Attachment of Horseradish Peroxidase to Single-Walled Carbon Nanotubes for Hydrogen Peroxide Detection. Preprint at https://doi.org/10.1101/2023.12.14.571773 (2023).

Researchers have pursued the development of semi-rationally designed polymer-SWCNT conjugates to better develop nanosensor generation for a particular analyte. For example, Bisker *et al.* used a small phospholipid library screen to identify the phospholipid-PEG polymer DPPE-PEG(5000) to selectively recognize fibrinogen proteins with an 80% decrease in SWCNT fluorescence intensity upon addition of fibrinogen protein.[51] Similarly, Bisker and colleagues identified another PEGylated lipid, C_{16}-PEG(2000)-Ceramide, to serve as a recognition element for SWCNT-based insulin nanosensors with a turn-off response of around 60%.[39] Though these approaches successfully demonstrate CoPhMoRe sensing of their target analytes, they still require labor-intensive screens of similar polymer coating libraries to identify the optimal candidate for use as a molecular recognition element. Another approach for polymer-SWCNT nanosensors involves the use of synthetic peptide mimics named peptoids, which feature N-substituted side chains that confer both resistance to protease degradation and sequence tunability to rationally design molecular recognition. Chio *et al.* demonstrated the utility of these polymers by designing a small peptoid library and identifying a peptoid with both hydrophobic anchor sequences to bind to the SWCNT surface and loops of side chains designed to selectively bind the target protein Wheat Germ Agglutinin.[52] While this system successfully showed the ability to rationally design polymer-SWCNT nanosensors, the need for extensive library screens to identify successful molecular recognition elements remains a limitation to using pre-existing molecular recognition elements for nanosensor development. Overall, there are several advantages of polymer-SWCNTs for nanosensor development, including the development of nanosensors for which there exist no natural molecular recognition elements and the tunability of their selectivity and sensitivity profiles often achievable with more extensive screening.

Direct attachment of known molecular recognition elements such as proteins to SWCNTs present an orthogonal method for nanosensor generation that can circumvent some of the drawbacks of polymer-SWCNT screening, including time and cost of screening for nanosensor sensitivity, limited nanosensor selectivity, and less straightforward mechanistic function of the resulting nanosensor. Given their natural affinity for binding a target analyte, proteins are often the most readily available molecular recognition elements with which to develop nanosensors through protein-SWCNT conjugation.[53] While protein-SWCNT nanosensors can be rationally designed to detect or image a variety of biomarkers, the major drawback is that protein attachment to SWCNTs often compromises protein stability or SWCNT fluorescence.[5,45,54]

Traditionally, protein-SWCNT conjugates have been prepared by non-covalent approaches.[55] These methods typically rely on physical adsorption of the hydrophobic domains of proteins to SWCNT surfaces. For example, ultrasonication of SWCNT and protein[56] or dialysis-based ligand exchange[57] facilitates the non-specific adsorption of proteins to SWCNT surfaces. These non-covalent approaches, however, are dependent on the nature of the proteins which leads to varying levels of adsorption; thus, they are not generalizable.[58] Moreover, non-covalent attachment is often accompanied by conformational changes in the proteins, leading to the loss of their biological functions.[55] For example, Palwai *et al.* reported a complete loss of enzymatic activity of horseradish peroxidase (HRP) five days after immobilization on SWCNT.[59] A random alignment of the proteins on SWCNT may also reduce the efficiency of their biological activities, even if conformational stability is maintained. Therefore, non-covalent approaches are not a generalizable approach to developing protein-SWCNT nanosensors.

In this regard, covalent functionalization of proteins to SWCNT promises better stability and controlled alignment of the conjugated proteins.[60,61] However, covalent functionalization of SWCNT for sensing and imaging applications has been challenging because covalent bonds can introduce unintentional sp^3 defects into the sp^2 SWCNT lattices. While certain engineered SWCNT defects are used to shift SWCNT fluorescence for defect-based sensing, when introduced unintentionally, these defects often attenuate or fully eliminate the optical transitions in SWCNTs that drive SWCNT photoluminescence.[62,63] On the other hand, recent reports have shown successful covalent conjugation of proteins and peptides to SWCNTs while preserving their optical properties. For example, it has been shown that minimal introduction of quantum defects can preserve or even enhance the photoluminescence of SWCNTs.[64,65] Following these findings, Mann *et al*. developed a protocol to covalently conjugate proteins to SWCNT by controlling the density of quantum defects.[66,67] An alternative approach is to covalently functionalize SWCNTs without introducing sp^3 defects using azide-based conjugation.[68,69] Since the azide-based covalent bonds do not introduce an sp^3 defect by re-aromatizing the sp^2 lattice, this approach has a significantly higher degree of freedom in the density of functionalization compared to the approaches that use quantum defects. Recently, we have applied this chemistry to develop a versatile protocol to covalently functionalize SWCNTs and showed the potential of this chemistry to maintain analyte-specific responses of previously-reported nanosensors.[70]

2.3 HRP as a Model Protein for SWCNT Conjugation Platform Development

With the goal of covalent protein conjugation to SWCNTs for sensor development, many candidates for a model protein exist. An ideal model protein for development of this strategy should be amenable to the desired conjugation chemistry, small enough in molecular weight to be easily purified from SWCNTs, show minimal nonspecific adsorption to SWCNTs to confirm successful covalent conjugation, and bind an analyte of biological relevance. Thus, we are seeking a protein that achieves these figures of merit to best optimize and demonstrate the utility of this platform. In this regard, we employ Horseradish Peroxidase (HRP) as a model protein for the detection of hydrogen peroxide (H_2O_2). H_2O_2 is a critical component of reactive oxygen species (ROS) that play a pivotal role in many industrial and biological processes including ecosystem regulation in surface water, sterilization in food and beverage products, and cellular oxidative stress and signaling.[71,72] Consequently, developing fluorescent nanosensors for H_2O_2 that can be used for hydrogen peroxide detection or imaging is valuable, particularly non-photobleaching probes.

To synthesize our nanosensors, we first covalently modified unfunctionalized (pristine) SWCNTs with the azide-based triazine approach as previously reported (Figure 2.1).[68,70] Briefly, we reacted pristine SWCNTs with cyanuric chloride and sodium azide to produce high density triazine-labelled SWCNTs (Trz-H-SWCNTs) with minimal quantum defects, maintaining intrinsic SWCNT optical properties like nIR fluorescence emission. Trz-H-SWCNTs were further functionalized with the amino acid cysteine in the presence of triethylamine. Nucleophilic substitution of the solvent-exposed chlorines on the triazine handles with the primary amine of cysteine produced thiol-functionalized SWCNTs (SH-SWCNTs).

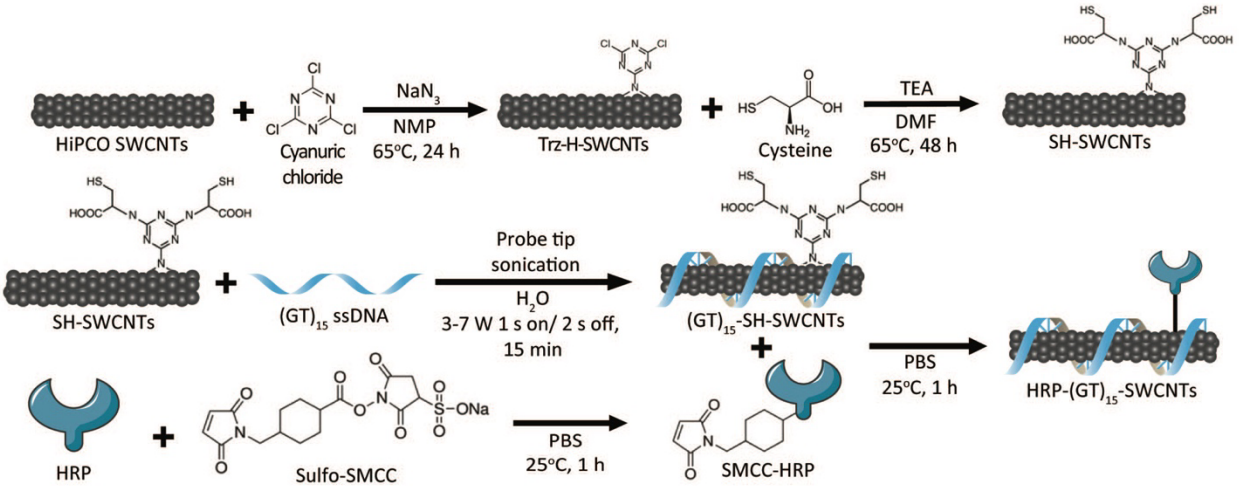

Figure 2.1. Synthesis of HRP-$(GT)_{15}$-SWCNT nanosensors. Synthesis scheme for nanosensor was performed according to previously established protocols. The SMCC:HRP ratio was optimized for single maleimide addition and reaction time and temperature were selected according to manufacturer protocol. Excess reactants were filtered away after each step and the final product was diluted back to the starting reaction volume.

These SWCNTs maintained their optical properties as shown by the preservation of characteristic absorbance (Figure 2.2a) and fluorescence (Figure 2.2b) peaks. Notably, the choice of cysteine for functionalization was made in part due to Sulfo-SMCC being chosen as the crosslinker for this protein-SWCNT conjugation platform. This crosslinker is optimal for this conjugation scheme as it features two orthogonal functional groups: an N-hydroxysuccinimide-ester group (NHS-ester) that first reacts with solvent-exposed primary amines on HRP and a maleimide group that subsequently forms a stable covalent bond with free thiol groups on the SWCNT. This stepwise order of crosslinking afforded by Sulfo-SMCC helps minimize unwanted side reactions and imparts the flexibility of extending this platform to conjugate other proteins with exposed primary amines with the same SH-SWCNT sample.

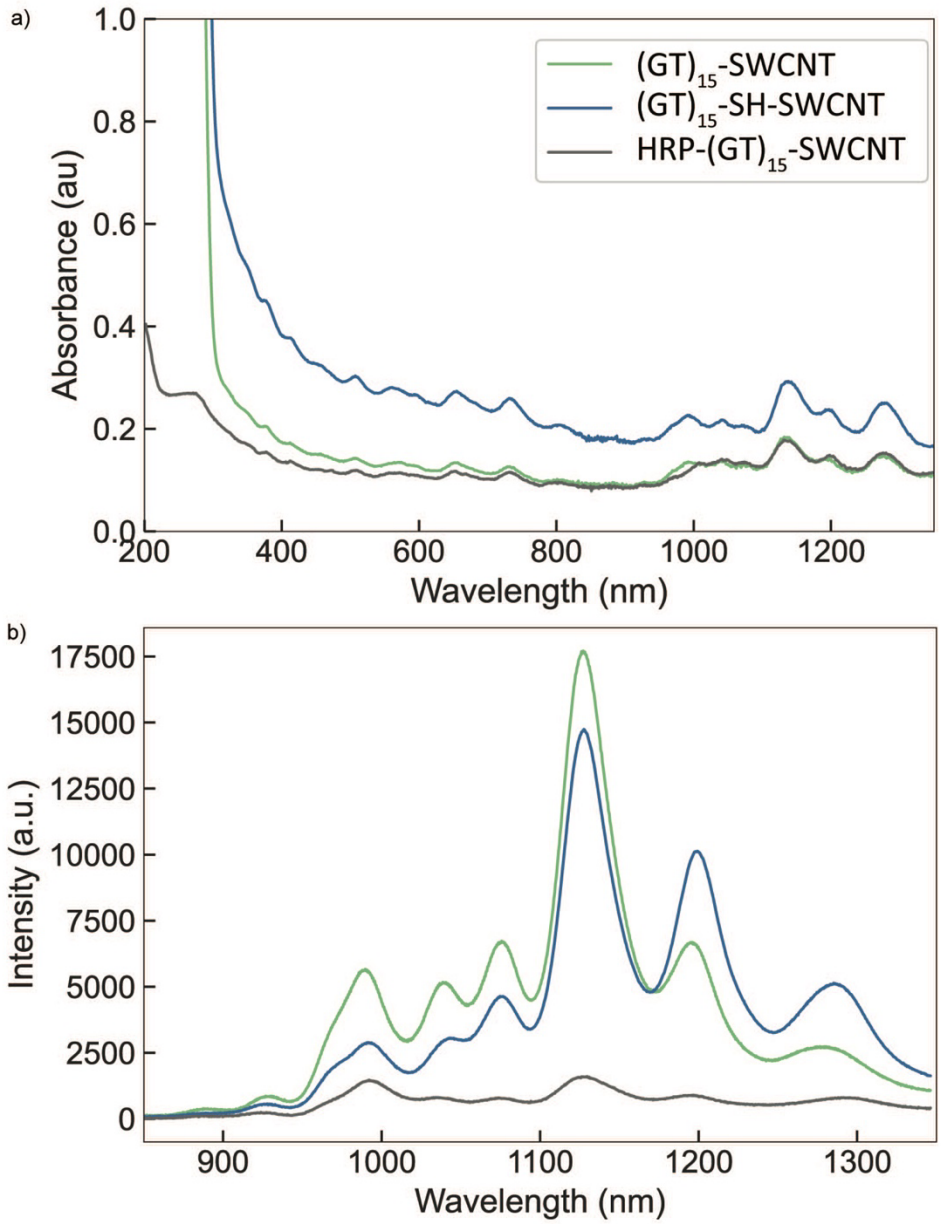

Figure 2.2. UV-Vis-IR absorbance and nIR fluorescence characterization of HRP-$(GT)_{15}$-SWCNT nanosensors. (a) Absorbance spectra of $(GT)_{15}$-coated SWCNTs along the nanosensor synthesis route show maintained characteristic peaks. (b) nIR fluorescence baselines for the samples in (a) show preservation of SWCNT intrinsic fluorescence throughout synthesis.

We reacted the NHS-ester group of Sulfo-SMCC with solvent-exposed primary amines on HRP to form maleimide-functionalized HRP (SMCC-HRP) for subsequent conjugation to SH-SWCNTs. There are 6 solvent-exposed primary amines in the form of lysine residues on the surface of HRP, 3 of which are the most amenable to crosslinker functionalization (K232, K241, K174).[73] The other 3 lysines are either involved in salt bridges (K65 and K149) or barely exposed to solvent (K84).[74] As such, we expected to add between 1 and 3 SMCC crosslinkers to HRP under these reaction conditions. Optimizing the SMCC:HRP ratio during the conjugation reaction via QTOF-MS shows successful addition of 1 SMCC for a 10:1 SMCC:HRP ratio and the appearance of dual

functionalization at a higher ratio of 20:1 (Figure 2.3). As all 3 potential lysines are not located within the binding pocket of HRP and subsequent activity assays show negligible loss in enzymatic activity post-SMCC functionalization, the exact identity of which lysine is modified was left unknown, though previous literature suggests the most reactive lysine of the potential candidates is K232.[74] Thus, we concluded that the optimal ratio of SMCC:HRP is 10:1 as it leads to singular functionalization, though this ratio would need re-optimization for any new protein to be used with this strategy depending on its number and availability of solvent-exposed primary amines.

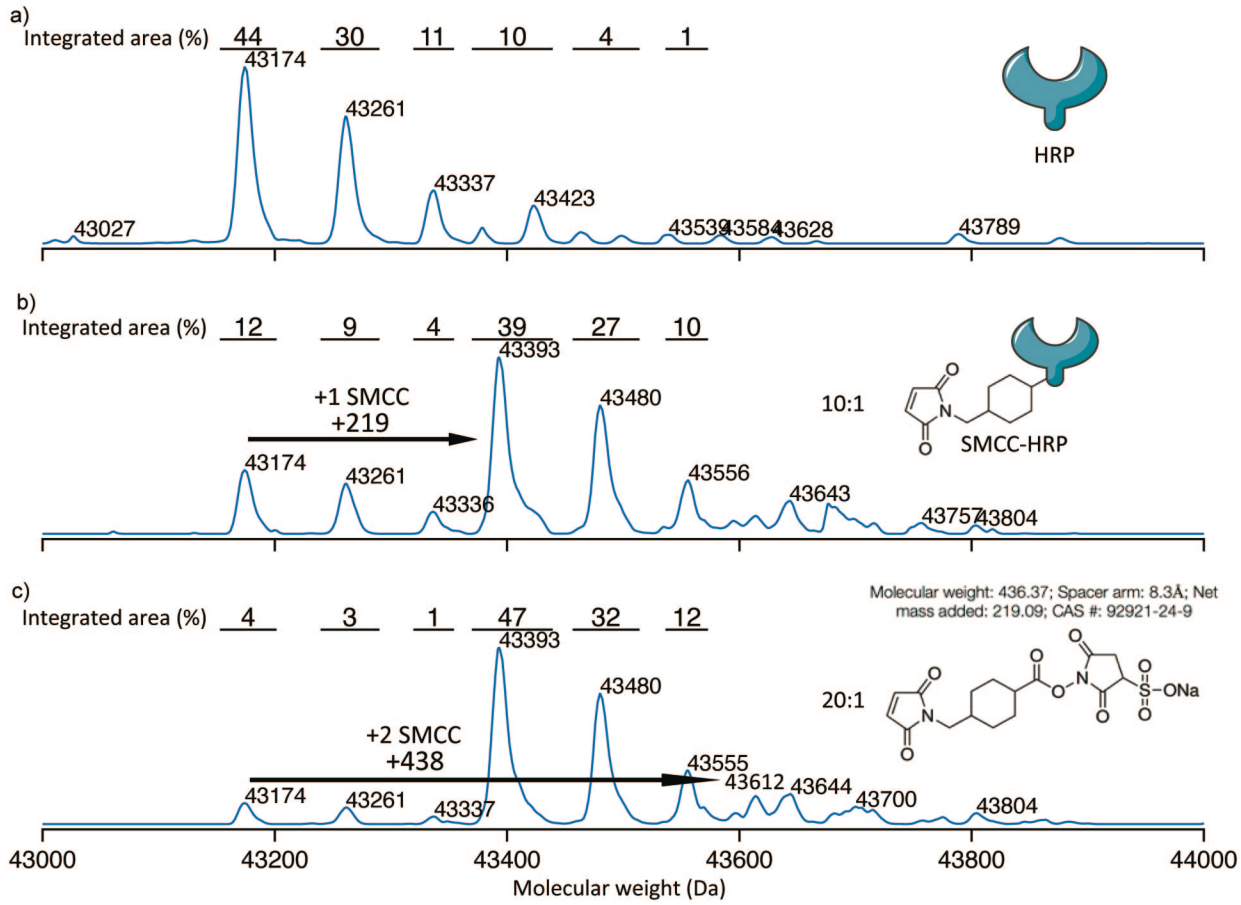

Figure 2.3. SMCC-HRP conjugation ratio optimization. Quantitative time-of-flight mass spectrometry (QTOF-MS) of HRP alone (a), SMCC-HRP reacted at a 10:1 ratio (b), and SMCC-HRP reacted at a 20:1 ratio (c) shows a ratio-dependent degree of maleimide functionalization. Though poly-dispersed, the primary mass of HRP alone by QTOF-MS reads as 43147 Da as seen in (a). According to the manufacturer, the mass added for one maleimide addition to HRP corresponds to about 219 Da, as seen by the appearance of the 44393 Da peak in (b). Similar additions of 219 Da to the other peaks present in (a) can be seen in (b) as well. Though (c) reveals 20:1 SMCC:HRP leads to a higher mono-functionalization than 10:1 as indicated by percent integrated area, it also exhibits higher dual-functionalization in the appearance of the 43612 Da peak. To minimize the potential of multiple maleimide additions reducing enzymatic activity, 10:1 SMCC:HRP was chosen for SWCNT conjugation.

To solubilize SH-SWCNTs for conjugation with HRP, we assessed 3 potential amphiphilic SWCNT dispersants: $(GT)_{15}$ ssDNA, the amphiphilic lipid C_{16}-PEG(2000)-Ceramide (Cer), and

the surfactant sodium cholate (SC). We induced noncovalent adsorption of each coating with SWCNTs through π-π aromatic stabilization and hydrophobic attraction, respectively. Each dispersant was added to SH-SWCNTs and subjected to probe-tip sonication on ice according to previously established protocols.[40,70] The resulting products ($(GT)_{15}$-SH-SWCNT, Cer-SH-SWCNT, and SC-SH-SWCNT) showed high yield (100-300 mg L^{-1}) and solubility in water after centrifugation to remove aggregates and excess dispersant (Figure 2.4a).

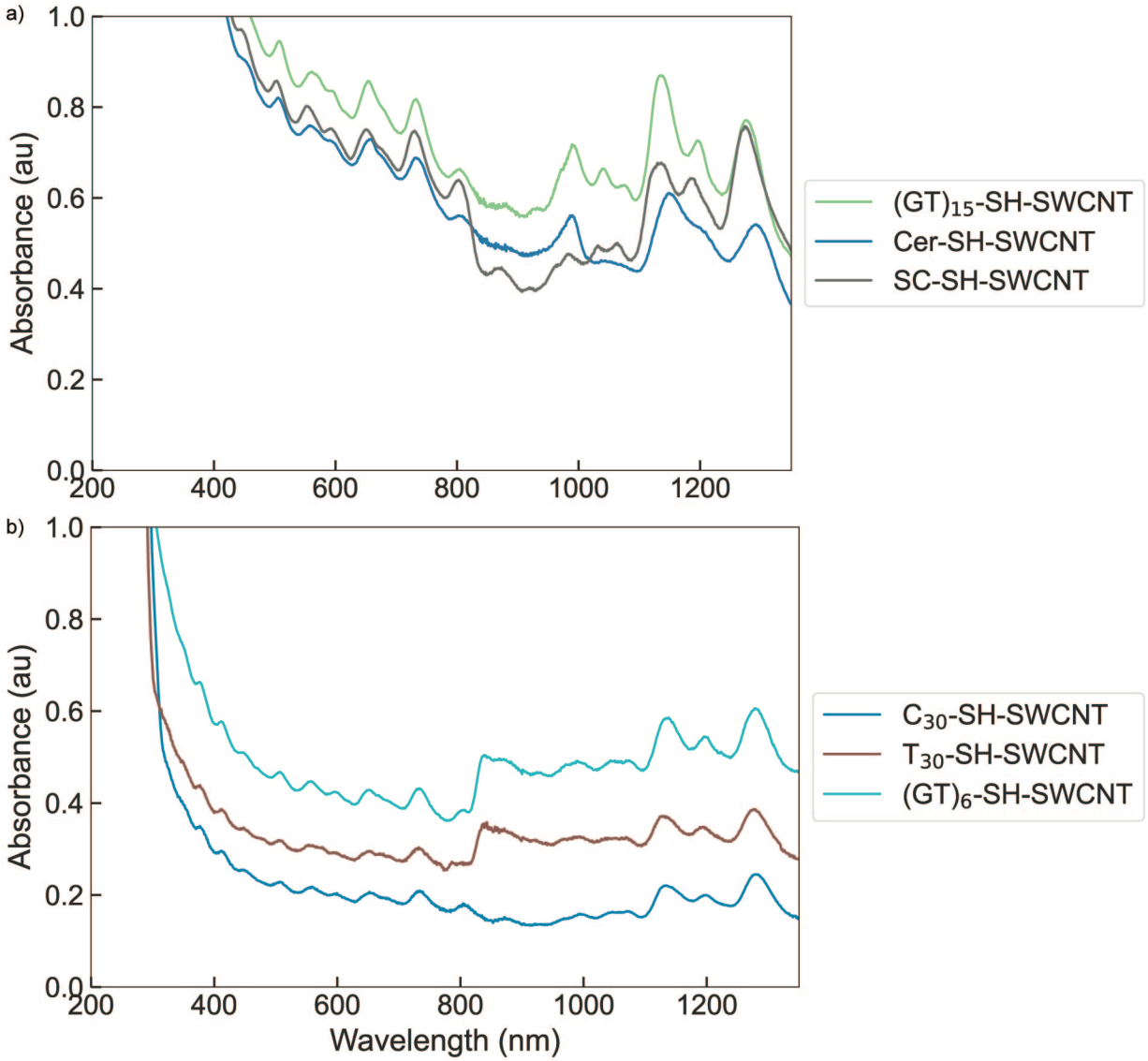

Figure 2.4. UV-Vis-IR absorbance spectra of SH-SWCNTs after probe tip sonication and centrifugation. After unsuspended SWCNT aggregates were removed by centrifugation, absorbance spectra were taken for each sample. All samples show expected SWCNT absorbance peaks in the nIR range (850 to 1350 nm), indicating probe tip sonication minimally interfered with the SWCNT sp^2 lattice. Each sample was diluted to normalize their absorbance to the linear range of Beer-Lambert's Law between 0 and 1 for accurate [SWCNT] calculation. (a) Cer-SH-SWCNTs were diluted 20X for absorbance measurements, while $(GT)_{15}$-SH-SWCNTs were diluted 10X and SC-SH-SWCNTs were diluted 2X. The corresponding absorbances at 632 nm

were used for Beer-Lambert's Law to measure [SWCNT] in each diluted sample of 18.77, 21.69, and 19.44 mg L^{-1}, respectively, and 375.42, 216.87, and 38.88 mg L^{-1} when multiplied by their dilution factors. (b) All samples were diluted 20X for absorbance measurements. The absorbances at 632 nm for C_{30}-SH-SWCNTs, T_{30}-SH-SWCNTs, and $(GT)_6$-SH-SWCNTs were used to measure [SWCNT] in each diluted sample of 5.18, 7.76, and 11.09 mg L^{-1}, respectively, and 103.54, 155.26, and 221.87 mg L^{-1} when multiplied by their dilution factors.

The solubilized SWCNT products were subsequently assessed for the degree of nonspecific HRP adsorption to their surface with a corona exchange dynamics assay.[58] Briefly, this assay leverages the fluorescence quenching effect of fluorophores proximal to SWCNT to measure the degree of nonspecific protein adsorption to SWCNT surfaces. Compared to fluorescein (FAM)-functionalized control proteins fibrinogen (FBG-FAM) and human serum albumin (HSA-FAM), HRP-FAM showed lower FAM fluorescence quenching when incubated with SWCNTs, indicated by a higher endpoint fluorescence fold change value (Figure 2.5). Since the degree of FAM quenching is proportional to the amount of nonspecific protein adsorption to the SWCNT surface, our results suggest that HRP shows minimal nonspecific adsorption to all three dispersed SWCNTs. This result highlights the utility of HRP as a model protein as its low level of adsorption helps ensure subsequent SWCNT sensor responses can be attributed to covalently attached HRP only, rather than a mixed population of covalently-attached and nonspecifically-adsorbed HRP.

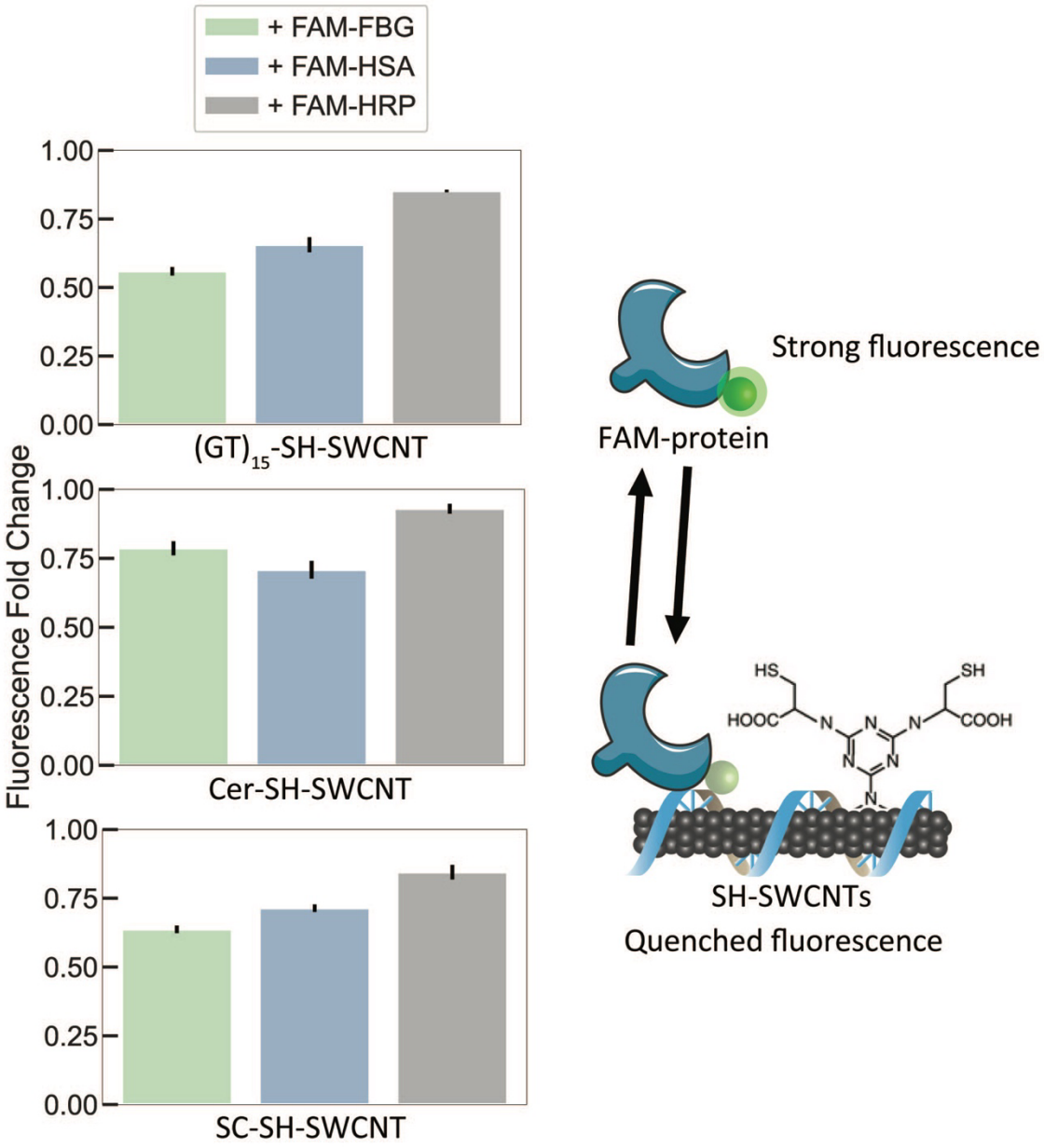

Figure 2.5. Corona exchange dynamics characterization of HRP with dispersed SH-SWCNTs. Corona exchange assay for HRP and control proteins shows minimal HRP adsorption to different dispersant-SH-SWCNT samples. Fold change was calculated as the endpoint FAM fluorescence value 60 min after SWCNT addition to FAM-proteins divided by the initial FAM fluorescence for each protein sample. Error bars represent the standard deviation of experimental replicates (n = 3).

Though all three dispersants were good candidates in minimizing nonspecific HRP adsorption, we proceeded with H_2O_2 nanosensor development with $(GT)_{15}$-SH-SWCNTs as they showed greater colloidal stability than SC-SH-SWCNTs through the rest of the sensor's synthesis (Figure 2.6a) and greater response to H_2O_2 than Cer-SH-SWCNTs (Figure 2.7a).

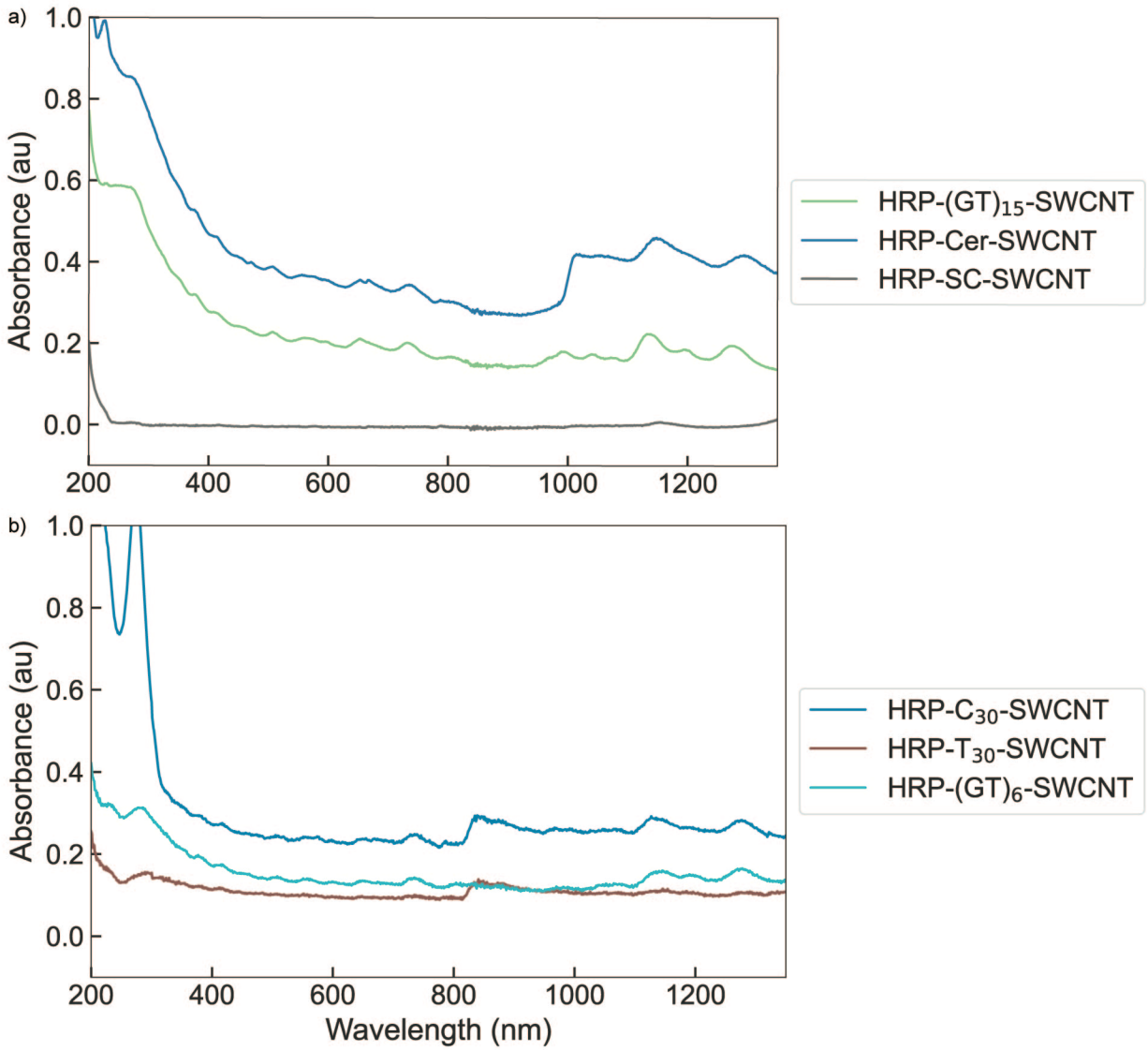

Figure 2.6. HRP-$(GT)_{15}$-SWCNT compared to other HRP-SWCNTs. (a) UV-Vis-IR absorbance spectra show loss of colloidal stability for HRP-SC-SWCNTs after purification as shown by the complete loss of characteristic SWCNT absorbance compared to $(GT)_{15}$- and Cer-coated HRP-SWCNTs. (b) UV-Vis-IR absorbance spectra for HRP-T_{30}-SWCNTs, HRP-C_{30}-SWCNTs and HRP-$(GT)_6$-SWCNTs.

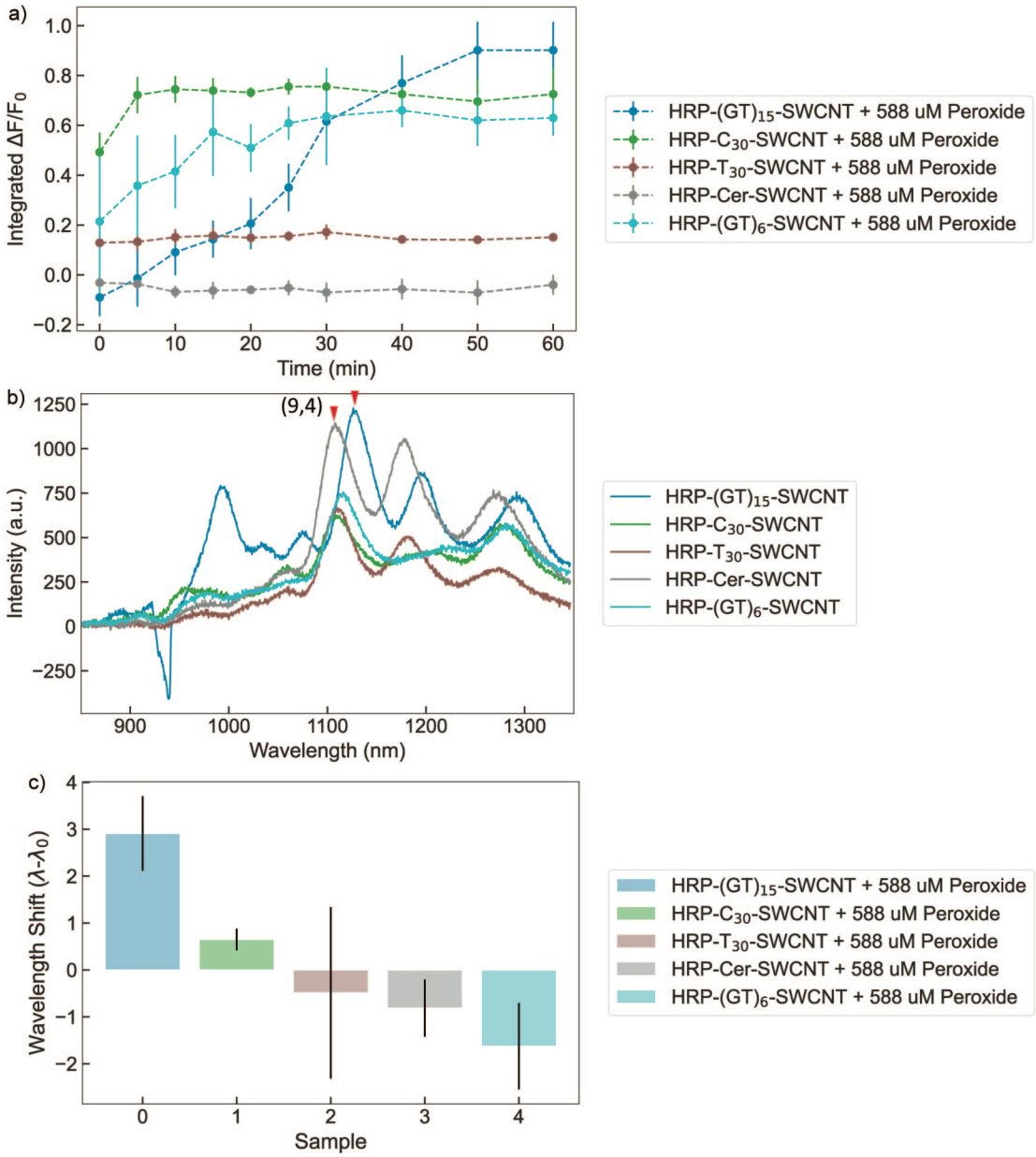

Figure 2.7. HRP-$(GT)_{15}$-SWCNT nanosensor fluorescence response to H_2O_2 compared to HRP-SWCNTs with other dispersants. (a) Comparing the integrated change in fluorescence for each sensor construct in response to the same amount of H_2O_2 shows a similar response profile between the HRP-$(GT)_{15}$-SWCNT nanosensor and HRP-C_{30}-SWCNT and HRP-$(GT)_6$-SWCNT. By contrast, HRP-Cer-SWCNT shows no turn-on response and HRP-T_{30}-SWCNT shows a small but immediate turn-on response. (b) The fluorescence baselines of all HRP-SWCNT constructs show strong quenching before H_2O_2 addition, enabling the large magnitude fluorescence turn-on response observed in (a). The wavelength range of the (9,4) SWCNT chirality is marked with red arrows for tracking solvatochromic shifts. (c) Endpoint (60 min post-H_2O_2 addition) wavelength shifts for the (9,4) chirality fluorescence peaks of the samples shown in (a) show no clear trend in relation to the observed turn-on response. Of the three constructs that exhibited a turn-on response, the HRP-$(GT)_{15}$-SWCNT nanosensor shows the largest red-shift in fluorescence while HRP-C_{30}-SWCNT shows no solvatochromic shift and HRP-$(GT)_6$-SWCNT

shows a slight blue-shift. Both HRP-Cer-SWCNT and HRP-T_{30}-SWCNT shows slight blue-shifts despite exhibiting no turn-on response to H_2O_2. Error bars represent the standard deviation between experimental replicates (n = 3).

After de-salting excess unreacted crosslinker from the SMCC-HRP reaction, we reacted SMCC-HRP with $(GT)_{15}$-SH-SWCNTs to covalently link HRP to SWCNTs. Following centrifugal membrane filtration to remove excess unreacted SMCC-HRP (Figure 2.8), we characterized the final nanosensor product (HRP-$(GT)_{15}$-SWCNT). The nanosensor showed maintained characteristic optical absorbance (Figure 2.2a) and fluorescence (Figure 2.2b) properties of SWCNT throughout the synthesis process. The different peaks in Figure 2.2b correspond to different chiralities of SWCNT, which emit fluorescence at different intensities in response to our excitation laser at 721 nm. This monochromatic laser predominantly excites the (10,2), (9,4), (8,6), (10,5), and (8,7) chiralities more efficiently than chiralities that resonate at lower excitation wavelengths, resulting in the largest emission peaks at wavelengths greater than 1100 nm. The relative intensities of these emission peaks were slightly altered following triazine functionalization for $(GT)_{15}$-SH-SWCNT compared to pristine $(GT)_{15}$-SWCNT, where the (9,4) and (8,6) chirality SWCNTs showed increased emission intensity at 1135 nm and 1195 nm, respectively, relative to the other chirality peaks at shorter wavelengths. This is expected from previous literature findings that the triazine functional group modifies the SWCNT chemical potential, increasing emission intensity for these chiralities at our excitation wavelength of 721 nm.[68] To account for these different chirality effects, we opted to analyze the nanosensor response by measuring the area under the fluorescence emission curve by integrating from 850 to 1350 nm rather than measuring the intensity at any single chirality peak wavelength.

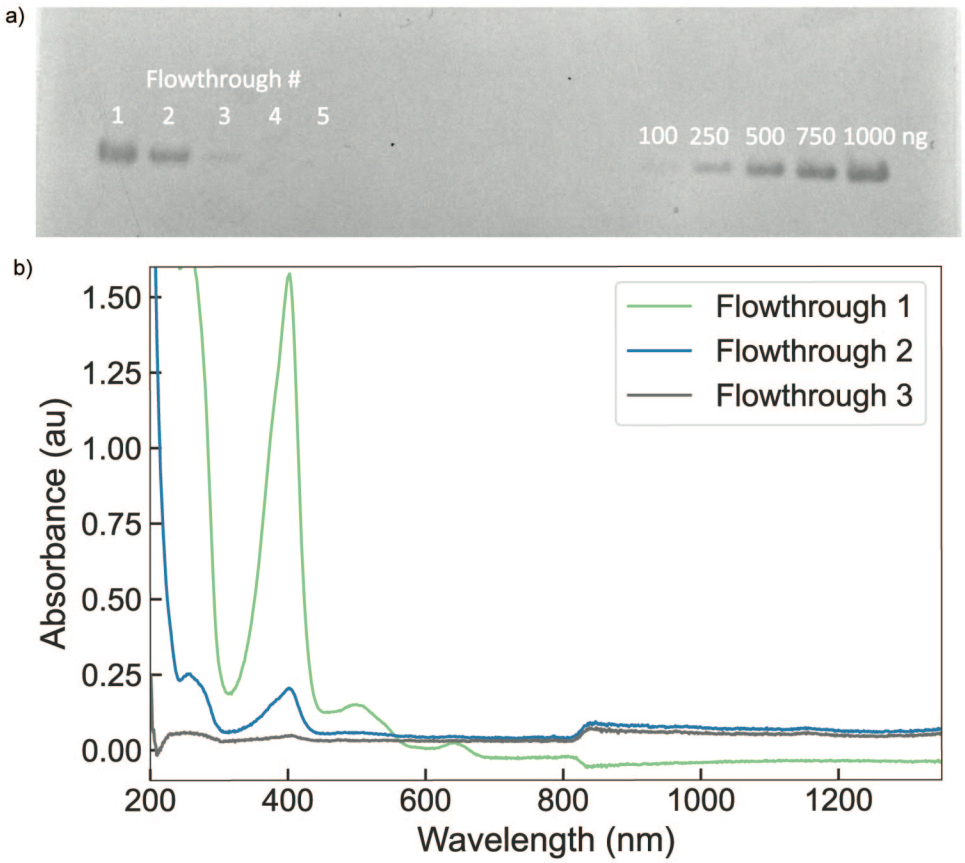

Figure 2.8. Purification of SWCNT from unconjugated SMCC-HRP. (a) SDS-polyacrylamide gel electrophoresis (SDS-PAGE) gel of spin-filter flowthrough shows full protein removal after three washes. Control additions of 100-1000 ng HRP to gel show barely detectable protein at 100 ng, thus 3 spin-filtration steps are sufficient to remove protein from nanosensor. (b) UV-Vis-IR absorbance spectroscopy of the spin-filter flowthroughs confirm minimal free protein remains in the sample. The absorbance peak of HRP at 400 nm gradually decreases to 0 in successive filter flowthroughs, echoing the findings from PAGE analysis.

We found that attaching HRP to SWCNTs yielded a decrease in fluorescence intensity proportional to the concentration of HRP in the conjugation reaction, with minimal shifts in the SWCNT fluorescence peak wavelengths for HRP-$(GT)_{15}$-SWCNT relative to the base $(GT)_{15}$-SH-SWCNT material (Figure 2.9b). This uniform decrease in fluorescence intensity is a desired and common mechanism to generate turn-on fluorescent nanosensors.[75] Since the observed quenching is proportional to the amount of HRP available for conjugation, we hypothesize that HRP is affecting SWCNT fluorescence emission by proximity to the surface upon conjugation, leading to greater attenuated fluorescence intensity as more HRP is conjugated. If this attenuation was due to unintended quantum defects or other sp^2 lattice damage introduced by the synthesis process, the SWCNT fluorescence intensity would not be modulated in the presence of the HRP substrate H_2O_2 but instead remain attenuated. Subsequent experiments show that the resulting nanosensors can modulate in fluorescence and exhibit different fluorescence responses to the addition of H_2O_2, with the highest magnitude of fluorescence increase achieved with the nanosensor generated with 1 mg mL^{-1} HRP in the conjugation reaction (Figure 2.9a). Additionally, previous studies have shown that SWCNT fluorescence intensity decreases in the presence of H_2O_2 rather than increase,

providing further evidence that the catalysis of H_2O_2 by HRP facilitates the turn-on fluorescence response.[76]

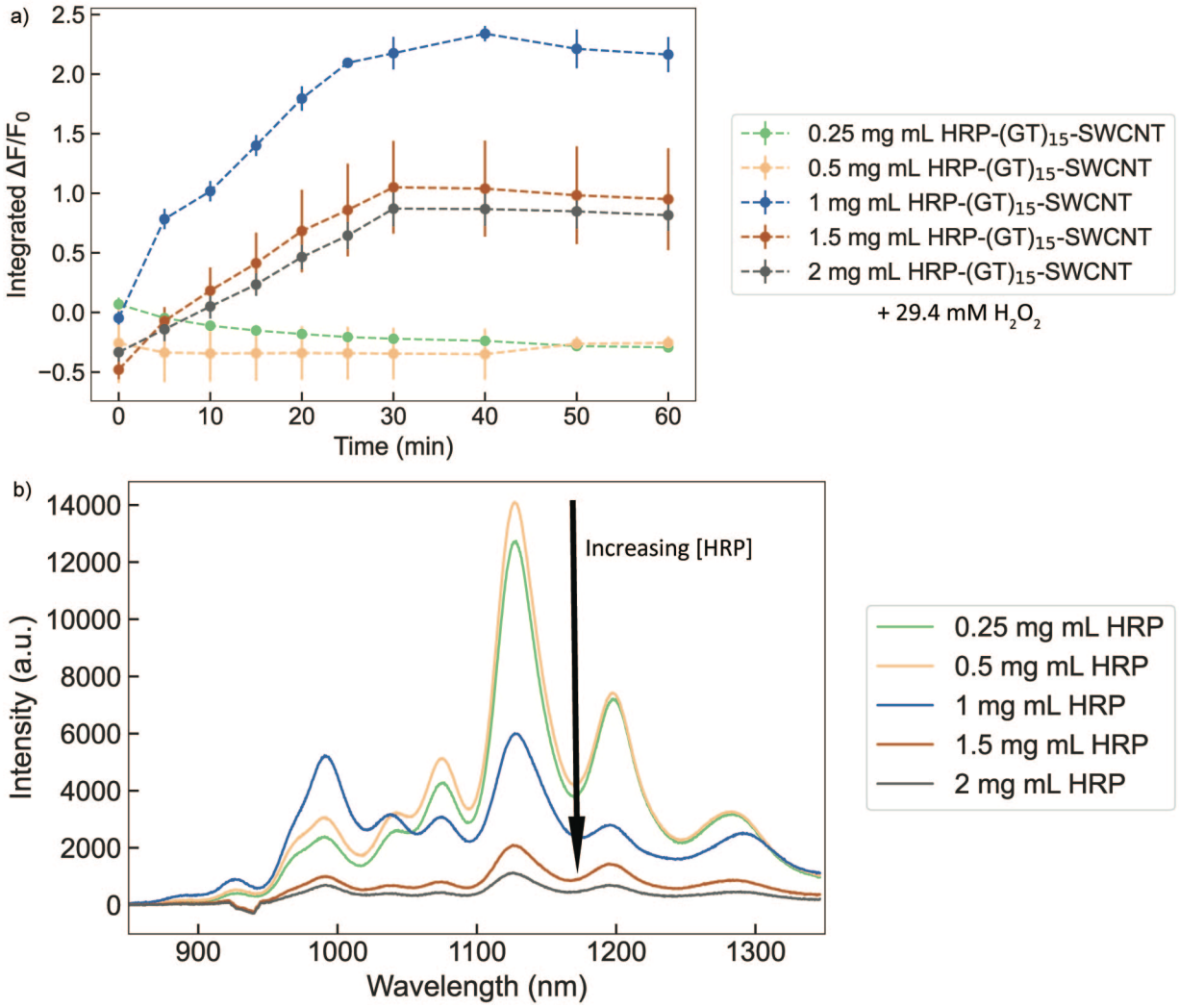

Figure 2.9. Optimizing [HRP] in conjugation reaction via nanosensor fluorescence turn-on response. (a) Varying the concentration of HRP in the covalent conjugation reaction to SWCNTs results in varied nanosensor fluorescence responses to the same concentration of H_2O_2. At 0.25 and 0.5 mg mL^{-1} HRP in the conjugation step, the product nanosensor shows a turn-off response to 29.4 mM H_2O_2. Increasing the HRP concentration to 1 mg mL^{-1} results in a product that exhibits a 200% increase in fluorescence intensity upon H_2O_2 addition. However, increasing the HRP concentration further to 1.5 and 2 mg mL^{-1} decreased the nanosensor's peak response to around 100%. Thus, an optimum functionalization density of HRP on SWCNT exists when the reaction conditions are 1 mg mL^{-1} HRP to 10 mg L^{-1} $(GT)_{15}$-SH-SWCNT. (b) The fluorescence baseline of the HRP-$(GT)_{15}$-SWCNT nanosensors is progressively quenched as HRP concentration is increased in the conjugation step. As HRP concentration is increased, it is probable that the number of HRP attached per SWCNT increases proportionally, leading to increased fluorescence quenching as seen by progressive decrease in the intensity peak around 1134 nm corresponding to the (9,4) chirality SWCNT.

Mechanistically, we hypothesize that the SWCNT quenching behavior upon HRP conjugation could be attributed to a proximity effect of the charged heme center of HRP or HRP itself on SWCNT fluorescence emission. SWCNT fluorescence occurs by exciton recombination, where an electron in the valence band of SWCNT is photo-excited by visible light, creating an excited electron-hole pair (exciton), and subsequently decays back to its ground state, recombining with the empty hole in the SWCNT valence band and emitting fluorescence.[43,44] As such, positively charged groups near the SWCNT surface could effectively serve as a charge trap, locally stabilizing excitons and lowering the exciton energy below the needed threshold for radiative recombination and fluorescence emission.[77] At its native state, the heme iron of HRP exists as Fe^{3+} and the proximity of this positively charged metal ion to the SWCNT surface could lower exciton recombination energy, resulting in nonradiative electron decay and fluorescence quenching. Previous literature supports this possibility, demonstrating that free metal ions,[78] ferricyanide,[54] and free heme[79] added to SWCNTs strongly quench their fluorescence by this nonradiative mechanism. Similarly, HRP exhibits an isoelectric point (pI) between pH 8.7 and 9,[80] resulting in a net positive (+2) charge at neutral pH.[81] Thus, HRP itself could also serve as a charge trap and quench SWCNT fluorescence by the same nonradiative decay mechanism.

2.4 Conclusions

Overall, these results confirm HRP as a good model protein for optimization of this platform because HRP is amenable to singular SMCC functionalization, easily purified from SWCNTs via spin-filtration, and shows minimal nonspecific adsorption to SWCNTs via the corona exchange dynamics assay. Characterization techniques such as UV-Vis-IR absorbance and nIR fluorescence to ensure SWCNT integrity, QTOF-MS to confirm crosslinker functionalization, corona exchange dynamics to validate minimal nonspecific protein adsorption, and SDS-PAGE to affirm separation of free protein from the final nanosensor product can help identify any given protein's candidacy for SWCNT conjugation with this platform.

The platform and conditions presented in this chapter can serve as a starting point for conjugating any protein of interest to SWCNTs so long as they achieve the figures of merit listed above. Should this not be the case for a protein of interest, many modifications to the platform are possible with the flexibility this platform provides. Suggested modifications include varying SMCC:Protein ratios to optimize singular functionalization, choosing different SWCNT dispersant molecules to mitigate nonspecific protein adsorption, or even functionalizing SWCNT with different moieties for alternative conjugation chemistries, such as EDC/NHS conjugation or "click" chemistry, depending on a given protein's properties that make it more amenable to a different chemical strategy. Altogether, this platform offers a modular, flexible, and robust strategy to covalently conjugate proteins to SWCNT.

2.5 Materials and Methods

Materials: All chemicals unless otherwise stated were purchased from Sigma-Aldrich. Raw high pressure carbon monoxide (HiPco) synthesized SWCNTs were purchased from NanoIntegris (SKU# 1601). C_{16}-PEG(2000)-Ceramide (N-palmitoyl-sphingosine-1-{succinyl[methoxy(polyethyleneglycol)2000]}) was purchased from Avanti Polar Lipids (SKU# 880180P). $(GT)_{15}$ ssDNA was purchased from Integrated DNA Technologies. Sulfo-SMCC

(sulfosuccinimidyl 4-(N-maleimidomethyl)cyclohexane-1-carboxylate) was purchased from ThermoFisher Scientific (Catalog# A39268). Hydrogen Peroxide (3% w/w) was purchased from Labchem (Catalog# LC154501).

Synthesis of SH-Functionalized SWCNTs: Synthesis of SH-functionalized SWCNTs was adapted from previous literature.[68,70] Briefly, pristine HiPco SWCNTs (1 g) were dispersed in *N*-methyl-2-pyrrolidone (NMP) (150 mL) in a round bottom flask with a stir bar. The mixture was bath sonicated (Branson Ultrasonic 1800) for 1 h at 25 °C followed by gentle stirring for 1 h at 25 °C. The mixture was then cooled to 0 °C on ice. 2,4,6-1,3,5-trichloro-triazine (10 g, 54 mmol) was dissolved in NMP (50 mL) and slowly added to the SWCNT dispersion. The resulting mixture was stirred for 20 min at 0 °C. Sodium azide (1.76 g, 27 mmol) was gradually added to the mixture and stirred for 2 h at 0 °C. The mixture was then stirred at 25 °C for 1 h followed by stirring at 70 °C for 12 h to yield Trz-H-SWCNTs. This product was purified by repeated centrifugation and washing steps with 10 mL each of acetone, water, toluene, then chloroform. The purified product was then lyophilized for storage and characterization.

Trz-H-SWCNTs (10 mg) were dispersed in dimethylformamide (DMF) (5 mL) and bath sonicated for 15 min at 25 °C. Cysteine (1 mg) and a 1.5 M excess of triethylamine were added to the mixture and stirred for 48 h at 65 °C. The product (SH-SWCNTs) was purified by centrifugation, supernatant removal, and re-dispersion in washes of DMF (4 mL, 2X) then water (4 mL, 2X). The product was then dialyzed against water using a Slide-A-Lyzer G2 10 kDa MWCO dialysis cassette (Thermo Scientific) for 1 week with daily water changes (2 L). The purified product was pelleted by centrifugation and lyophilized for storage, characterization, and covalent HRP functionalization.

Noncovalent Adsorption of ssDNA to SH-SWCNTs by Probe-Tip Sonication: SH-SWCNTs (1 mg) and $(GT)_{15}$ single-stranded DNA (1 mg) were dispersed in 1X phosphate buffered saline (PBS) (500 µL, pH 7.4) and bath sonicated for 10 min at 25 °C. The solution was then probe-tip sonicated with an ultrasonic processor (Cole Parmer) and a 3 mm stepped microtip probe with pulses of 3-7 W for 1 s followed by 2 s of rest for a total sonication time of 15 min. The solution was equilibrated for 1 h at 25 °C then subsequently centrifuged at 16100 relative centrifugal force (RCF) for 30 min to remove unsuspended SWCNT aggregates. Suspended SWCNTs formed a homogeneous dark gray solution and were measured for concentration by UV-Vis-IR absorbance (Shimadzu UV-3600 Plus) with samples in a 100 µL volume, black-sided quartz cuvette (Thorlabs, Inc.). SWCNT concentration was calculated from absorbance at 632 nm using the Beer-Lambert law with extinction coefficient $\varepsilon_{632} = 0.036$ L mg^{-1} cm^{-1}.[38]

Corona Exchange Dynamics Assay for HRP-SWCNT Adsorption: Corona exchange dynamics studies were conducted as described previously.[58] Briefly, HRP, fibrinogen, and human serum albumin were labeled with a fluorophore (FAM) via N-hydroxysuccinimide ester conjugation (Lumiprobe). Protein (10 mg) in 1X PBS (900 µL) and an 8-fold molar excess of FAM-NHS in dimethyl sulfoxide (DMSO) (100 µL) were gently mixed via end-over-end rotation in a foil-covered tube for 4 h. FAM-protein conjugates were then purified with Zeba 2 mL spin desalting columns with 40 kDa MWCO (Thermo Scientific) to remove excess unreacted FAM-NHS according to manufacturer's instructions. The purified FAM-proteins were measured for concentration and degree of labeling via UV-Vis-IR absorbance at 280 nm for protein and 495 nm

for FAM. The degree of labeling was calculated as the molar ratio of FAM to protein in the samples. 200 mg L^{-1} FAM fluorophore-labeled protein (25 μL) was added to 10 mg L^{-1} SH-SWCNTs dispersed with $(GT)_{15}$ ssDNA, C_{16}-PEG2k-Ceramide, and SC (25 μL) in triplicate. The solutions were combined via microchannel pipette in a 96-well PCR plate (Bio-Rad) and mixed by pipetting. The plate was sealed with an optically transparent adhesive seal and gently spun down in a benchtop centrifuge. Fluorescence time series measurements were obtained with a Bio-Rad CFX96 Real Time qPCR System by scanning the FAM channel every 30 s at 25 ºC.

Covalent Conjugation of HRP to SH-SWCNT via Sulfo-SMCC Crosslinker: $(GT)_{15}$-SH-SWCNTs were diluted to 20 mg L^{-1} in PBS and 5% v/v TCEP to reduce disulfide bonds between SWCNTs. HRP was similarly diluted to 2 mg mL^{-1} in PBS and Sulfo-SMCC dissolved in Milli-Q H_2O was added at 10:1 molar ratio Sulfo-SMCC:HRP. Both mixtures were incubated separately for 1 h at 25 ºC. Each solution was then de-salted to remove excess TCEP and Sulfo-SMCC, respectively, with 7K MWCO Zeba Spin Desalting Columns (2 mL) according to manufacturer's instructions. Purified $(GT)_{15}$-SH-SWCNTs and maleimide-functionalized HRP were then mixed at a final concentration of 10 and 1 mg mL^{-1}, respectively, and incubated 1 h at 25 ºC. The finished reaction mixture was purified to remove unconjugated maleimide-HRP with 100K MWCO Amicon Ultra Centrifugal Filters (0.5 mL). The membrane was rinsed with PBS and centrifuged at 5000 rcf for 5 min. The raw reaction mixture was then added and spun at the same conditions. PBS (450 μL) was added to the membrane to wash away excess protein and spun at the same conditions and repeated once. Finally, the membrane was cleaned with PBS (200 μL) to remove adsorbed SWCNTs and the membrane was inverted and spun at 1000 rcf for 2 min to collect the purified sample. The recovered HRP-$(GT)_{15}$-SWCNTs were then diluted to their original reaction volume and characterized by UV-Vis-IR absorbance and nIR fluorescence measurements.

SDS-PAGE of Nanosensors and Filtration Flowthroughs: SDS-PAGE was performed according to previously established protocols. Briefly, sample buffer was prepared by combining glycerol (2.5 mL), water (3.75 mL), 0.5 M Tris-HCl buffer pH 6.8 (1.25 mL), and 10% w/v SDS (2 mL). Gel running buffer was prepared with 10X Tris/Glycine/SDS Buffer (50 mL, Bio-Rad) and deionized water (450 mL). Sample (5 μL) was added to sample buffer (7.5 μL) and 6X loading dye (2.5 μL, New England Biosciences) and boiled at 95 ºC for 5 min. Samples were then loaded onto a 4-20% Mini-PROTEAN® TGX™ Precast Protein Gel (Bio-Rad) in a Mini-PROTEAN® Tetra Vertical Electrophoresis Cell (Bio-Rad) with running buffer according to manufacturer's instructions. Gel electrophoresis was run with a Mini-PROTEAN® PowerPac Basic Power Supply (Bio-Rad) at 200 V for 30 min. The finished gel was then stained with Coomassie Brilliant Blue (Thermo Scientific) for 1 hour, shaking gently. The gel was then de-stained overnight with 50% water, 40% methanol, 10% acetic acid (v/v/v) solution. The final gel was rehydrated in water and imaged according to manufacturer's instructions on a Typhoon FLA 9500 laser scanner (Cytiva) in digitization mode with a 532 nm excitation laser and a long-pass green filter. Gel images were processed with imageJ to adjust color contrast and image field of view.

Chapter 3: Characterization of Protein-SWCNT Conjugates[‡]

3.1 Chapter Abstract

Covalent HRP-SWCNT conjugates generated with the platform detailed in Chapter 2 require characterization to confirm successful HRP attachment while maintaining enzymatic activity. Herein, we demonstrate several characterization techniques to confirm successful HRP attachment including visualization with atomic force microscopy, preserved HRP enzymatic activity via previously established luminol activity assays, stable HRP activity over time, and quantification of HRP per SWCNT by a luminescence calibration curve. This workflow of techniques can be applied to any protein-SWCNT conjugates generated with this platform if an enzymatic or binding activity assay is available and compatible with SWCNTs. When combined with the workflow in Chapter 2, these techniques successfully confirm covalent protein conjugation to SWCNT to generate a nanosensor with maintained SWCNT and enzymatic properties.

3.2 Visualizing HRP-SWCNT Conjugates via AFM

After developing and optimizing the reaction conditions for this nanosensor in Chapter 2, we characterized its physical and chemical properties to confirm the successful covalent attachment of HRP to SWCNTs while maintaining enzymatic activity. To visualize HRP on the surface of SWCNTs, we captured atomic force microscopy (AFM) images of HRP (Figure 3.1a) and HRP-$(GT)_{15}$-SWCNT (Figure 3.1b).

[‡] Portions of this chapter are adapted from Ledesma, F. *et al.* Covalent Attachment of Horseradish Peroxidase to Single-Walled Carbon Nanotubes for Hydrogen Peroxide Detection. Preprint at https://doi.org/10.1101/2023.12.14.571773 (2023).

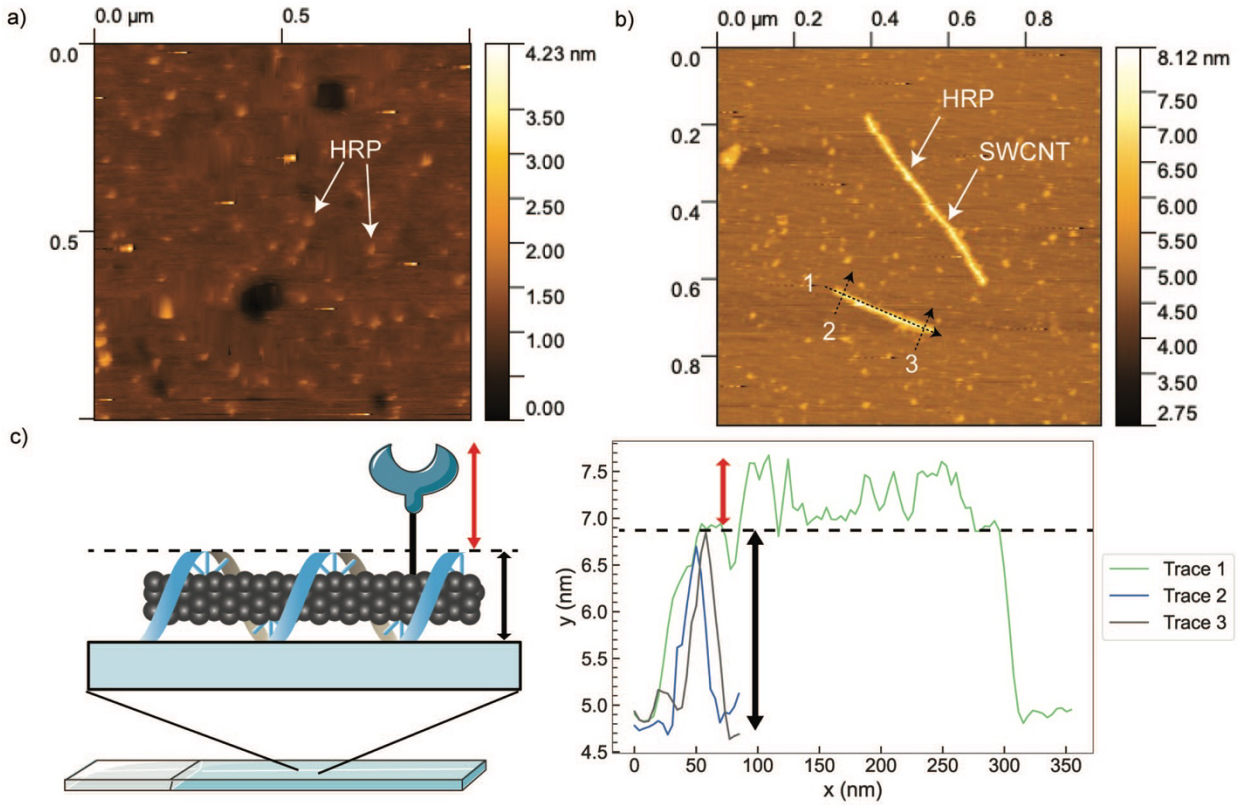

Figure 3.1. Validation of HRP presence for HRP-$(GT)_{15}$-SWCNT nanosensors. (a) AFM image of HRP. Height trace analysis shows a height increase of ~0.7 nm for this protein when accounting for the surface baseline (Figure 3.2). (b) AFM image of nanosensor shows individual SWCNTs with several height spikes along axis, visually confirming both successful $(GT)_{15}$ dispersion (minimal aggregates) and HRP conjugation. (c) Height trace analysis of the AFM image in (b) shows that the height spikes along the SWCNT axis (Trace 1) correspond to HRP height above SWCNT baseline (Trace 2,3).

Height trace analysis over 10 of the clearest proteins and subtracting the height of the bare surface yielded an average height of 0.66 nm for HRP under these conditions (Figure 3.2).

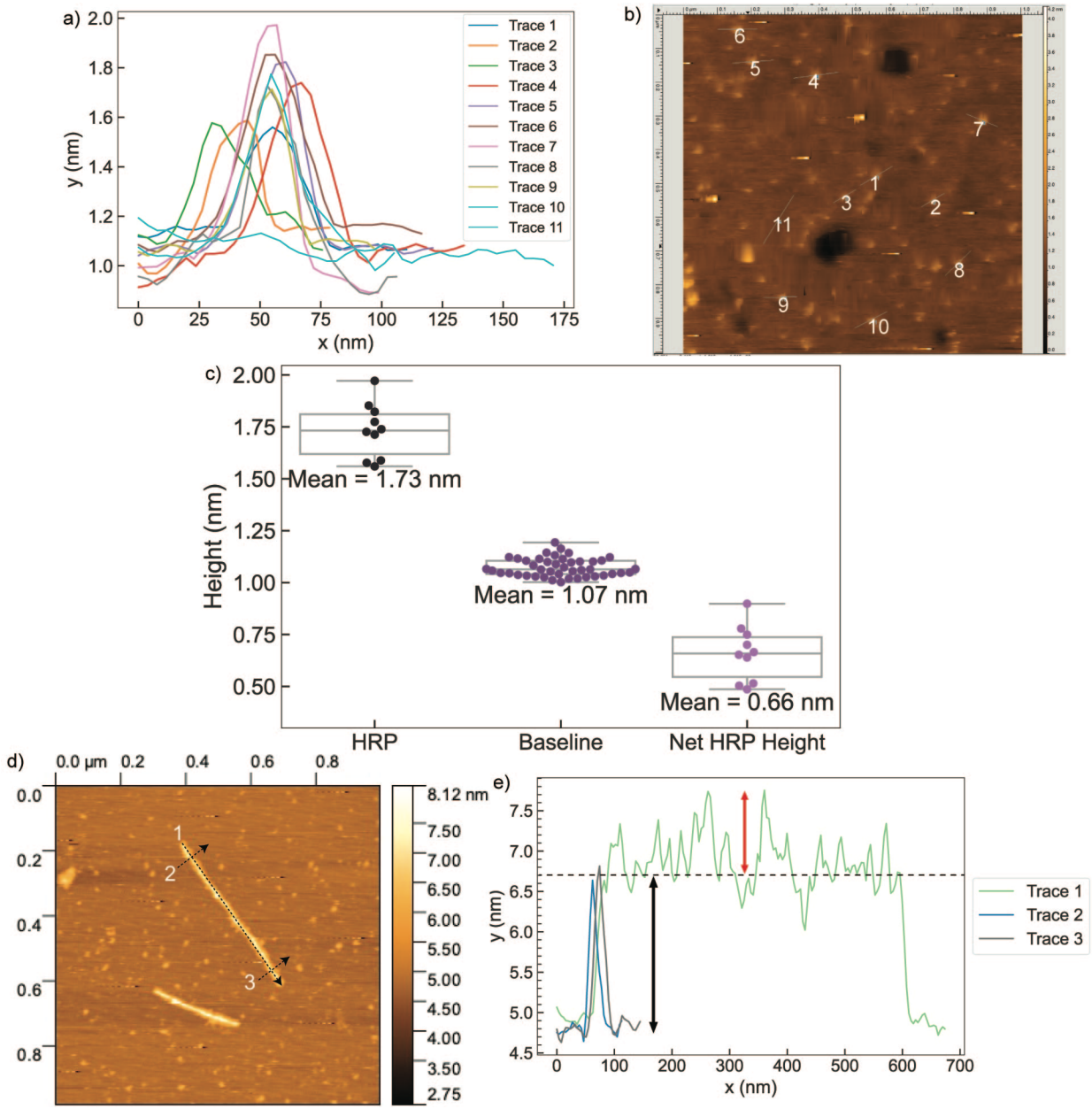

Figure 3.2. AFM trace analysis of free HRP and HRP-$(GT)_{15}$-SWCNT. (a) Trace analysis of 10 free HRP proteins in Figure 3.1a shows consistent peaks in height and width compared to a baseline trace (Trace 11). (b) Traces plotted in (a) shown on the image itself. (c) Boxplot of the results from (a) show the distribution and mean of heights found in the image, with the net HRP height being the average of the baseline values subtracted from the raw HRP values, yielding an average height increase above the baseline in the image of 0.66 ± 0.13 nm. Our AFM values for HRP are consistent with prior reports of AFM height tracing for HRP which report raw HRP heights of ~1.6 nm.[82,83] (d) Traces taken parallel and perpendicular to the axis of the other HRP-$(GT)_{15}$-SWCNT shown in Figure 3.1b. (e) Height trace analysis of (d) shows varied but significant height increases above SWCNT baseline between 0.5 and 1 nm in height, in the range of the average value of HRP alone shown in (c). The differences in peak heights could

correspond to varied levels of protein deformation during the imaging process as the AFM probe is known to cause.[82]

Performing the same analysis along the length of the nanotube showed several peaks of increased height ~0.7 nm greater than the height of the nanotube as determined by tracing perpendicular to the SWCNT length axis (Figure 3.1c). Combined with the corona exchange results confirming minimal nonspecific adsorption of HRP to SWCNTs, these peaks can thus be attributed to covalently attached HRP as shown schematically (Figure 3.1c).

3.3 Validating Maintained Enzymatic Activity Post-Conjugation

To confirm that covalently attached HRP maintained enzymatic activity while on the surface of SWCNTs, we used a luminol assay according to established protocols.[84] Briefly, the oxidation of luminol by the catalysis of H_2O_2 by HRP produces luminescence proportional to protein activity when normalized for protein concentration. We thus measured luminescence values for all HRP conditions along the nanosensor synthesis route incubated with luminol and H_2O_2 (Figure 3.3).

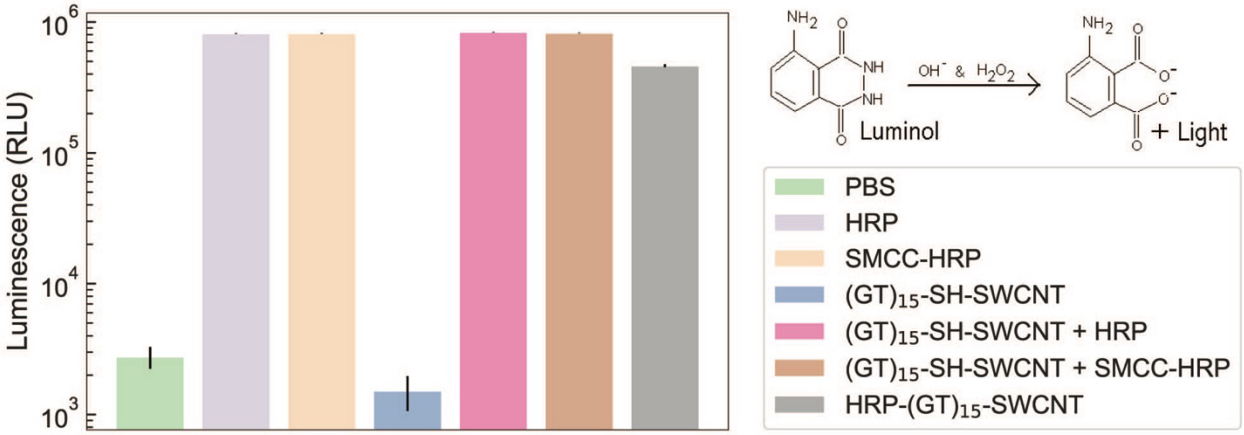

Figure 3.3. Validation of HRP activity for HRP-$(GT)_{15}$-SWCNT nanosensors. Luminol activity assay shows nanosensor has comparable HRP activity to control and that neither SMCC functionalization nor SWCNT presence interferes with HRP activity. Error bars represent the standard deviation between experimental replicates (n = 3).

Compared to the low luminescence magnitude shown by the controls of empty wells (Figure 3.4), PBS, and $(GT)_{15}$-SH-SWCNT alone, the nanosensor showed similar catalytic activity to the other HRP-containing samples at the same protein concentration. This data also suggests that SMCC functionalization does not negatively affect HRP activity under these conditions. Similarly, the presence of SWCNT showed little negative impact on the activity of both native and SMCC-HRP when mixed. Furthermore, we measured the enzymatic activity of our nanosensor over the course of 20 days, observing no noticeable decrease in luminescence (Figure 3.4).

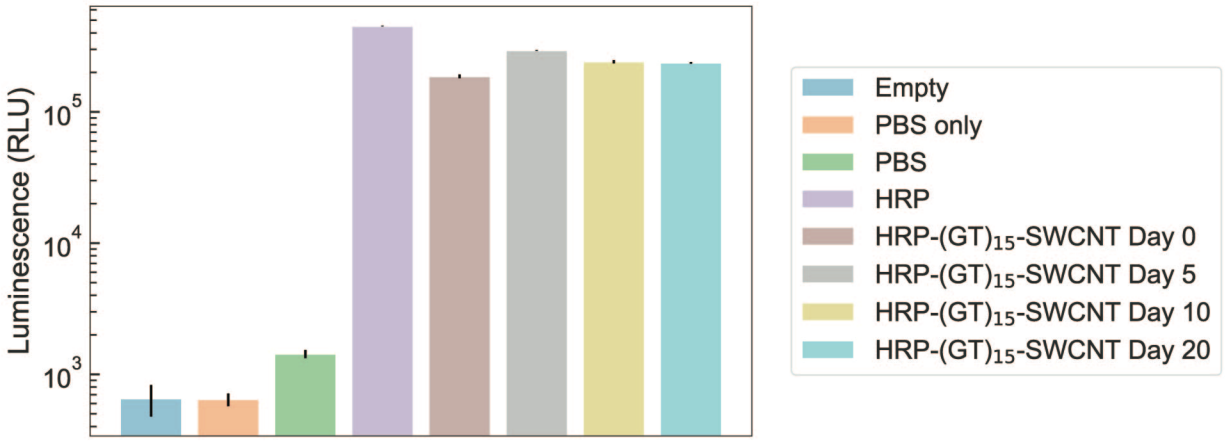

Figure 3.4. Luminol activity assay of nanosensor activity over time. The luminescence of empty wells and PBS only with no luminol are of similar magnitude to the addition of PBS to luminol, serving as a baseline of no HRP activity. In comparison, the enzymatic activity of the nanosensor over the course of 20 days remains high and stable. Error bars represent the standard deviation between experimental replicates (n = 3).

We also leveraged the luminol assay to calculate the concentration of HRP in each sample by using the luminescence values of a calibration curve of known HRP concentrations to extract a linear regression model (Figure 3.5b). Using the luminescence of the nanosensor with this model calculated an approximate HRP concentration of 0.415 μg mL^{-1} in the sample (Figure 3.5c). Since the concentration of SWCNT in the nanosensor sample can be determined by the absorbance at 632 nm (Figure 3.5d), we converted both values to moles by the known molecular weights of HRP (44 kDa) and SWCNT (2700 kDa) and divided the two to roughly approximate the number of HRP per SWCNT in the nanosensor at 80.5 ± 8.4 (Figure 3.5e). Taken together, these results suggest that we have synthesized a stable covalent HRP-SWCNT sensor with preserved SWCNT and enzymatic properties that can be assessed for its ability to sense hydrogen peroxide.

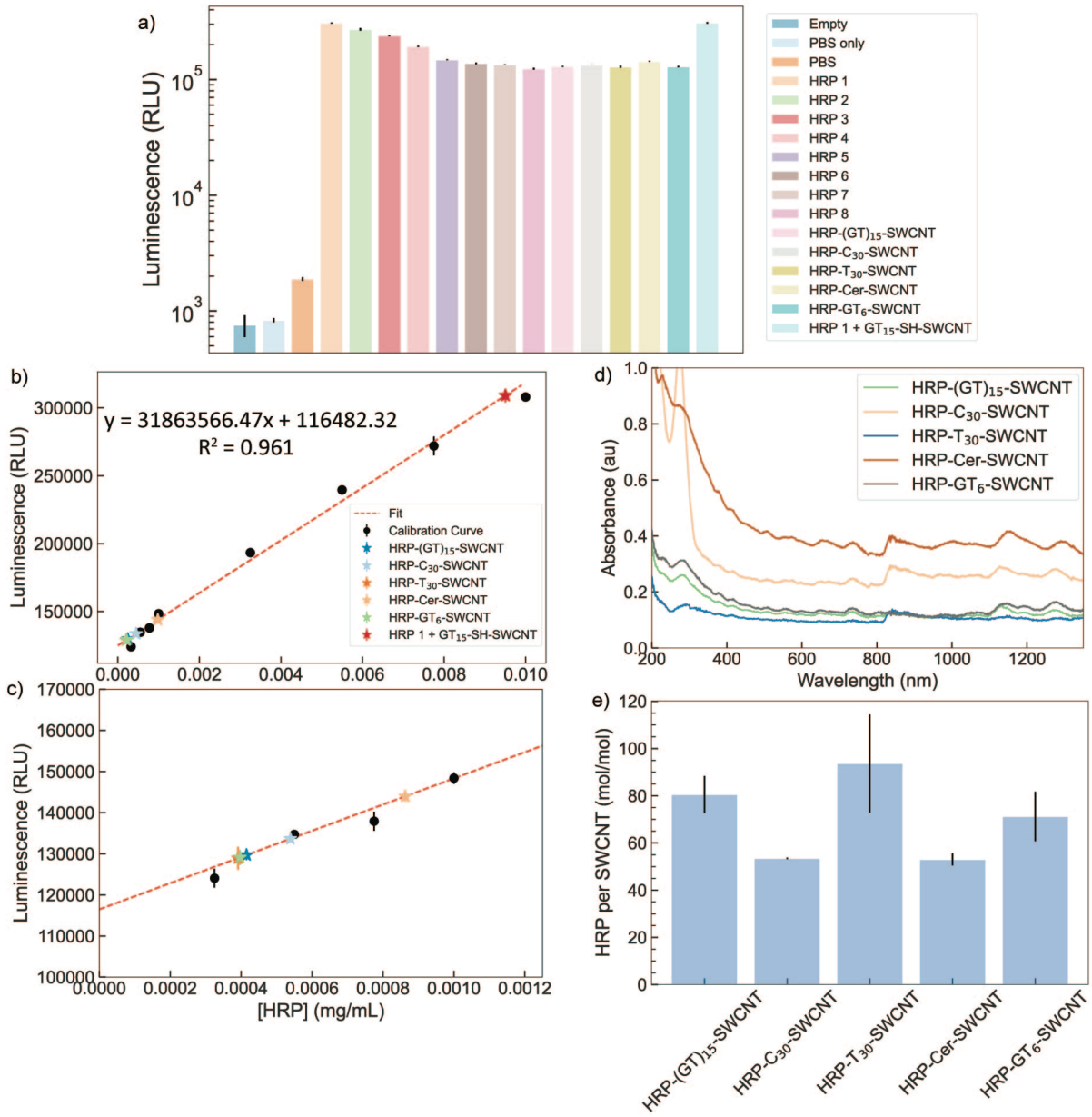

Figure 3.5. HRP-SWCNT luminol activity assay for [HRP] quantification. (a) A calibration curve from 0.325 μg mL^{-1} to 0.01 mg mL^{-1} (HRP 1-9) was created to calculate [HRP] from HRP-SWCNT sample luminescence values. (b) Plotting the calibration curve from (a) in black allows for fitting by linear regression in red. Using the resulting fitting parameters to calculate the [HRP] in each sample, the values are plotted as stars. (c) Zoomed in graph from (b) to highlight the region where each HRP-SWCNT sample is calculated. The concentration of HRP in the HRP-$(GT)_{15}$-SWCNT nanosensor sample is calculated to be 0.415 μg mL^{-1}. (d) UV-Vis-IR absorbance spectroscopy of each HRP-SWCNT sample in (c) is used to calculate [SWCNT] in each sample by taking the absorbance value at 632 nm and using Beer-Lambert's Law. (e) Using the known molecular weight of HRP at 44,000 g mol^{-1} and an average of the manufacturer's stated molecular weight range for SWCNTs (340,000 g mol^{-1} to 5,200,000 g mol^{-1} for SWCNTs 100-1000 nm long, respectively) at 2,770,000 g mol^{-1}, the mols of HRP and SWCNT in each

sample are calculated and divided to plot the ratio of HRP per SWCNT in each sample. The HRP per SWCNT ratio for the HRP-$(GT)_{15}$-SWCNT nanosensor is calculated at 80.5 ± 8.4. However, it is not expected that there are 80 HRP proteins attached to each individual SWCNT, since there is a distribution of SWCNT lengths in the sample from 100-1000 nm, but rather an average of 80 HRP proteins attached to SWCNTs for every individual SWCNT in the sample. Error bars represent the standard deviation between experimental replicates (n = 3).

3.4 Conclusions

Overall, these results confirm successful HRP conjugation to SWCNTs while maintaining HRP enzymatic activity. Height trace analysis of free HRP and nanosensor AFM images confirm HRP presence on the SWCNT surface. Given the previous validations in Chapter 2, these proteins must be covalently attached rather than noncovalently adsorbed, confirming successful conjugation via Sulfo-SMCC crosslinking. The luminol activity assay for HRP enzymatic activity confirms maintained HRP activity when functionalized with SMCC, in the presence of SWCNT, and covalently attached to SWCNT. This activity is also maintained over the course of 20 days, suggesting that attachment to SWCNT imparts greater stability and thus preserved activity compared to free protein alone. Finally, we leveraged the concentration-dependent nature of the luminescence emitted via the luminol activity assay to calculate the HRP concentration in the nanosensor sample from a concentration curve to be around 0.415 μg mL^{-1}. Combined with the SWCNT concentration in the sample as determined by UV-Vis-IR absorbance at 632 nm, we calculated an HRP/SWCNT (mol/mol) ratio of around 80 for the nanosensor. For generating other nanosensors with this platform, AFM should be performed to help visualize other proteins conjugated to SWCNT and corresponding activity assays should be conducted to confirm the synthesis process minimally damaged the protein.

3.5 Materials and Methods

Materials: All chemicals unless otherwise stated were purchased from Sigma-Aldrich. Raw high pressure carbon monoxide (HiPco) synthesized SWCNTs were purchased from NanoIntegris (SKU# 1601). C_{16}-PEG2k-Ceramide (N-palmitoyl-sphingosine-1-{succinyl[methoxy(polyethyleneglycol)2000]}) phospholipid was purchased from Avanti Polar Lipids (SKU# 880180P). $(GT)_{15}$ ssDNA was purchased from Integrated DNA Technologies. Sulfo-SMCC (sulfosuccinimidyl 4-(N-maleimidomethyl)cyclohexane-1-carboxylate) was purchased from ThermoFisher Scientific (Catalog# A39268). Luminol (Pierce ECL Western Blotting Substrate) was purchased from ThermoFisher Scientific (Catalog# 32209).

Atomic Force Microscopy of SWCNT Nanosensors: SWCNT nanosensors were analyzed for the presence of HRP with atomic force microscopy (AFM). A small square (1 cm x 1 cm) of mica substrate was adhered to a glass slide and the top surface was freshly cleaved with tape immediately prior to sample preparation. HRP-$(GT)_{15}$-SWCNT (100 μL) at 5 mg L^{-1} in 1X PBS was statically dispensed onto the mica surface and spin-coated at 2000 rpm for 1 min. Static dispense and spin coating was then repeated with an additional 100 μL of 5 mg L^{-1} HRP-$(GT)_{15}$-SWCNT to increase the coverage of functionalized SWCNT on the mica surface. Once doubly coated, deionized water (100 μL) was slowly dynamically dispensed onto the coated surface while spinning to rinse off excess salts. The sample was then stored at room temperature overnight and

imaged using a TAP150AL-G (Ted Pella) Aluminum Reflex coated tip coupled to an MFP-3D-BIO AFM (Asylum Research) in soft tapping mode.

Luminol Assay for HRP Activity: HRP activity was assessed using the Pierce™ ECL Western Blotting Substrate kit. Briefly, the samples were all diluted to the same HRP concentration as the lowest concentration to be measured for activity, typically the nanosensor. Each sample was confirmed to be at the correct [HRP] via Qubit assay according to manufacturer's instructions. The peroxide and luminol stocks from the kit were mixed at 1:1 by volume and added to each sample to dilute the [HRP] to the working concentration of 0.5 mg L^{-1} according to the manufacturer's instructions. Each sample (50 μL) was added to a 96-well plate in triplicate and the luminescence of each well was measured over 60 min on a luminescence plate reader (Tecan M1000).

Chapter 4: Nanosensor Fluorescence Response and Mechanism[§]

4.1 Chapter Abstract

Having validated the conjugation platform to covalently attach HRP to SWCNTs, we assess the nanosensor's fluorescence response to H_2O_2 and propose a mechanism of action for the nanosensor's observed performance. We demonstrate a concentration-dependent response to H_2O_2, confirm the nanosensor can image H_2O_2 in real-time using an immobilized imaging format, and assess the nanosensor's selectivity for H_2O_2 against a panel of biologically relevant analytes. We also assess the nanosensor's response to a variety of analytes such as inhibitors, various pH and ionic strength buffers, other enzymes, and surfactants to elucidate a mechanism that relies on the modulation of HRP redox state by H_2O_2 to modulate SWCNT fluorescence. Furthermore, we performed the synthesis process for the nanosensor while omitting the crosslinker Sulfo-SMCC to orthogonally confirm successful covalent HRP conjugation, observing low luminol activity and nIR fluorescence response compared to the nanosensor. Taken together, these results demonstrate successful generation of functional HRP-SWCNT nanosensors that show sensitive and selective fluorescence modulation in response to H_2O_2, are applicable in various form factors including immobilized on glass, and rely on HRP redox state for SWCNT fluorescence modulation.

4.2 Nanosensor Response to H_2O_2 in Solution-Phase Screens

We characterized our HRP-$(GT)_{15}$-SWCNT nanosensor's response to hydrogen peroxide by measuring the change in nIR SWCNT fluorescence over time in response to varied levels of H_2O_2 analyte, schematically represented in Figure 4.1a. The addition of 29.4 mM H_2O_2 elicited a strong and stable turn-on fluorescence response over the course of one hour (Figure 4.1c). This contrasts with the minor turn-off response elicited by water (Figure 4.1b), isolating the analyte as the cause of the turn-on response rather than the addition of volume to the sample. The normalized integrated change in fluorescence ($\Delta F/F_0$) of the sensor peaked after 20 min post-addition of H_2O_2 and remained stable over the course of one hour (Figure 4.1d).

[§] Portions of this chapter are adapted from Ledesma, F. *et al.* Covalent Attachment of Horseradish Peroxidase to Single-Walled Carbon Nanotubes for Hydrogen Peroxide Detection. Preprint at https://doi.org/10.1101/2023.12.14.571773 (2023).

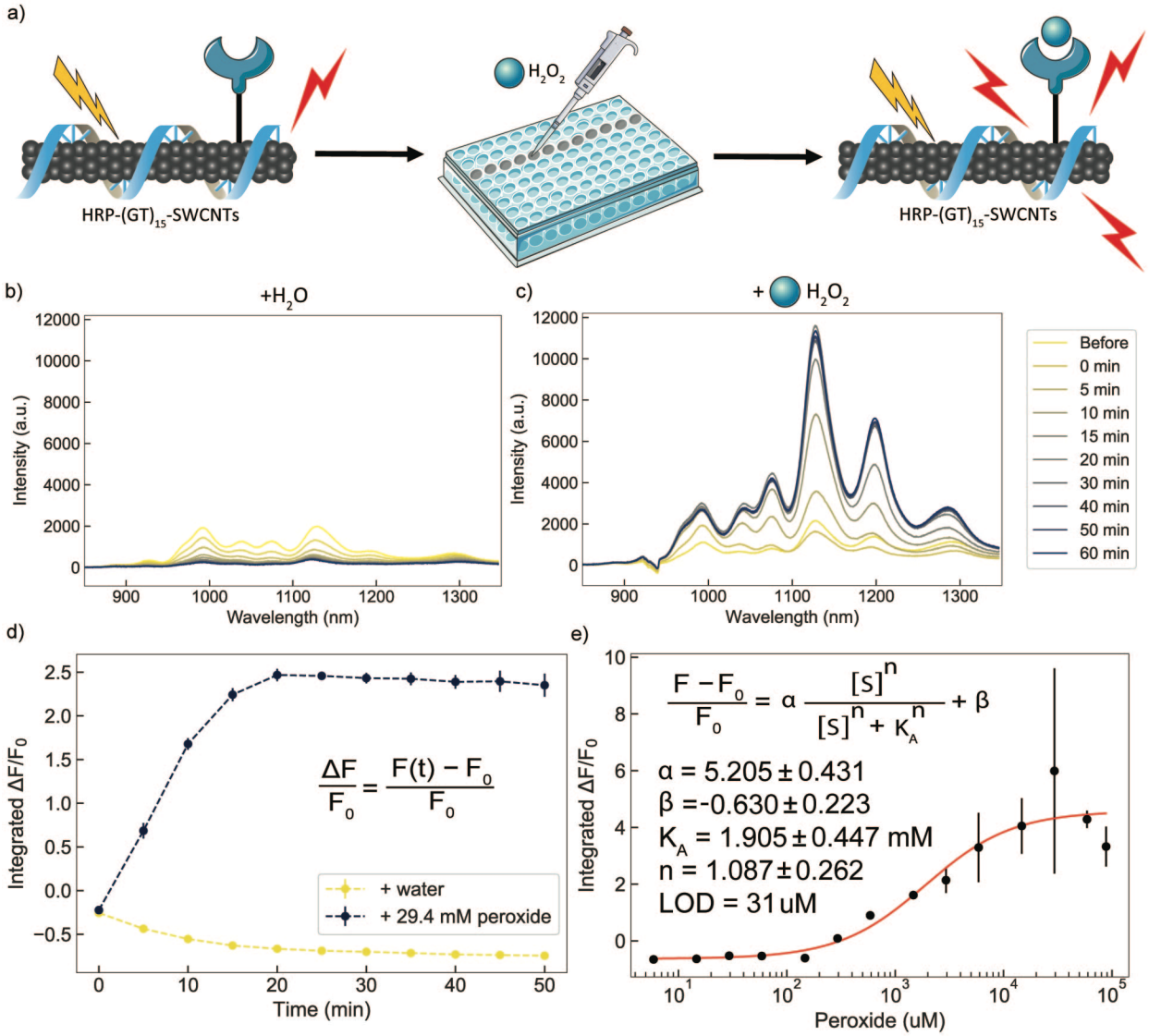

Figure 4.1. HRP-$(GT)_{15}$-SWCNT nanosensor response to H_2O_2 in solution-phase screen. (a) Schematic depiction of response screening platform, where addition of analyte to a 384-well plate with nanosensor induces a strong turn-on response as measured by the increase in nIR fluorescence emission. (b) Nanosensor response to water shows a strong turn-off response over 60 min. (c) Nanosensor response to 29.4 mM H_2O_2 shows a strong turn-on response over 60 min. (d) The normalized integrated change in fluorescence ($\Delta F/F_0$) for (b) and (c). F_0 is set to the integrated fluorescence intensity of the "Before" baseline timepoints in (b) and (c) taken immediately prior to H_2O_2 addition. (e) Endpoint (time = 60 min) $\Delta F/F_0$ values for varying concentrations of analyte plotted and fit to a cooperative binding model. Fit parameters are listed with 95% confidence intervals evaluated using the t-distribution. All fluorescence measurements were obtained with a laser excitation wavelength of 721 nm. Error bars represent the standard deviation between experimental replicates (n = 3).

In contrast, $(GT)_{15}$-SH-SWCNT alone exhibits a turn-off fluorescence response to H_2O_2 (Figure 4.2a), as expected from previous literature.[76] Furthermore, HRP mixed with $(GT)_{15}$-SH-SWCNT

exhibits a strong turn-off response immediately upon H_2O_2 addition followed by a gradual increase in fluorescence to the baseline intensity (Figure 4.2a). This non-monotonic fluorescence modulation could be due to the consumption of H_2O_2 by free HRP, mitigating the analyte's quenching effect as it is depleted from the solution. To confirm this hypothesis, we probed the response of $(GT)_{15}$-SH-SWCNTs to H_2O_2 when mixed with HRP and Catalase, a peroxide-scavenging enzyme, as well as with both proteins inactivated by glutathione (GSH), an inhibitor of HRP enzymatic activity (Figure 4.2b).[85,86] Upon addition of 588 μM H_2O_2 to the Catalase sample, an immediate strong turn-off response is observed followed by a gradual increase in fluorescence. This response is similar to that of HRP mixed with $(GT)_{15}$-SH-SWCNTs, though lesser in magnitude as Catalase is known for having low affinity for H_2O_2 with a K_M value between 10-30 mM which would lead to less peroxide consumption over the same time period compared to HRP, thus lessening the increase in fluorescence. When GSH is added to both samples to inhibit the enzymatic reaction and 588 μM H_2O_2 is added, a strong turn-off response is again observed and remains stable over time as the enzymes are unable to remove the quenching H_2O_2 from solution.

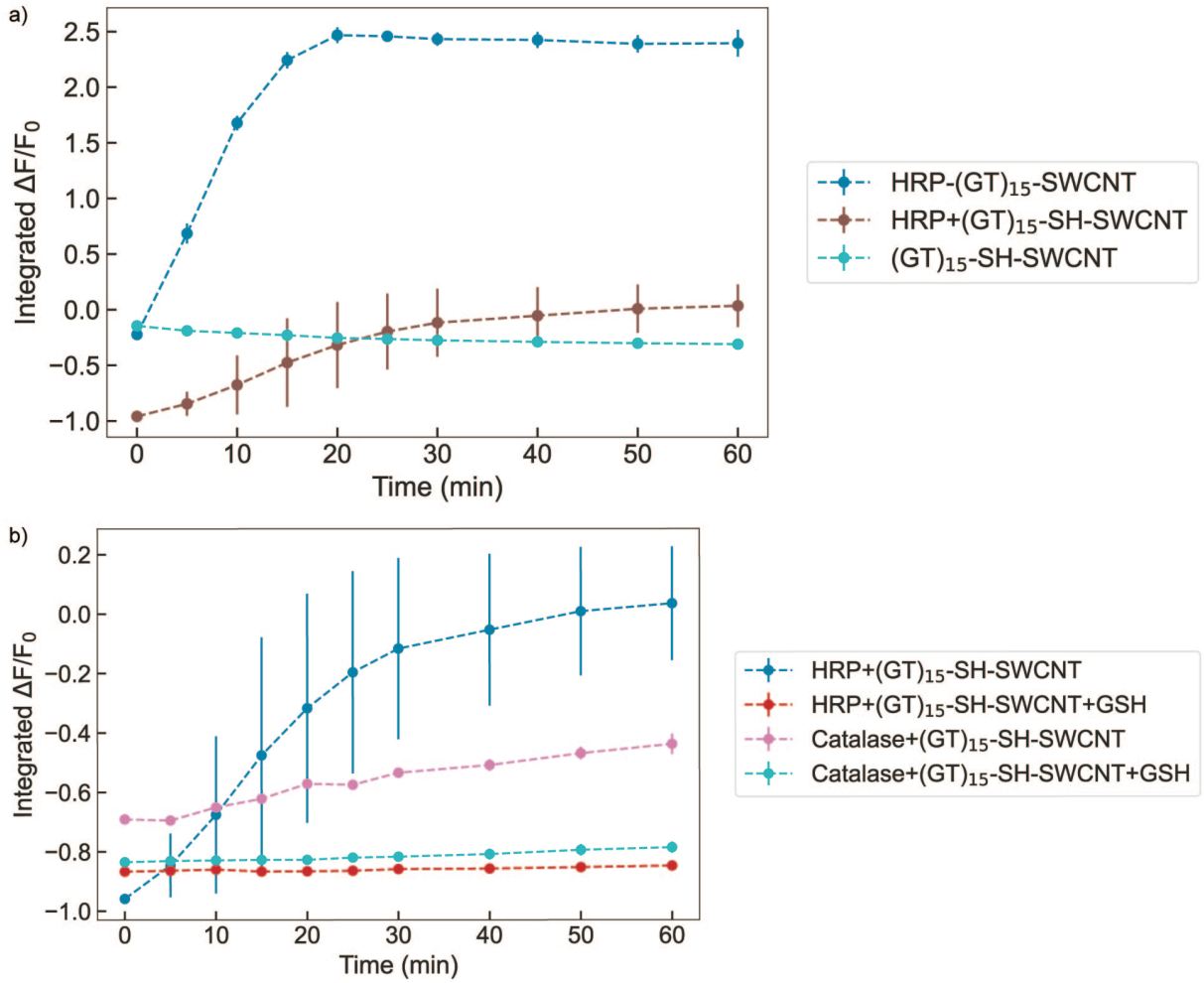

Figure 4.2. HRP-$(GT)_{15}$-SWCNT fluorescence response compared to control conditions. (a) Upon addition of 29.4 mM of H_2O_2, $(GT)_{15}$-SH-SWCNT alone shows a slight turn-off response, replicating results from literature where H_2O_2 in proximity to the SWCNT surface quenches

fluorescence.[76] Addition of 29.4 mM H_2O_2 to a solution of HRP mixed with $(GT)_{15}$-SH-SWCNT yields a strong turn-off response followed by a gradual increase in fluorescence returning to the original baseline intensity. This response could be attributed to the consumption of H_2O_2 by free HRP in the solution, reducing the quenching effect of H_2O_2 as the analyte is depleted. In contrast, HRP-$(GT)_{15}$-SWCNT exhibits a strong and stable turn-on fluorescence response to the same concentration of H_2O_2, highlighting the necessity of covalent HRP conjugation for this nanosensor's response. (b) To elucidate a nanosensor mechanism, $(GT)_{15}$-SH-SWCNTs were mixed with HRP and the peroxide-consuming enzyme Catalase at a concentration of 0.01 mg mL^{-1}. Both samples were also incubated with 1 mM of the known inhibitor glutathione (GSH). The resulting fluorescence responses to 588 μM of H_2O_2 confirm that the initial turn-off response to analyte addition is due to the quenching of SWCNTs by H_2O_2 and subsequent return to baseline fluorescence is a result of scavenging by HRP or Catalase in solution. Error bars represent the standard deviation between experimental replicates (n = 3).

Altogether, this confirms that the response observed by the sample with HRP noncovalently adsorbed to $(GT)_{15}$-SH-SWCNTs is due to consumption of quenching H_2O_2 which returns the sensor to baseline fluorescence. Thus, these results suggest that the strong turn-on response of our sensor must be due to the interaction between H_2O_2 and covalently-attached HRP on the SWCNT surface rather than between H_2O_2 or catalysis reaction byproducts and the SWCNT itself.

Furthermore, we conducted a mock synthesis where the crosslinker Sulfo-SMCC was omitted from the otherwise normal synthesis route and assessed the product (Figure 4.3). The mock SWCNT showed notably lower HRP enzymatic activity than the nanosensor and no turn-on response to H_2O_2, emphasizing the necessity of covalent HRP conjugation to SWCNT via Sulfo-SMCC crosslinker for the nanosensor's function.

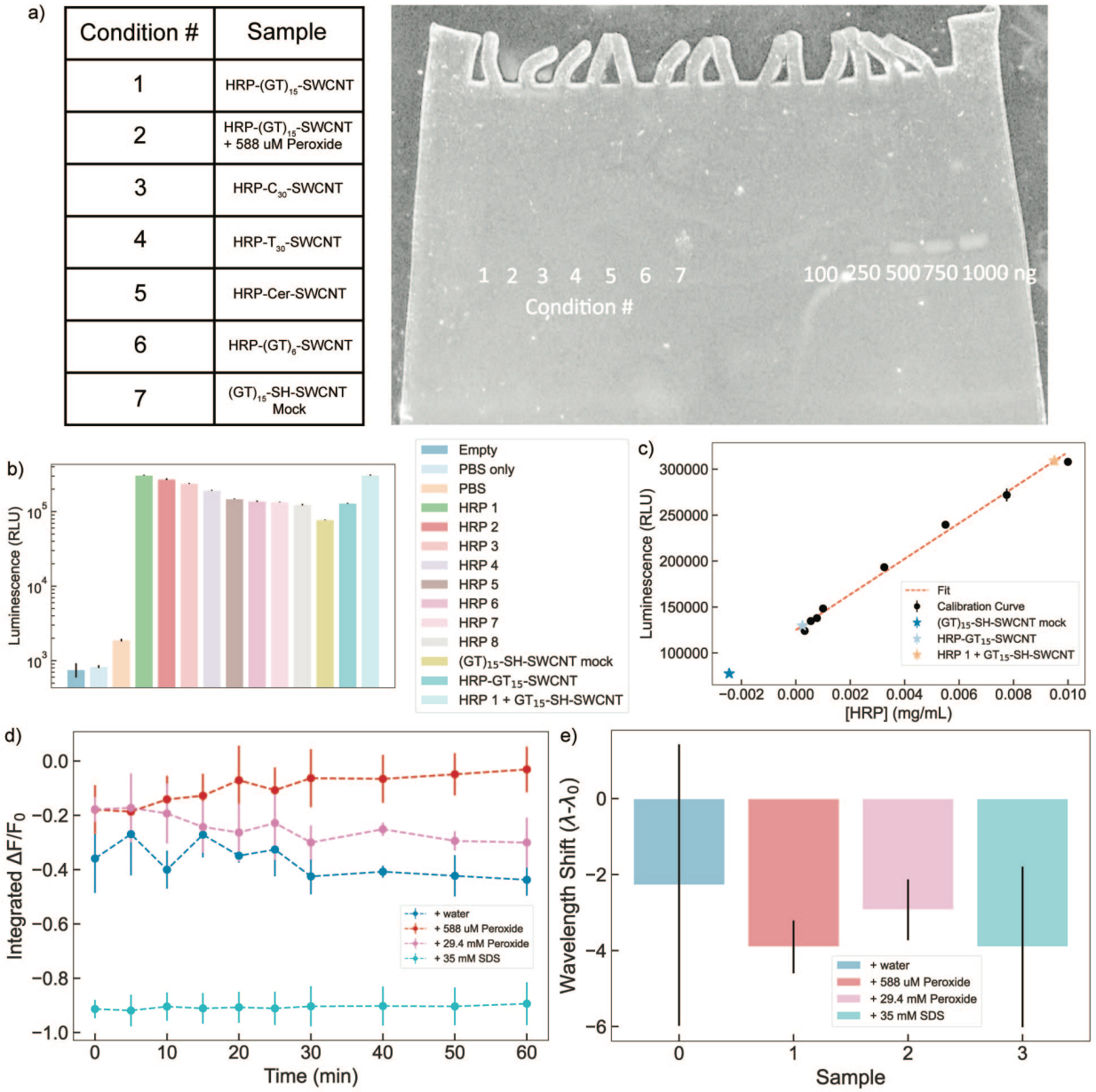

Figure 4.3. Orthogonal validation of covalent HRP conjugation to SWCNT. (a) SDS-PAGE of HRP-SWCNTs shows minimal free protein in solution, < 250 ng or 0.05 mg mL^{-1} since the faintest band that appears in the known calibration curve on the right is 250 ng while no bands appear for the conditions loaded on the left. Additionally, pre-incubation of the nanosensor with H_2O_2 did not cause band appearance as would be expected if the nanosensor response mechanism relied on H_2O_2 inducing desorption of HRP from the SWCNT surface. (b) Luminol activity assay shows $(GT)_{15}$-SH-SWCNT Mock, the SWCNTs taken through the nanosensor synthesis route without the addition of crosslinker SMCC, having much less enzymatic activity than the normal nanosensor though still exhibiting more activity than the negative controls, suggesting a small amount of HRP remains adsorbed to the SWCNT. (c) Using the HRP luminescence calibration curve in (b) to calculate [HRP] in the Mock sample yields a negative concentration. While not useful as a number alone, the difference in calculated concentration to the nanosensor emphasizes the retention of HRP enabled by covalent conjugation. Fluorescence

response profile (d) and solvatochromic shift of the (9,4) chirality peak (e) of Mock SWCNT in response to low and high concentrations of H_2O_2 highlights the importance of covalent conjugation for the observed nanosensor response. Mock SWCNT exhibits no turn-on response to H_2O_2 while exhibiting a similar turn-off response to SDS as $(GT)_{15}$-SH-SWCNTs alone. Additionally, Mock SWCNT exhibit a blue-shift in response to low H_2O_2 whereas the nanosensor in this work exhibits a slight red-shift in response to the same amount of H_2O_2. Error bars represent the standard deviation between experimental replicates (n = 3).

We further measured the concentration-dependent nanosensor response and determined a 31 μM limit of detection (LOD) for hydrogen peroxide (Figure 4.1e). The data was fit to a cooperative binding model and extracted parameters include an equilibrium constant K_A of 1.905 mM and Hill coefficient n of 1.087, as expected of this noncooperative enzyme which uses its heme cofactor to bind one peroxide molecule at a time for catalysis.[88] When compared with similar peroxide sensors, our nanosensor LOD and linear range fall within the range of literature values (Table 1).

Table 4.1. Comparisons of similar H_2O_2 nanosensors found in literature.

Platform	Signal Type	Linear Range (μM)	LOD (μM)	Reference
HRP/Os Polymer	Amperometric	1-500	0.3	[89]
HRP/Au	Amperometric	40-100	40	[90]
SWCNT/GCE	Amperometric	1900-24000	1000	[91]
HRP/Luminol	Chemiluminescence	100-3000	667	[92]
Fe-N-C Nanozyme	Chemiluminescence	500-100000	0.5	[93]
Cobalt-CNT/GOx	Fluorescence	0.2-20	0.1	[94]
ssDNA-SWCNT	Fluorescence	10-1000	0.1	[76]
AgNP	Absorbance	10-10000	10	[95]
HRP-SWCNT	Fluorescence	150-600	31	This work

Abbreviations: Ag, silver; Au, gold; Fe, iron; N, nitrogen; C, carbon; GCE, glassy carbon electrode; GOx, glucose oxidase, Os, Osmium.

Though our nanosensor has a higher LOD and linear range than some systems (Figure 4.4), our system maintains the advantages of facile synthesis, form factor variability, non-photobleaching nature, and an underlying platform that is flexible enough to accommodate other proteins and analytes to generate other nanosensors or multiplexed sensors.

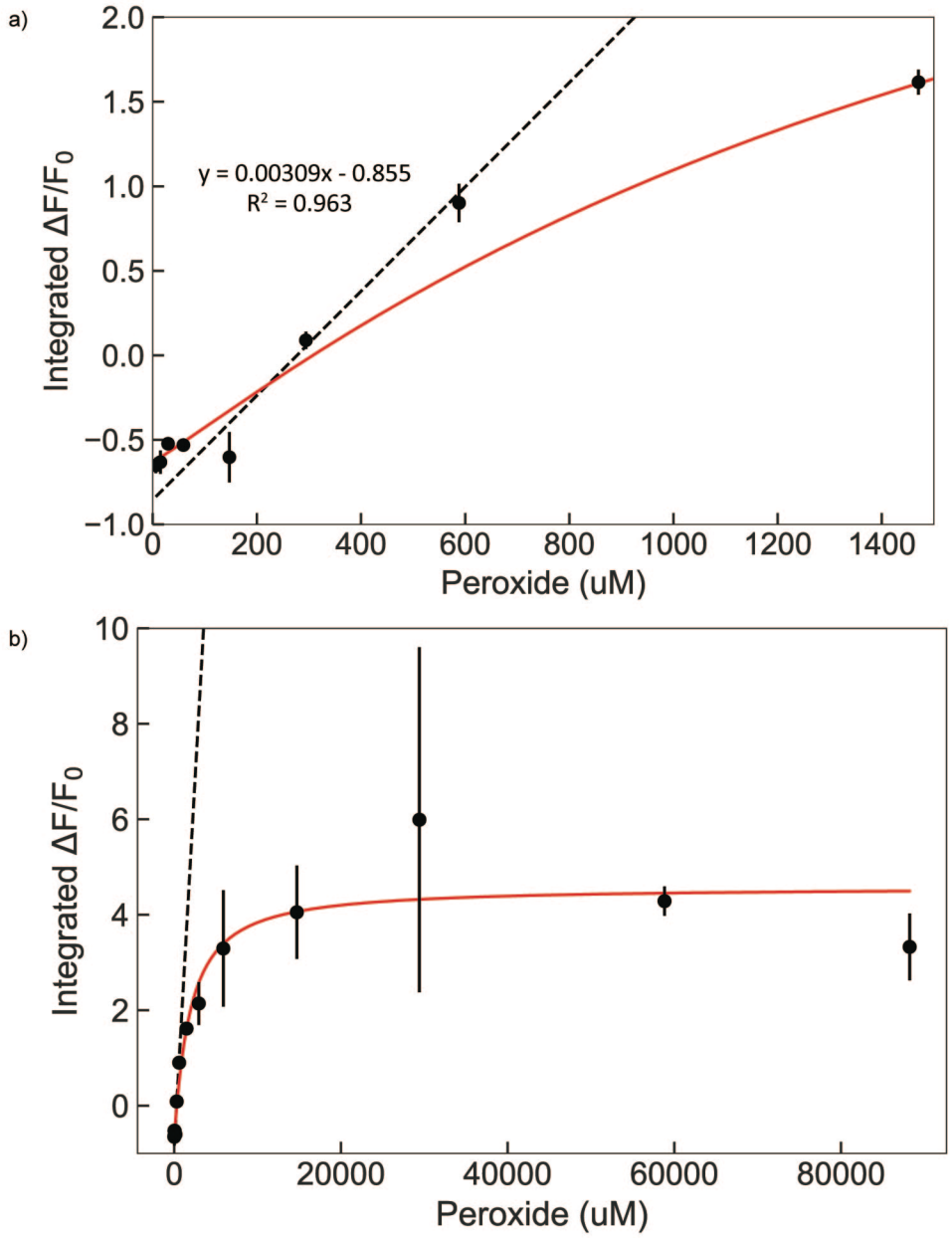

Figure 4.4. Linear range of HRP-$(GT)_{15}$-SWCNT nanosensor. Using weighted least squares regression, every possible set of 3 or more consecutive data points above the limit of detection was fit to a linear equation. (a) The region with the best linear fit as deemed by the highest R^2 value was between data points at 147.1 and 588.2 μM with $R^2 = 0.963$. All data points before the linear region and one data point after are included to demonstrate the deviation from linearity outside the identified range. (b) The plot of all data on a linear plot shows good agreement between the determined linear line and the visually observed region of linearity. Dotted black lines correspond to fitted linear equation and solid red lines correspond to fitted cooperative binding model. Error bars represent the standard deviation between experimental replicates (n = 3).

4.3 Nanosensor Response to H_2O_2 in Immobilized Form

After characterizing the solution-phase nanosensor response, we investigated the nanosensor response when surface-immobilized on a glass microwell dish (Figure 4.5a). HRP-$(GT)_{15}$-SWCNTs were immobilized on a glass microwell dish and imaged after rehydration with PBS over the course of 5 min. Isolating the image analysis to fluorescent HRP-$(GT)_{15}$-SWCNT regions of interest with high fluorescence and averaging their values over time, we demonstrate the nanosensor's ability to sense hydrogen peroxide when immobilized through an imaging format (Figure 4.5b). The addition of water at 60 s shows no measurable fluorescence change, while the addition of 588 µM H_2O_2 at 120 s shows a signal increase of ~15%, with representative images at Frame 9 (Figure 4.5c) and 124 (Figure 4.5d). This response can thus still be attributed to the analyte's presence upon addition rather than volume increases.

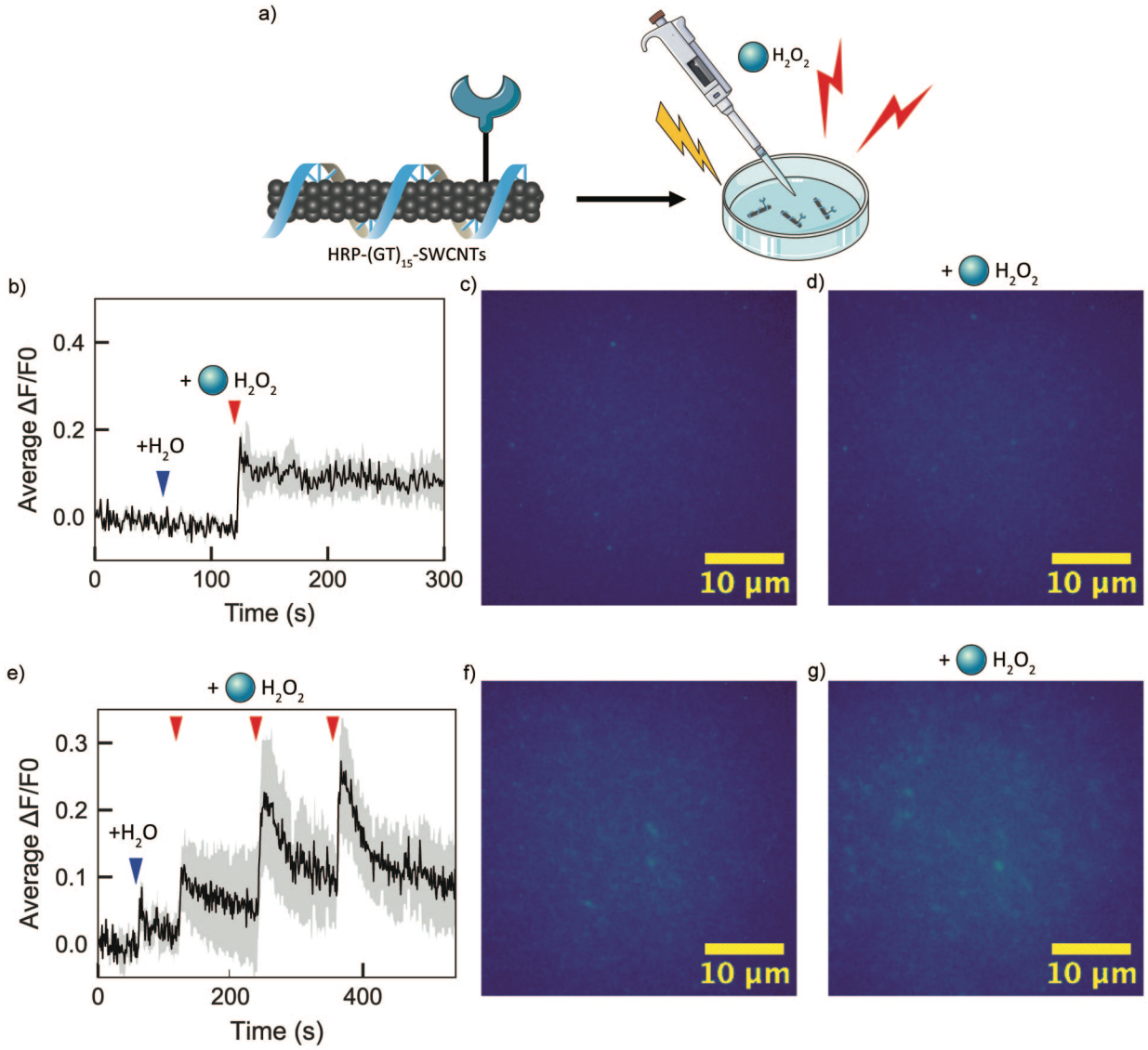

Figure 4.5. Immobilized nanosensor response to H_2O_2. (a) Schematic depiction of immobilized sensing platform, where the nanosensor is incubated in a glass microwell dish for 20 min, washed,

and rehydrated with 1X PBS before analyte addition and imaging. Addition of analyte induces an increase in fluorescence intensity of the sensor. (b) Analysis of fluorescence microscopy images of immobilized nanosensor over 5 min shows around 15% increase in fluorescence intensity corresponding to H_2O_2 addition at 120 s. (c) Fluorescence microscopy image of immobilized nanosensor at 9 s post-hydration with PBS. (d) Fluorescence microscopy image of immobilized nanosensor at 4 s post-addition of H_2O_2 shows increased fluorescence intensity compared to (c). (e) Analysis of fluorescence microscopy images of immobilized nanosensor over 10 min shows repeatable fluorescence intensity increase upon subsequent additions of H_2O_2. (f) Fluorescence microscopy image of immobilized nanosensor at 9 s post-hydration with PBS. (g) Fluorescence microscopy image of immobilized nanosensor at 4 s post the third addition of H_2O_2 shows increased fluorescence intensity compared to (f). Gray shaded areas represent the standard deviation from the mean value in black (n=20). Average fluorescence change values in (b) and (e) are calculated using ROIs from the entire image field of view. Images in (c), (d), (f), and (g) are representative images highlighting the center of the field of view and capture fluorescence intensity emitted by the SWCNTs from 900-1700 nm through a 900 nm long-pass filter.

Further, the repeatability of this response can be seen by the similar sharp increases in fluorescence upon subsequent additions of H_2O_2 every 120 s (Figure 4.5e). The fluorescence intensity increases for each addition by a similar magnitude, suggesting that the consumption of analyte by HRP is modulating SWCNT fluorescence intensity rather than an interaction between the analyte or reaction byproducts and the SWCNT itself. The signal fails to fully return to baseline between analyte additions likely due to imaging drift, where the addition of buffer and analyte to the microwell dish adds weight that shifts the imaging plane downwards from its original location, causing a drift in the measured baseline intensity. The visual presence of SWCNTs in the image after H_2O_2 addition (Figure 4.5g) confirms that the immobilized nanosensors are not degrading over the course of the experiment, as does the persistence of stable spectroscopy nanosensor fluorescence (Figure 4.1d). The difference in magnitude of fluorescence modulation between the solution phase HRP-$(GT)_{15}$-SWCNT nanosensor response to hydrogen peroxide and this immobilized form factor can be attributed to the difference in analysis between the two. In solution, the fluorescence is measured for each wavelength in the nIR region, whereas the immobilized form factor captures fluorescence images of the sample, aggregating the total emission over the nIR region into an image. The solution-phase response is stronger at certain nIR wavelengths (Figure 4.1c), corresponding to different chirality SWCNTs. This sensitivity is lost in the images as they only capture overall emission, limiting the magnitude of the response to the same concentration of H_2O_2.

4.4 Confirming Nanosensor Selectivity for ROS

Following successful demonstration of the surface-immobilized nanosensor, we next characterized the HRP-$(GT)_{15}$-SWCNT nanosensor's selectivity for H_2O_2 against a panel of relevant analytes (Figure 4.6). These analytes were chosen to both ensure that the catalysis of H_2O_2 was the sole signal source rather than similar structural analogues (TBHP) or downstream reaction intermediates (superoxide), and to evaluate the potential interference of biomolecules that would be present during *in vitro* sensing applications (GSH and sodium hypochlorite).

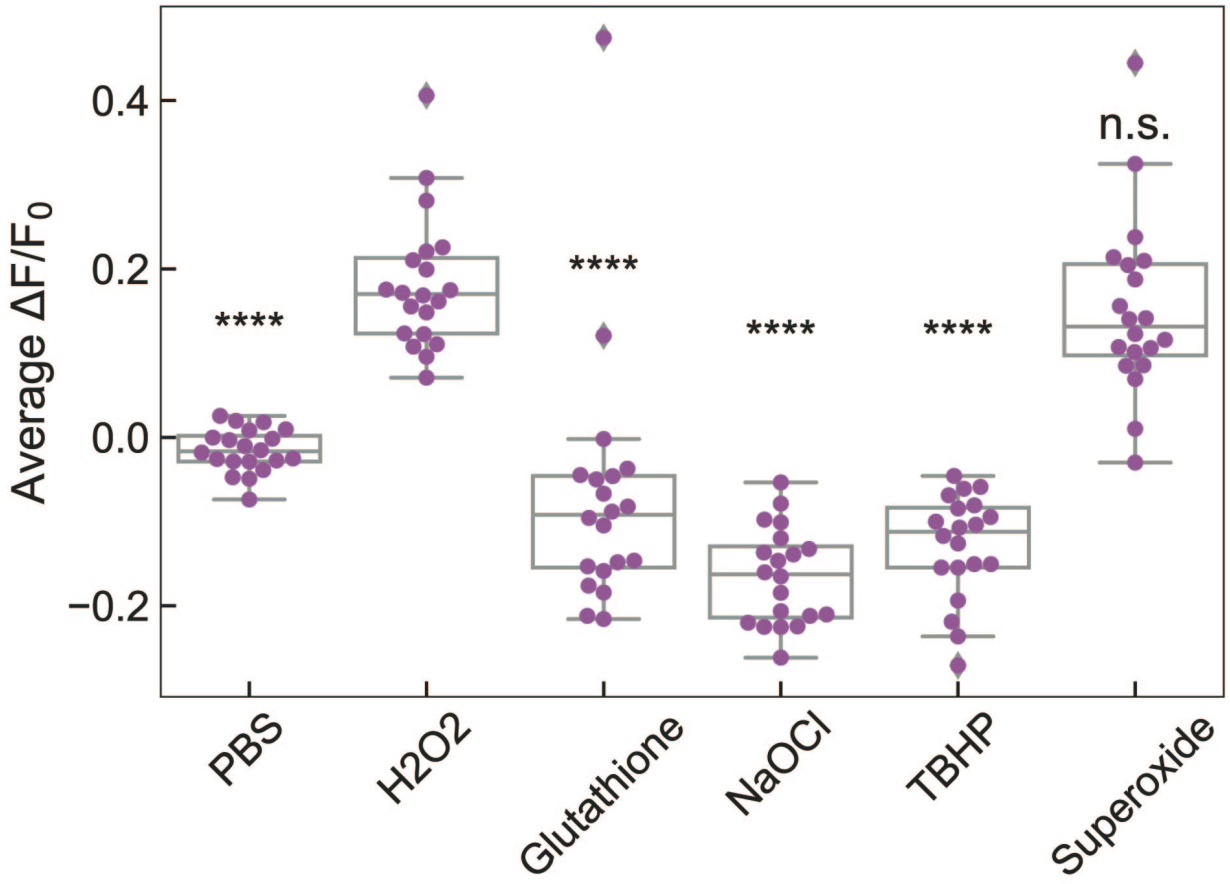

Figure 4.6. Nanosensor selectivity against relevant analytes. Normalized change in fluorescence values of nanosensor immobilized on glass upon addition of analytes shows minimal response for analytes other than the target. Fluorescence change for each ROI (n=20) 10 s after analyte addition is plotted as purple circles for each condition. ****P = 3.35 x 10^{-9} (PBS), 1.64 x 10^{-13} (Glutathione), 2.26 x 10^{-14} (NaOCl), and 2.26 x 10^{-14} (TBHP), and P = 0.89 (Superoxide) in independent two-sample *t* tests for each analyte $\Delta F/F_0$ in comparison to H_2O_2.

Compared to buffer and H_2O_2 control, the addition of 50 μM of GSH, NaOCl, and TBHP produced either no response or a turn-off response. The addition of 50 μM of superoxide did produce a turn-on response similar to H_2O_2, though this result is expected as superoxide bound to the heme core of HRP is an intermediate of the enzyme's catalytic cycle (Compound III), supporting our proposed mechanism for the nanosensor discussed later in Section 4.5.[96,97] Altogether, our nanosensor appears to be selective for ROS over other potential interfering species, further confirming the necessity of HRP-analyte interaction for the observed fluorescence turn-on response. Given the ease of preparation and screening, further relevant analytes can be quickly assayed depending on the intended application of a nanosensor generated with this platform.

4.5 Nanosensor Mechanism Investigation

To probe a potential mechanism for the nanosensor's turn-on response, we investigated the response to H_2O_2 when subjected to various conditions including high and low pH, high and low

ionic strength, incubation with GSH, and incubation with Catalase. We hypothesize that the nanosensor would respond differently to H_2O_2 under these conditions by affecting HRP enzymatic activity, thus confirming the reliance on HRP enzymatic activity for the observed fluorescence turn-on response. Increasing or decreasing pH and ionic strength would increase or decrease HRP activity, respectively, the addition of GSH would inhibit enzymatic activity, and the addition of catalase would provide an additional H_2O_2 scavenger, reducing the amount of H_2O_2 available in solution for catalysis by HRP. The nanosensor responds to H_2O_2 similarly in 1X PBS and 1 M NaCl, representing a higher ionic strength buffer than 1X PBS at 150 mM NaCl (Figure 4.7a). In contrast, the nanosensor shows no response in the low ionic strength conditions of 10 mM NaCl and the zwitterionic buffer HEPES. Since previous studies have reported better HRP enzymatic activity in higher ionic strength conditions,[98,99] these results point towards the catalytic reaction as the source of the fluorescence mechanism. Furthermore, the sensor shows no response in pH 5 PBS, a normal response at pH 7, and a fast and high magnitude response at pH 9. This supports previous studies that found minimal HRP enzymatic activity at acidic pH and peak enzymatic activity from pH 8-9, as the pK_a of HRP is ~8.6.[98–100] Together, these results suggest that the optimal conditions for nanosensor response are at high pH and ionic strength, conditions that optimize HRP enzymatic activity. Therefore, mechanistically, these results support a nanosensor mechanism whereby HRP enzymatic consumption of H_2O_2 drives an increase in SWCNT fluorescence.

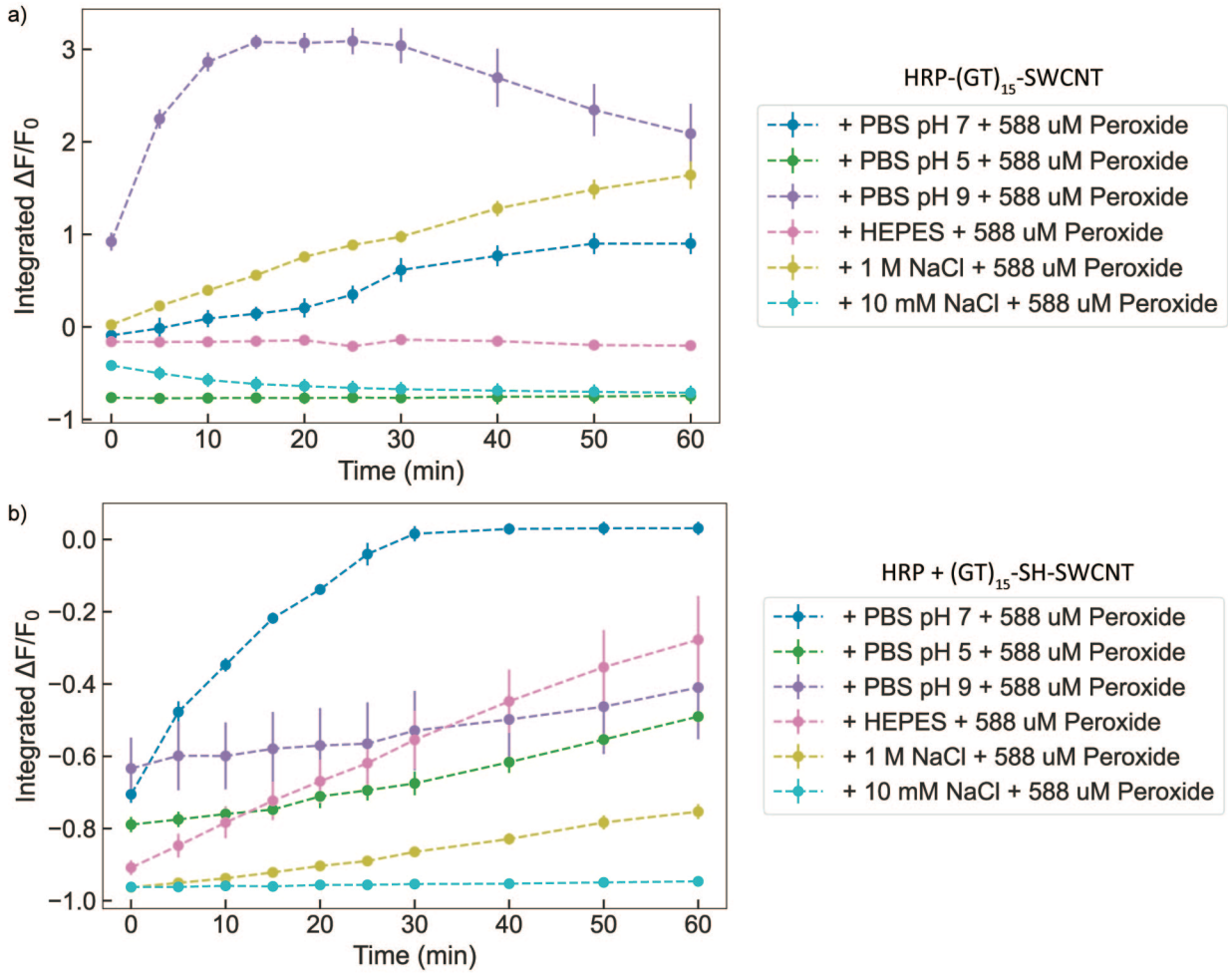

Figure 4.7. HRP-$(GT)_{15}$-SWCNT nanosensor response in various pH and ionic strength conditions. (a) Compared to the response to 588 μM of H_2O_2 in the ionic strength of 1X PBS (150 mM NaCl), the nanosensor responds similarly in higher ionic strength conditions of 1 M NaCl in PBS and shows no response in the low ionic strength buffers of 10 mM NaCl in PBS and the zwitterionic buffer HEPES. Interestingly, the nanosensor shows a faster and higher magnitude response to the same amount of H_2O_2 in PBS at pH 9 than at pH 7. This could be attributed to the pK_a of HRP at 8.6, resulting in a higher enzymatic activity at pH 9 than at pH 7, leading to a faster response. (b) The response to 588 μM of H_2O_2 at the same conditions as in (a) was assessed for HRP noncovalently mixed with the starting material $(GT)_{15}$-SH-SWCNT. All conditions exhibited an initial large turn-off response to H_2O_2 followed by varying degrees of return to baseline as the quenching H_2O_2 is removed from solution. No conditions produced a turn-on response like the covalently-conjugated nanosensor, with only the pH 7 condition fully returning to baseline fluorescence. Error bars represent the standard deviation between experimental replicates (n = 3).

To further support this mechanistic nanosensor function, when HRP is noncovalently mixed with SWCNTs in the aforementioned conditions rather than covalently attached to the SWCNT surface as in our nanosensor, the noncovalently mixed samples show no turn-on response (Figure 4.7b). Lastly, as an orthogonal method to support this nanosensor's mechanism, our corona exchange assay (Figure 2.5) and filtration of free HRP (Figure 2.8) indicate minimal/no free HRP adsorption to SWCNTs. Taken together, these results further support that the sensing mechanism relies on the interaction between HRP and SWCNTs near the SWCNT surface enabled by covalent conjugation of HRP to the SWCNT surface.

This hypothesis is further supported by investigating the nanosensor response when incubated with GSH to inhibit HRP activity and Catalase as a separate H_2O_2 scavenger (Figure 4.8). Incubation with 1 mM GSH for 1 hour prior to testing completely negates the nanosensor's turn-on response to H_2O_2, further suggesting that HRP enzymatic activity is necessary to modulate SWCNT fluorescence. Furthermore, addition of 0.01 mg mL^{-1} Catalase to the nanosensor shows a slower and lower magnitude turn-on response to H_2O_2 compared to the nanosensor alone, likely due to Catalase catalyzing and thus reducing the available H_2O_2 in solution for consumption by HRP on the nanosensor. The addition of free HRP to the sample at 0.01 mg mL^{-1} does not impact the nanosensor's response profile to H_2O_2, as it reaches the same peak fluorescence over the same period, highlighting the reliance of HRP proximity to the SWCNT surface for the turn-on response rather than attributing the nanosensor response to reaction byproducts or H_2O_2 consumption by free/adsorbed HRP.

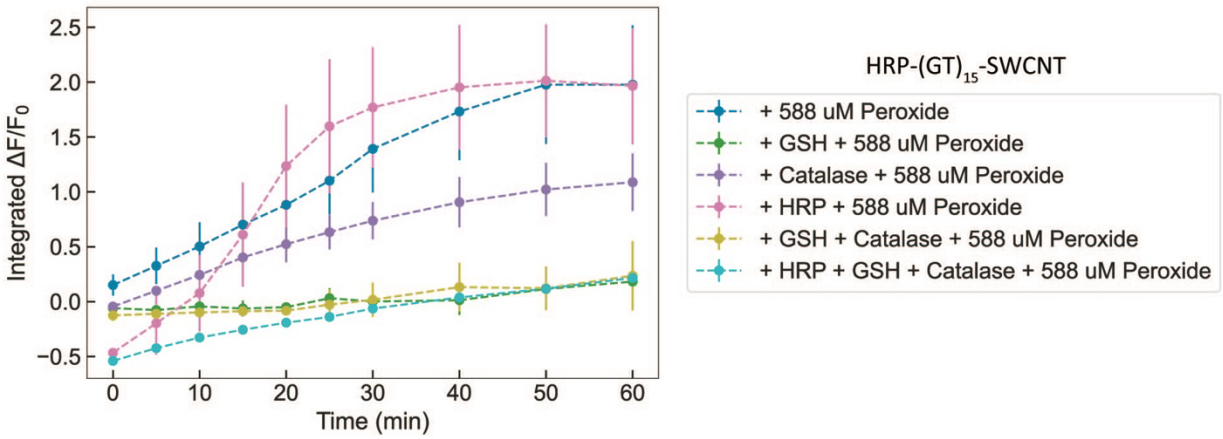

Figure 4.8. HRP-$(GT)_{15}$-SWCNT nanosensor response to various analytes to determine nanosensor mechanism. HRP-$(GT)_{15}$-SWCNTs show a similar response profile to 588 μM of H_2O_2 alone as they do when incubated with 0.01 mg mL^{-1} of HRP, emphasizing the mechanism's reliance on HRP near the SWCNT surface for fluorescence modulation. Similarly, HRP-$(GT)_{15}$-SWCNTs incubated with 0.01 mg mL^{-1} of Catalase show an attenuated turn-on response to 588 μM of H_2O_2. When incubated with 1 mM Glutathione, a known inhibitor of HRP enzymatic activity, the nanosensor's response is negated. Adding each combination of GSH, Catalase, and HRP to the nanosensor also shows no turn on response. Error bars represent the standard deviation between experimental replicates (n = 3).

With these results in hand, the remaining possible mechanisms for the turn-on response of the nanosensor can be narrowed down to: (i) the redox charge state of the heme center of HRP existing at a state that enhances SWCNT fluorescence emission, (ii) conformational change of HRP during the catalytic cycle causing ssDNA to shift on the SWCNT surface leading to increased fluorescence emission, or (iii) HRP destruction/denaturation causing a return to SWCNT alone baseline fluorescence without the quenching effect of HRP in proximity to the SWCNT surface. To evaluate the impact of these potential mechanistic contributions to our nanosensor response, we can, respectively: (i) pre-incubate the nanosensor with varying levels of H_2O_2 and test the subsequent response to varying levels of H_2O_2 to determine if HRP is induced to the inactive forms of Compound III or P-670 as described in previous literature,[101] (ii) compare the nanosensor's response to H_2O_2 when wrapped with other polymers including ssDNA sequences of the same (C_{30} and T_{30}) and different ($(GT)_6$) length as $(GT)_{15}$, and the amphiphilic lipid C_{16}-PEG(2000)-Ceramide, and (iii) assess the nanosensor's response to a protein denaturant such as SDS which is known to denature HRP.[102]

4.5.1 Mechanism (i): HRP Heme Redox State

Regarding Mechanism (i), extensive studies have been conducted to understand the catalytic cycle of HRP and the resulting oxidation state of the heme center at each intermediate stage in the cycle. Briefly, researchers have identified four possible intermediate redox states for the heme center of HRP during the catalytic cycle: Compound I, Compound II, Compound III, and P-670.[103] The typical catalytic cycle involves fast conversion to Compound I then Compound II, followed by decay to native enzyme. However under certain conditions, the enzyme can be converted to primarily Compound III, a catalytically inactive intermediate.[104] From this state, Compound III

either slowly decays back to the native enzyme or irreversibly inactivates to its P-670 form. In particular, researchers have investigated various mechanisms for inducing HRP inactivation including heme destruction,[105] acid treatment,[106] ionizing radiation,[107] and excess H_2O_2 with no exogenous substrates,[101,108–110] as is the case with our system. We hypothesize that should Mechanism (i) be contributing to the nanosensor response, HRP on the nanosensor would be rapidly converted to Compound III or P-670 upon the addition of high H_2O_2 (29.4 mM) and this process would occur much slower at low H_2O_2 (588 µM), explaining the differences in both time and magnitude of the nanosensor's response profile in both cases. Additionally, subsequent additions of H_2O_2 to samples that have already been treated with high and low levels of H_2O_2 would induce either no response or an attenuated response, respectively, if the enzymes were indeed inactivated. The nanosensor indeed shows the described response profile, exhibiting a rapid and high magnitude increase in fluorescence in response to 29.4 mM H_2O_2, reaching its peak increase around 15 min post-addition and around 450% fluorescence increase over baseline (Figure 4.9). Interestingly, when pre-treated with 29.4 mM H_2O_2, the nanosensor exhibits no turn-on response to both 29.4 mM and 588 µM H_2O_2, suggesting that this high amount of H_2O_2 inhibits subsequent HRP activity, supported by literature findings that excess H_2O_2 induces HRP to the Compound III and P-670 inactive states at $[H_2O_2] > 1$ mM.[101] By contrast, the nanosensor reaches a peak fluorescence increase of around 100% after 60 min in response to 588 µM H_2O_2. When the nanosensor is pre-treated with 588 µM H_2O_2 for 1 hour before screening, the nanosensor exhibits a similar response profile to 29.4 mM H_2O_2, though slower and lower in magnitude than the response without this pre-treatment, reaching a peak of ~375% increase after 30 min. This result suggests that 588 µM H_2O_2 is not enough to fully inhibit HRP activity by converting the redox state to Compound III or P-670 since it still responds to 29.4 mM H_2O_2.

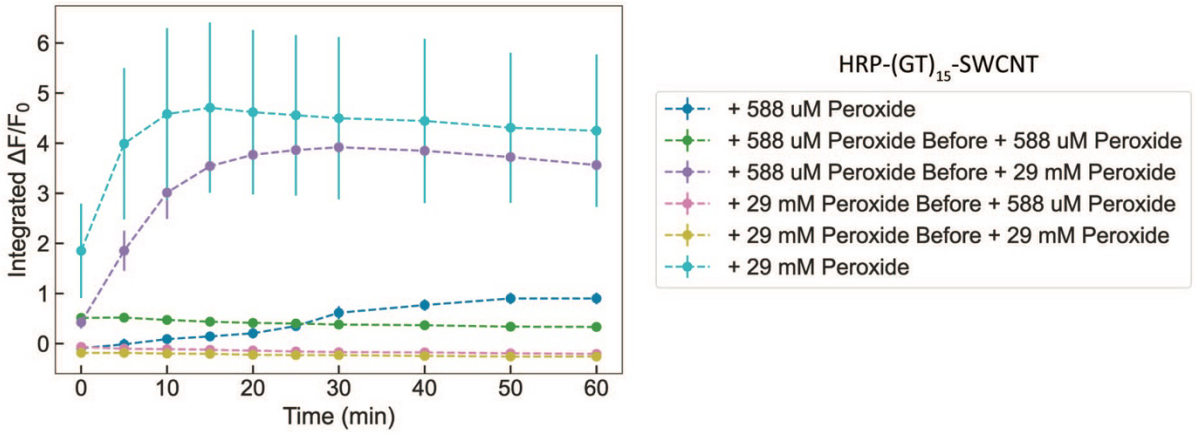

Figure 4.9. HRP-$(GT)_{15}$-SWCNT nanosensor response to various levels of H_2O_2 to determine nanosensor mechanism. HRP-$(GT)_{15}$-SWCNTs show the strongest turn-on response to 29.4 mM H_2O_2 as shown. This response is slightly attenuated though not completely negated when the nanosensor is incubated with 588 µM of H_2O_2 for 1 hour pre-screening ("Before"). In contrast, when the nanosensor is incubated with 29.4 mM H_2O_2 for 1 hour pre-screening, the nanosensor shows no response to 29.4 mM H_2O_2. Low amounts of H_2O_2 do not lead to this inactivation, as the additions of 588 µM and 29.4 mM H_2O_2 both induce turn-on responses when the nanosensor is incubated with 588 µM of H_2O_2 prior to screening. Error bars represent the standard deviation between experimental replicates (n = 3).

On the other hand, the response to 588 μM H_2O_2 after pre-treatment with the same amount of H_2O_2 shows a decreased, but faster turn-on response of about 50% at 0 min and remains stable for 60 min. If this response was due to cycling of the heme redox state back to native enzyme rather than settling at one state, this response would be expected to decrease back to baseline fluorescence as H_2O_2 is depleted. However, the stability of both this response and that of 29.4 mM H_2O_2 alone potentially indicates a reliance on the generation of Compound III or P-670 forms of HRP for fluorescence modulation. The magnitude of the response could thus be proportional to the fraction of HRP on SWCNT converted to these redox states and the kinetics of the response would depend on the concentration of H_2O_2 as we observe in Figure 4.9.

To determine if Compound III or P-670 dominates the HRP heme redox state when our nanosensor exhibits a turn-on response, we investigated the nanosensor response to H_2O_2 in the presence of salicylic acid (SA) (Figure 4.10). SA is known to induce P-670 formation at high H_2O_2,[111,112] so if P-670 formation is the source of fluorescence modulation in the nanosensor, the previously observed nanosensor response profile would be observed for pre-treatment with 29.4 mM H_2O_2 for 1 hour before screening to induce Compound III formation followed by addition of 1 mM SA. However, nanosensor pre-treatment with 29.4 mM and 588 μM H_2O_2 showed no response to SA, while pre-treatment with SA only induced a response for 29.4 mM H_2O_2. Additionally, addition of SA alone showed no turn-on response.

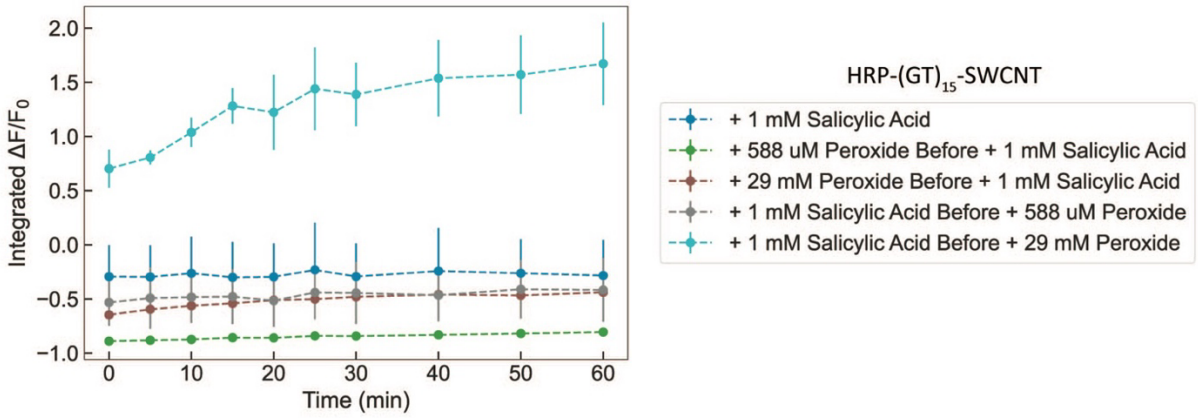

Figure 4.10. HRP-$(GT)_{15}$-SWCNT nanosensor response to salicylic acid to determine nanosensor mechanism. Nanosensor incubation with a low (588 μM) and high (29.4 mM) amount of H_2O_2 for 1 hour prior to adding 1 mM salicylic acid, should first induce Compound III formation followed by P-670 formation. Neither of these conditions produced a turn-on response, eliminating P-670 formation as the mechanism source. Furthermore, incubating the nanosensor with 1 mM salicylic acid followed by screening with 588 μM and 29.4 mM H_2O_2 showed no turn-on response and a rapid but attenuated turn-on response, respectively. Error bars represent the standard deviation between experimental replicates (n = 3).

Together, these results suggest that HRP on the nanosensor is primarily induced to Compound III in the presence of high H_2O_2 rather than irreversibly inactivated to P-670. Several studies also suggest the decay of Compound III to P-670 without SA present occurs on the order of hours, further supporting Compound III as the primary state of HRP in the nanosensor.[101,112] We

hypothesize that the proximity of the HRP heme center to the SWCNT may be close enough to enhance fluorescence emission, though investigating the specific physical mechanism of how this charged radical group influences SWCNT fluorescence is beyond the scope of this dissertation. The structure of Compound III is typically represented as a superoxide anion bound to the Ferric heme center, so this negatively charged radical group could potentially negate the charge-trapping effect of the heme iron on SWCNT excitonic recombination, increasing SWCNT fluorescence. Additionally, there is the possibility that superoxide can be released from the heme center and interact with SWCNTs, causing fluorescence modulation. However, our previous data showing that free HRP mixed with $(GT)_{15}$-SH-SWCNTs do not exhibit the same strong turn-on response to H_2O_2 as the nanosensor eliminates the possibility that superoxide anion released from Compound III induces fluorescence modulation (Figure 4.7). Additionally, our data assessing nanosensor selectivity in Section 4.3 supports the formation of Compound III as the mechanism, since the addition of superoxide to the nanosensor induces a turn-on response, suggesting direct formation of Compound III causing a turn-on response (Figure 4.6).

Furthermore, direct addition of superoxide to $(GT)_{15}$-SH-SWCNTs alone does not induce fluorescence modulation (Figure 4.11b), pointing the nanosensor's mechanism towards Compound III on the SWCNT surface enhancing SWCNT fluorescence emission. Previous literature suggests that redox active compounds like ascorbic acid induce a turn-on fluorescence response for ssDNA-SWCNTs, supporting the proposed mechanism.[45]

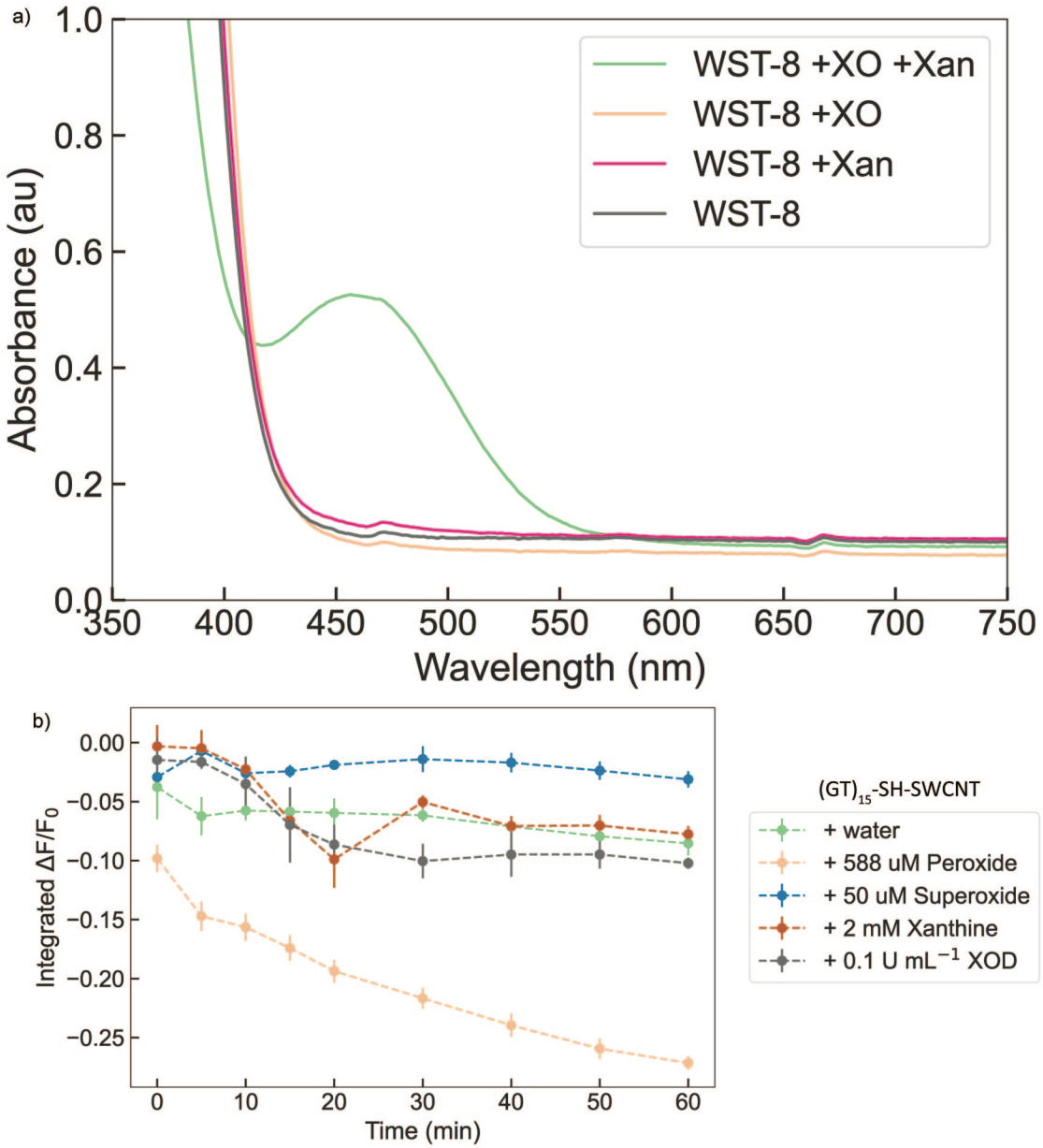

Figure 4.11. Validation of enzymatic superoxide generation with Xanthine/Xanthine Oxidase system and WST-8 and response of SWCNTs alone to superoxide. (a) Absorbance spectra for WST-8 is assessed alone, with Xanthine, with Xanthine Oxidase, and with both components. When superoxide is present, WST-8 is converted to WST-8 formazan, which exhibits an absorbance peak at 460 nm.[113] This peak at 460 nm is only evident when both Xanthine Oxidase and Xanthine are present, confirming the generation of superoxide under these conditions. (b) To ensure nanosensor response is not driven by HRP catalysis reaction byproducts, of which superoxide is one, the Xanthine/Xanthine Oxidase system and its components are screened as analytes with $(GT)_{15}$-SH-SWCNTs. Water and H_2O_2 expectedly exhibit no response and a turn-off response, respectively, while superoxide and the individual components to generate it all induce no response, confirming that the mechanism for the nanosensor in this work does not rely on superoxide generation/interaction with SWCNTs.

4.5.2 Mechanism (ii): HRP Catalysis Induces ssDNA Conformational Change

If Mechanism (ii) is contributing to the response of the nanosensor, the response to H_2O_2 would vary greatly depending on the identity of the amphiphilic polymer used to impart colloidal stability to the SWCNTs. To investigate this, we prepared covalent HRP-SWCNTs with $(GT)_{15}$, C_{30}, T_{30}, Ceramide, and $(GT)_6$ as dispersants and assessed their responses to 588 μM H_2O_2 (Figure 2.7a). Compared to the nanosensor, HRP-C_{30}-SWCNTs and HRP-$(GT)_6$-SWCNTs exhibited the closest response profile, though HRP-C_{30}-SWCNTs reached its peak fluorescence increase at around 75% after 5 min, while the nanosensor and HRP-$(GT)_6$-SWCNTs reached peaks of 90% and 60 % after 60 and 30 min, respectively. By contrast, HRP-Cer-SWCNTs showed no fluorescence modulation in response to H_2O_2, potentially validating Mechanism (ii) as at least a partial contributor to the sensing mechanism. Interestingly, HRP-T_{30}-SWCNTs showed an immediate but small turn-on response to H_2O_2, increasing about 18% immediately and remaining stable over 60 min. This discrepancy in response despite being a DNA sequence of similar length as $(GT)_{15}$ could be attributed to low colloidal stability of the final product as seen by the disappearance of characteristic SWCNT absorbance peaks in the UV-Vis-IR absorbance spectra of HRP-T_{30}-SWCNTs (Figure 2.6b). However, if ssDNA is indeed perturbed by the catalysis of H_2O_2 by HRP and thus modulating SWCNT fluorescence, the SWCNT local dielectric environment would be altered and we would expect to see an accompanying solvatochromic shift in peak intensity wavelengths of each sample that exhibits a turn-on response. We assessed this possibility by plotting the shift in peak wavelength for the (9,4) chirality SWCNT (Figure 2.7c), which typically appears as the highest fluorescence intensity peak around 1135 nm due to our excitation laser wavelength of 721 nm as seen in the strongly quenched baseline sensor fluorescence spectra (Figure 2.7b). Comparing the solvatochromic shifts of nanosensor constructs that exhibited a turn-on response to H_2O_2 after 60 minutes, no clear trend or dependence is seen. HRP-$(GT)_{15}$-SWCNTs show a red-shifted response, HRP-C_{30}-SWCNTs exhibits almost no solvatochromic shift, and HRP-$(GT)_6$-SWCNTs show a slight blue-shift response. By contrast, both HRP-T_{30}-SWCNTs and HRP-Cer-SWCNTs show slight blue-shifts in the (9,4) chirality wavelength despite showing minimal or no response to H_2O_2, respectively. Taken together, these results help eliminate Mechanism (ii) as a potential contributor to the observed turn-on response as the identity of the ssDNA dispersant does not significantly affect the turn-on response capability, mostly serving to impart colloidal stability on the final nanosensor constructs.

Notably, the lack of H_2O_2 response by HRP-Cer-SWCNTs without the possibility of Mechanism (ii) warrants further investigation. This could potentially be attributed to the structure of Ceramide when wrapped around SWCNTs, where the large hydrophobic lipid tails coating the nanotube surface and bulky solvent-exposed polyethylene glycol chains could sterically inhibit either analyte access to HRP or HRP physical movement needed for analyte consumption. However, despite exhibiting no turn-on fluorescence response, HRP-Cer-SWCNTs still show HRP enzymatic activity via the luminol activity assay (Figure 4.3a). As discussed earlier, we are confident that few noncovalently adsorbed or free in solution HRP remains on SWCNTs post-synthesis, suggesting that Ceramide minimally interferes with HRP's catalytic function. In the frame of Mechanism (i), a possible explanation remains that HRP in Compound III form upon H_2O_2 addition facilitates either redox charge transfer to or otherwise influences nearby DNA bases, which has been shown in previous literature identifying particularly the guanine nucleotide as an oxidation sink, leading to fluorescence modulation.[45,114] Ceramide is presumably less redox active in this sense,

potentially explaining the lack of fluorescence modulation in response to H_2O_2 despite demonstrated HRP enzymatic activity.

4.5.3 Mechanism (iii): HRP Destruction/Denaturation Returns SWCNT to Baseline Fluorescence

Finally, if Mechanism (iii) was significantly contributing to the observed nanosensor fluorescence response, we expect that the addition of a protein denaturant such as SDS would exhibit a response profile like that of H_2O_2, identifying the destruction of HRP quenching SWCNT fluorescence as the mechanistic source. Compared to the nanosensor's fast response to 29 mM H_2O_2, the addition of 35 mM SDS to the nanosensor exhibited a linear increase in fluorescence over 60 minutes towards a similar magnitude endpoint (Figure 4.12a). This response was mirrored by HRP-C_{30}-SWCNT showing a similar linearity in fluorescence increase and HRP-$(GT)_6$-SWCNT exhibiting a lower magnitude but faster turn-on response, reaching peak fluorescence after 30 minutes. Notably, these three HRP-SWCNT constructs were also the only ones responsive to H_2O_2, while HRP-T_{30}-SWCNTs and HRP-Cer-SWCNTs again showed no turn-on response.

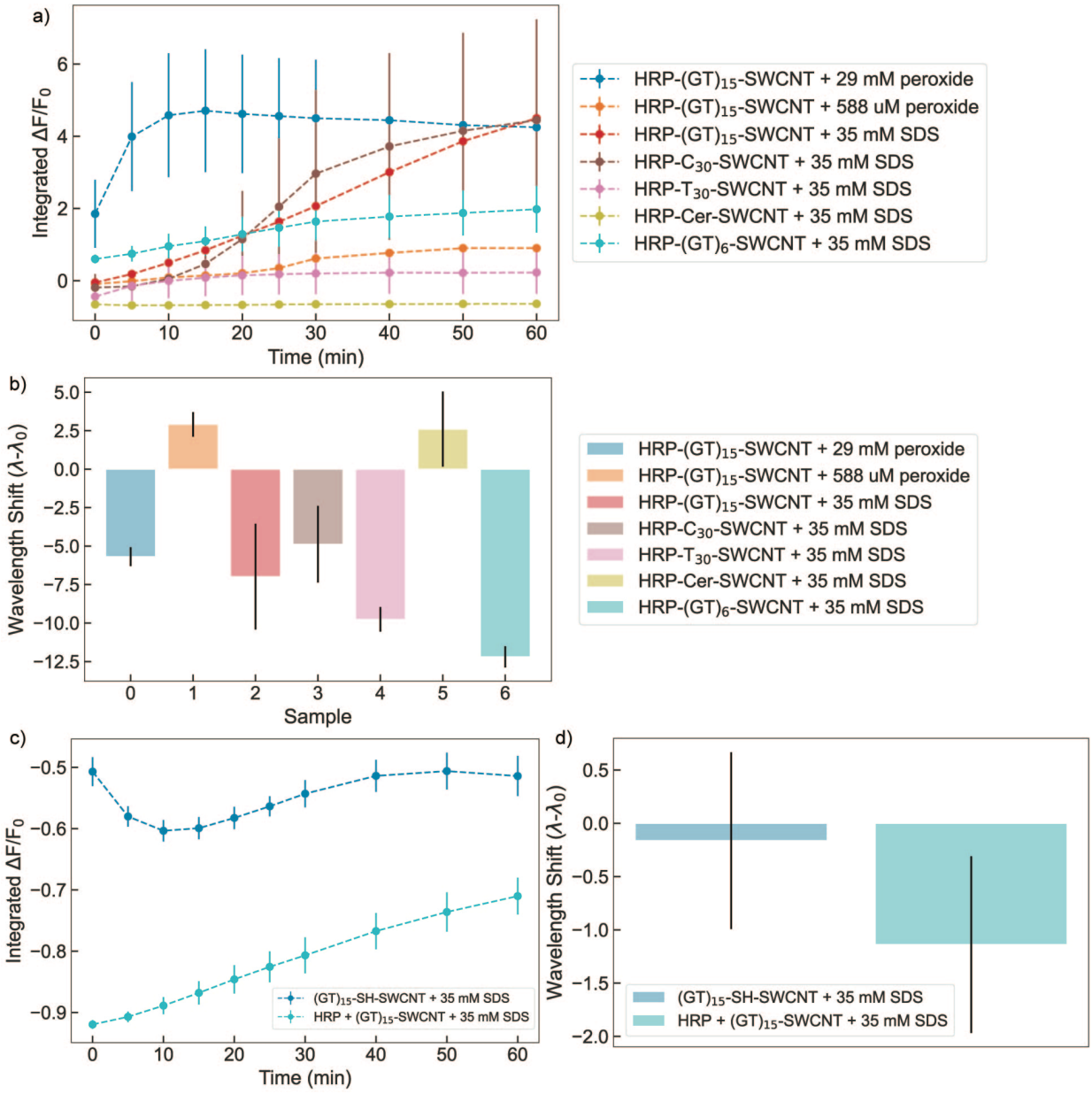

Figure 4.12. HRP-SWCNT nanosensor responses to denaturant SDS. (a) Comparing the response of various HRP-SWCNT constructs to excess SDS, a known protein denaturant, to that of high and low levels of H_2O_2, the response profiles appear similar in magnitude but vary in kinetics. The addition of 29.4 mM H_2O_2 to the HRP-$(GT)_{15}$-SWCNT nanosensor induces a fast turn-on to peak fluorescence, whereas the addition of 35 mM SDS to the same construct shows a linear increase in fluorescence over 60 minutes. HRP-C_{30}-SWCNT and HRP-$(GT)_6$-SWCNT also exhibit turn-on responses to 35 mM SDS, with HRP-C_{30}-SWCNT mirroring the response of HRP-$(GT)_{15}$-SWCNT in linearity and HRP-$(GT)_6$-SWCNT showing a lower magnitude turn-on response in comparison. Notably, these three constructs were also the only ones to exhibit a turn-on response to H_2O_2, while HRP-Cer-SWCNT and HRP-T_{30}-SWCNT again showed no response. (b) Monitoring the endpoint solvatochromic shifts of the (9,4) SWCNT chirality fluorescence intensity peak wavelength for the conditions in (a) identifies a significant blue-shift for almost all conditions involving SDS, as expected with surfactant addition to SWCNTs.

Though the HRP-$(GT)_{15}$-SWCNT nanosensor exhibits a blue-shift induced by H_2O_2 addition similar to the behavior in response to SDS, the difference in kinetics of these responses suggests different mechanisms of action. Additionally, HRP-T_{30}-SWCNT shows a strong blue-shift upon SDS addition but again shows no fluorescence intensity modulation, clouding the role of SDS in the observed blue-shifts and fluorescence increases. (c),(d) Addition of 35 mM SDS to $(GT)_{15}$-SH-SWCNTs alone and when incubated with HRP prior to addition both exhibit strong turn-off responses and no or mild blue-shifting, respectively. These results indicate that SDS interaction with the SWCNTs directly are not the source of fluorescence modulation seen in (a). Error bars represent the standard deviation between experimental replicates (n = 3).

Assessing the solvatochromic shift of the nanosensors in response to 35 mM SDS reveals a consistent blue-shift for all constructs except HRP-Cer-SWCNTs (Figure 4.12b). Interestingly, the solvatochromic shift of HRP-$(GT)_{15}$-SWCNT nanosensors differs depending on the amount of H_2O_2 added, lending more support to Mechanism (i) where varying levels of H_2O_2 added induce different redox states at the heme center of HRP, affecting the local SWCNT dielectric environment and in turn increasing fluorescence. It is important to note that again, HRP-T_{30}-SWCNTs show no response to SDS in fluorescence intensity but do exhibit a strong blue solvatochromic shift, clouding the role of SDS in modulating SWCNT fluorescence and local environment. The addition of SDS to $(GT)_{15}$-SH-SWCNTs alone and when mixed non-covalently both show a strong turn-off response (Figure 4.12c) and slight blue-shifting (Figure 4.12d) in accordance with previous literature.[77] These results suggest that the observed response of the nanosensor to SDS cannot be attributed to SDS interacting with the SWCNT itself. Previous studies have investigated the binding and kinetics of HRP denaturation by SDS and found that at an SDS concentration of 0.60 mM, 21 moles of SDS bind to one mole of HRP.[102,115] It is thus conceivable that the observed nanosensor response to SDS can be attributed to the slow and constant binding of SDS to HRP on SWCNTs, unfolding HRP by denaturation and thereby inhibiting its ability to quench SWCNT fluorescence. However, the apparent kinetic profile of the SDS response being linear suggests that this mechanism holds true specifically for exceedingly large amounts of surfactant interacting with proteins on SWCNT rather than the general mechanism for this specific enzyme-SWCNT nanosensor.

4.5.4 Proposed Nanosensor Mechanism

Based on our data, we hypothesize that the leading mechanism for nanosensor function is Mechanism (i) whereby H_2O_2 modulates native HRP into different redox states that influence SWCNT fluorescence emission, namely Compound II and the Compound III inactive intermediate as has been demonstrated when H_2O_2 is the only substrate present in the reaction.[101,108,109] At high concentrations of H_2O_2, this reaction is fast and the redox active heme center of Compound III would facilitate a very strong turn-on fluorescence response accompanied by a blue-shifted fluorescence spectra by about 5 nm. At low concentrations of H_2O_2, below the threshold required to induce Compound III formation, HRP primarily avoids Compound III formation and undergoes its regular catalytic cycle to consume added H_2O_2, cycling from native HRP to Compound I to mostly Compound II at any given time as found in previous studies.[101] With Compound II being the oxidized form of native HRP, it is possible that this redox state also enhances SWCNT fluorescence to a lesser degree than Compound III, explaining the lesser magnitude response and simultaneous red-shift in the fluorescence spectra. Since Compound II can be reduced to

Compound III upon subsequent H_2O_2 addition while Compound III cannot consume H_2O_2 as it is catalytically inactive, this mechanism is compatible with our findings that the nanosensor can still increase in fluorescence after incubation with a low amount of H_2O_2 yet fails to do so after incubation with a high amount of H_2O_2.

4.6 Conclusions

Altogether, these results demonstrate successful nanosensor generation via covalent HRP-SWCNT conjugation. The nanosensor responds to H_2O_2 with a stable and concentration-dependent turn-on in fluorescence compared to baseline. Fitting the concentration-dependent response to a cooperative-binding model yields parameters such as a limit of detection of 31 μM H_2O_2 and an expected cooperativity coefficient of ~1, confirming the reliance of HRP-H_2O_2 binding for the fluorescence turn-on response. A mock nanosensor, synthesized by the same process as the nanosensor but without Sulfo-SMCC crosslinker, showed low HRP activity and no turn-on fluorescence response, confirming the necessity of covalent HRP attachment for the observed performance. Furthermore, the nanosensor can be immobilized on glass and image H_2O_2 in real-time, showing consistent and repeatable fluorescence increases in response to H_2O_2.

Experiments to elucidate a mechanism were conducted, testing the nanosensor's response to H_2O_2 in various conditions including different pH and ionic strength buffers, excess Catalase or HRP, and inhibitory GSH. In these conditions, the nanosensor performed as expected, showing the highest response in the conditions that best promote HRP enzymatic activity (high pH and high ionic strength), and minimal or no activity in conditions that mitigate enzymatic activity such as low pH and ionic strength and in the presence of GSH, a known HRP inhibitor. When compared with the control condition of HRP noncovalently mixed with SWCNTs, which showed no turn-on response in all conditions, these results isolate the mechanism of the nanosensor to the enzymatic function of HRP covalently bound on the SWCNT surface.

Further experiments uncovered the most likely mechanism for this nanosensor as the redox state of the heme center of HRP affecting SWCNT fluorescence. The nanosensor responds differently to varied concentrations of H_2O_2 in magnitude, kinetics, and when pre-incubated with different concentrations of H_2O_2, indicating a dependence on HRP redox state for fluorescence modulation. However, the observed turn-on response is not replicated in the presence of salicylic acid, a molecule known to induce HRP to an inactive form (P-670). Thus, the most likely redox states that induce fluorescence modulation are Compound II and Compound III, in which the heme center of HRP is charged or features a charged radical, respectively. These heme redox states could thus be influencing SWCNT exciton recombination energy and thus modulating fluorescence intensity as observed.

Other mechanisms were proposed and eliminated by experiments including synthesizing the nanosensor with a variety of dispersant molecules including ssDNA of the same length as $(GT)_{15}$, the amphiphilic lipid group Ceramide, and a shorter ssDNA sequence $(GT)_6$. These different nanosensors showed no clear trend in response to H_2O_2, eliminating a reliance on a specific DNA sequence for the mechanism. Further, a surfactant SDS was added to these nanosensors to determine if HRP denaturation was the mechanistic source of fluorescence modulation, but the

response profile and solvatochromic shift observed with this analyte differed greatly from the response to H_2O_2, eliminating HRP denaturation as the mechanism.

Overall, we demonstrated the utility of this platform for robust nanosensor generation and outlined a workflow to synthesize, characterize, and apply these covalent protein-SWCNT conjugates.

4.7 Materials and Methods

Materials: All chemicals unless otherwise stated were purchased from Sigma-Aldrich. Raw high pressure carbon monoxide (HiPco) synthesized SWCNTs were purchased from NanoIntegris (SKU# 1601). C_{16}-PEG2k-Ceramide (N-palmitoyl-sphingosine-1-{succinyl[methoxy(polyethyleneglycol)2000]}) phospholipid was purchased from Avanti Polar Lipids (SKU# 880180P). $(GT)_{15}$ ssDNA was purchased from Integrated DNA Technologies. Sulfo-SMCC (sulfosuccinimidyl 4-(N-maleimidomethyl)cyclohexane-1-carboxylate) was purchased from ThermoFisher Scientific (Catalog# A39268). Luminol (Pierce ECL Western Blotting Substrate) was purchased from ThermoFisher Scientific (Catalog# 32209). Glass-bottom microwell dishes (35 mm petri dish with 10 mm microwell) were purchased from MatTek (Catalog# NC9341562). Hydrogen Peroxide (3% w/w) was purchased from Labchem (Catalog# LC154501). Sodium hypochlorite was purchased from Avantor Performance Materials (Catalog# 9416-01). Tert-butyl hydroperoxide (TBHP) was purchased from EMD Millipore (Catalog# 8.14006.0250). Xanthine was purchased from Sigma-Aldrich (Catalog# X7375-25G). Xanthine Oxidase (from buttermilk) was purchased from Millipore Sigma (Catalog# 682151-10U). 2-(2-methoxy-4-nitrophenyl)-3-(4-nitrophenyl)-5-(2,4-disulfophenyl)-2H-tetrazolium (WST-8) was purchased from MedChemExpress (Catalog# HY-D0831-25MG).

Near-Infrared Spectroscopy of SWCNT Nanosensors: Fluorescence spectra were obtained with an in-house nIR microscope setup. Briefly, we used an inverted Zeiss microscope (Axio Observer.D1, 10X objective) coupled to a Princeton Instruments spectrometer (SCT 320) and liquid nitrogen-cooled Princeton Instruments InGaAs detector (PyLoN-IR). SWCNT samples were excited with a 721 nm laser (OptoEngine LLC) and emission was collected in the 850 – 1350 nm wavelength range. The samples were measured in a 384 well-plate (Greiner Bio-One microplate) with a total volume of 30 μL per well. For solution-phase sensor response screens, nanosensor at 2.5 mg L^{-1} [SWCNT] in 1X PBS (27 μL) was added per well and 10X H_2O_2 (3 μL) was injected per well with a microchannel pipette in triplicate. After analyte addition, each well was briefly mixed by pipetting, sealed with an adhesive seal (Bio-Rad) and spun down for 10 s with a benchtop well plate centrifuge to remove bubbles. Fluorescence spectra were measured at time points of 0 min after analyte addition, 5 min, 10 min, 15 min, 20 min, and every 10 min after until 1 h post-addition.

Near-Infrared Microscopy of SWCNT Nanosensors: Fluorescence images were captured with the same epifluorescence microscope setup as described previously with a 100X oil immersion objective and a Ninox VIS-SWIR 640 camera (Raptor). Nanosensors were immobilized on glass-bottom microwell dishes (35 mm petri dish with 10 mm microwell, MatTek) as follows: each dish was washed twice with PBS (150 μL), incubated with nanosensor at 2.5 mg L^{-1} (100 μL) for 20 min, and washed twice again with PBS (150 μL). For each image, PBS (160 μL) was added to the dish and the z-plane was refocused to maximize SWCNT fluorescence intensity. Images were then recorded over 5 min with an exposure time of 950 ms and 1000 ms repeat cycle. Water (20 μL)

was added at Frame 60 and analyte (20 μL) was added at Frame 120. Images were processed with ImageJ as follows: a median filter (0.5-pixel radius) and rolling ball background subtraction (300-pixel radius) were applied, the image was cropped to eliminate gaussian blur and highlight the center of the image with the brightest nanosensors (width = 375, height = 375, x-coordinate = 110, y-coordinate = 36), the image was then analyzed using the ROI analyzer tool (Multi Measure) highlighting the clearest 20 ROIs of nanosensor bundles.

Superoxide Generation: Superoxide was generated enzymatically with the Xanthine/Xanthine Oxidase system according to previously established protocols.[97] Briefly, Xanthine was dissolved at 10 mM in 0.1 M NaOH and the pH was adjusted to 7 with 0.1 M HCl and a pH probe. Xanthine Oxidase was diluted to 0.1 U mL^{-1} in 1X PBS. Xanthine and Xanthine Oxidase (50 μL each) were added to 1X PBS (140 μL) in an Eppendorf tube and incubated 2 h at 25 °C. Separately, the generation of superoxide was validated by incubating 20 mg mL^{-1} WST-8 with the reaction mixture. The absorbance at 460 nm of the resulting solution was measured to determine the presence of the WST-8 formazan product, which is proportional to the generation of superoxide. Using the Beer-Lambert law with extinction coefficient ε_{460} = 30,700 M^{-1} cm^{-1} for the formazan product and knowing 2 superoxide radicals are required to generate 1 formazan, we calculated the superoxide concentration in this system (Figure 4.11).[113]

SDS-PAGE of Nanosensors and Filtration Flowthroughs: SDS-PAGE was performed according to previously established protocols. Briefly, sample buffer was prepared by combining glycerol (2.5 mL), water (3.75 mL), 0.5 M Tris-HCl buffer pH 6.8 (1.25 mL), and 10% w/v SDS (2 mL). Gel running buffer was prepared with 10X Tris/Glycine/SDS Buffer (50 mL, Bio-Rad) and deionized water (450 mL). Sample (5 μL) was added to sample buffer (7.5 μL) and 6X loading dye (2.5 μL, New England Biosciences) and boiled at 95 °C for 5 min. Samples were then loaded onto a 4-20% Mini-PROTEAN® TGX™ Precast Protein Gel (Bio-Rad) in a Mini-PROTEAN® Tetra Vertical Electrophorseis Cell (Bio-Rad) with running buffer according to manufacturer's instructions. Gel electrophoresis was run with a Mini-PROTEAN® PowerPac Basic Power Supply (Bio-Rad) at 200 V for 30 min. The finished gel was then stained with Coomassie Brilliant Blue (Thermo Scientific) for 1 hour, shaking gently. The gel was then de-stained overnight with 50% water, 40% methanol, 10% acetic acid (v/v/v) solution. The final gel was rehydrated in water and imaged according to manufacturer's instructions on a Typhoon FLA 9500 laser scanner (Cytiva) in digitization mode with a 532 nm excitation laser and a long-pass green filter. Gel images were processed with imageJ to adjust color contrast and image field of view.

Chapter 5: Extending Conjugation Platform to Other Systems

5.1 Chapter Abstract

The robust covalent protein-SWCNT conjugation platform developed with HRP serves as a foundation for the extension of the platform toward other proteins of interest. Herein, we present our efforts to extend our platform towards Concanavalin A, Lysozyme, Wheat Germ Agglutinin, and CRISPR-Cas9 ribonucleoprotein. All proteins represent potential candidates for recognition elements as nanosensors or cargo for delivery to plant and animal cells. We demonstrate that, of these options, Cas9 exhibits the least nonspecific adsorption to SWCNTs, highlighting it as the best candidate for platform extension. We optimized the platform for the specific properties of Cas9, changing reaction buffer, time, and temperature to best preserve protein stability. To confirm maintained Cas9 enzymatic activity after conjugation, we performed an *in vitro* DNA cleavage assay and demonstrate a dependence on SMCC:Cas9 molar ratio. These preliminary results motivate further investigation and optimization of covalent Cas9-SWCNTs for plant gene editing and DNA sensing applications.

5.2 Assessing Other Enzymes for Nanosensor Development

With the platform developed using HRP as a model protein as in Chapters 2-4, we now apply this methodology to other proteins of interest for nanosensor generation. Candidate proteins should achieve all figures of merit mentioned previously including binding capacity for an analyte of biological relevance, low molecular weight for ease of separation, amenability for Sulfo-SMCC crosslinking, and minimal nonspecific adsorption to SWCNTs. Candidate proteins that bind analytes of interest include Concanavalin A, Lysozyme, Wheat Germ Agglutinin, and CRISPR-Cas9 ribonucleoprotein.

5.2.1 Concanavalin A

Concanavalin A (ConA) is a sugar-binding protein isolated from the jack bean plant that exists as a tetramer at pH 7 with a molecular weight of 104 kDa.[116] ConA has been harnessed for a variety of biological applications in recent years including glucose sensing for disease diagnostics and insulin delivery, leveraging its natural affinity for sugars such as glucose and mannose.[117–119] Thus, ConA could potentially be conjugated to SWCNTs with our platform for selective glucose sensing. ConA features 12 exposed lysines, which researchers have previously used to attach around 8 polyethylene glycol (PEG) chains to ConA for improved stability.[120] These lysines thus make ConA amenable to Sulfo-SMCC functionalization, though the exact reaction conditions require optimization to avoid over-functionalization and subsequent loss of binding activity. Since ConA meets almost all characteristics for nanosensor development as mentioned above, we assessed the degree of nonspecific ConA adsorption to $(GT)_{15}$, Ceramide, and SC-dispersed SH-SWCNTs (Figure 5.1).

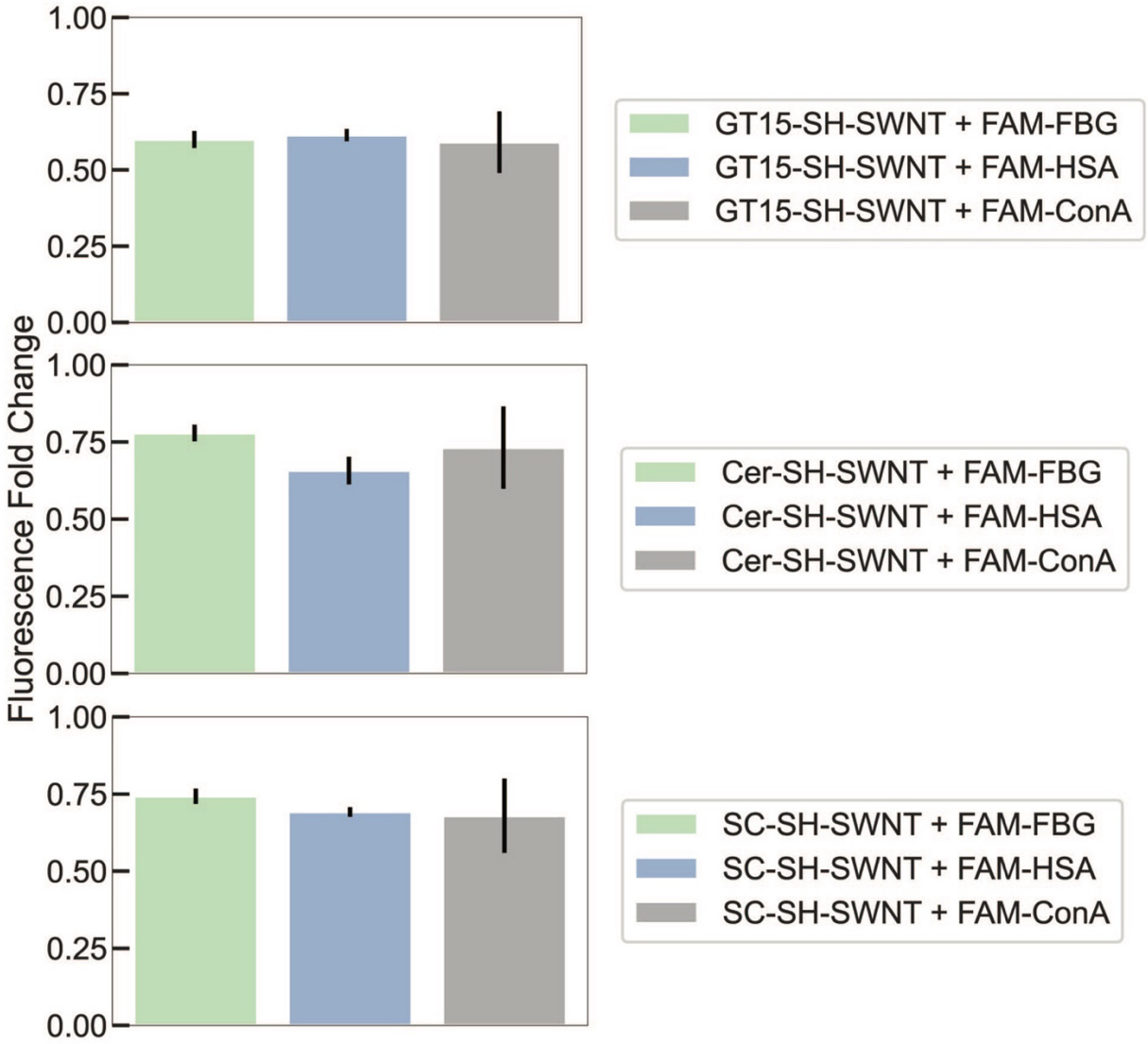

Figure 5.1. Corona exchange dynamics characterization of ConA with dispersed SH-SWCNTs. Corona exchange assay for ConA and control proteins shows similar adsorption to different dispersant-SH-SWCNT samples. Fold change was calculated as the endpoint FAM fluorescence value 60 min after SWCNT addition to FAM-proteins divided by the initial FAM fluorescence for each protein sample. Error bars represent the standard deviation of experimental replicates (n = 3).

Unfortunately, ConA shows similar adsorption to all SWCNT samples relative to the control proteins Fibrinogen (FBG) and Human Serum Albumin (HSA). Thus, downstream sensor screen results would not be attributable to covalently-bound ConA as there would be a mixed population of covalent and noncovalent ConA on the SWCNT surface. The SWCNT adsorption observed in these three cases may not hold true for SWCNTs dispersed with other easily available polymers including other ssDNA sequences like $(GT)_6$ and C_{30}, other surfactants like SDS, or other amphiphilic lipids like DPPE-PEG(5000). Though these conditions were left untested, future studies aiming to develop ConA-SWCNTs could easily undergo optimization to find the dispersant

that best mitigates noncovalent ConA adsorption by the corona exchange dynamics assay and follow our conjugation platform accordingly.

5.2.2 Lysozyme

Lysozyme is a small (14.3 kDa) antimicrobial enzyme produced by the innate immune system in animals that hydrolyzes glycosidic bonds in the peptidoglycan layer of bacterial cell walls.[121] This antimicrobial property has motivated coupling of Lysozyme with nanoparticles made of chitosan for mitigation of harmful bacteria in the food industry and delivery of Lysozyme with chitosan-alginate hydrogels for the same purpose.[122,123] Lysozyme could thus be conjugated to SWCNTs with this sample for bacterial contamination sensing in food and beverage samples. Lysozyme contains 6 lysine residues, 5 of which are solvent-accessible, making it amenable to Sulfo-SMCC conjugation with some optimization of reaction conditions.[121] Again, Lysozyme shows potential as a good candidate for nanosensor generation with our platform provided it exhibits minimal noncovalent adsorption to dispersed SH-SWCNTs. We again leveraged the corona exchange dynamics assay to assess Lysozyme's potential for conjugation with this platform to $(GT)_{15}$, Ceramide, and SC-dispersed SH-SWCNTs (Figure 5.2).

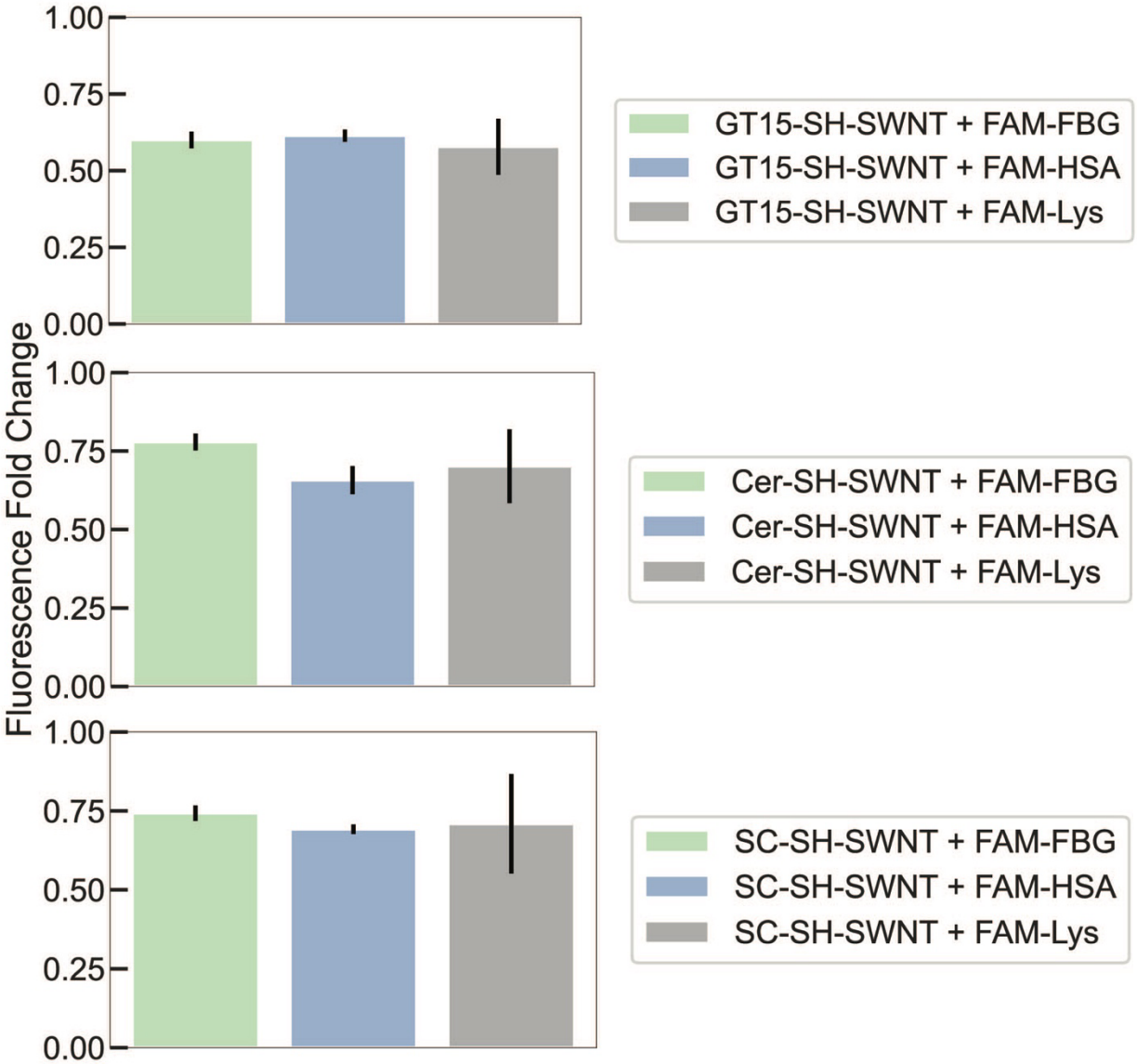

Figure 5.2. Corona exchange dynamics characterization of Lysozyme with dispersed SH-SWCNTs. Corona exchange assay for Lysozyme and control proteins shows similar adsorption to different dispersant-SH-SWCNT samples. Fold change was calculated as the endpoint FAM fluorescence value 60 min after SWCNT addition to FAM-proteins divided by the initial FAM fluorescence for each protein sample. Error bars represent the standard deviation of experimental replicates (n = 3).

As with ConA, Lysozyme shows similar noncovalent adsorption as control proteins FBG and HSA to all SWCNTs tested. As such, Lysozyme was not selected for conjugate development with the platform presented in this dissertation. Again, researchers interested in pursuing Lysozyme conjugation to SWCNTs with this platform should explore other SWCNT dispersants and assess noncovalent adsorption with this assay. Given Lysozyme's small molecular weight, purification via spin-filtration should be easier than other larger proteins. Therefore, if a SWCNT dispersant that minimizes Lysozyme adsorption is found, researchers that leverage our platform can be

confident that any unconjugated protein would be separated and that protein present in the final product is covalently bound.

5.2.3 Wheat Germ Agglutinin

Wheat Germ Agglutinin (WGA) is a 36 kDa lectin (carbohydrate-binding protein) found in wheat that protects the plant from hostile species like insects, yeast, and bacteria.[124] WGA primarily binds *N*-acetylglutaminic acid (GlcNAc) and *N*-acetylneuraminic acid (Neu5Ac) and has been demonstrated as a potential therapeutic agent for cancer, showing toxicity against acute myeloid leukemia cells in mice.[125] Additionally, a sugar sensor leveraging WGA and SWCNT has been developed in recent years, though the method for attaching WGA to SWCNT relied on binding to peptoid loops noncovalently adsorbed to SWCNT.[52] Thus, covalent attachment of WGA to SWCNT could aid in delivery for cancer treatment and stable sensors for sugar molecules.[126] WGA has 8 lysine groups in its structure, 4 of which are solvent-accessible and thus amenable to Sulfo-SMCC functionalization.[127] As such, WGA presents as a viable candidate for covalent conjugation to SWCNT with our platform provided that it shows minimal adsorption to dispersed SH-SWCNT (Figure 5.3).

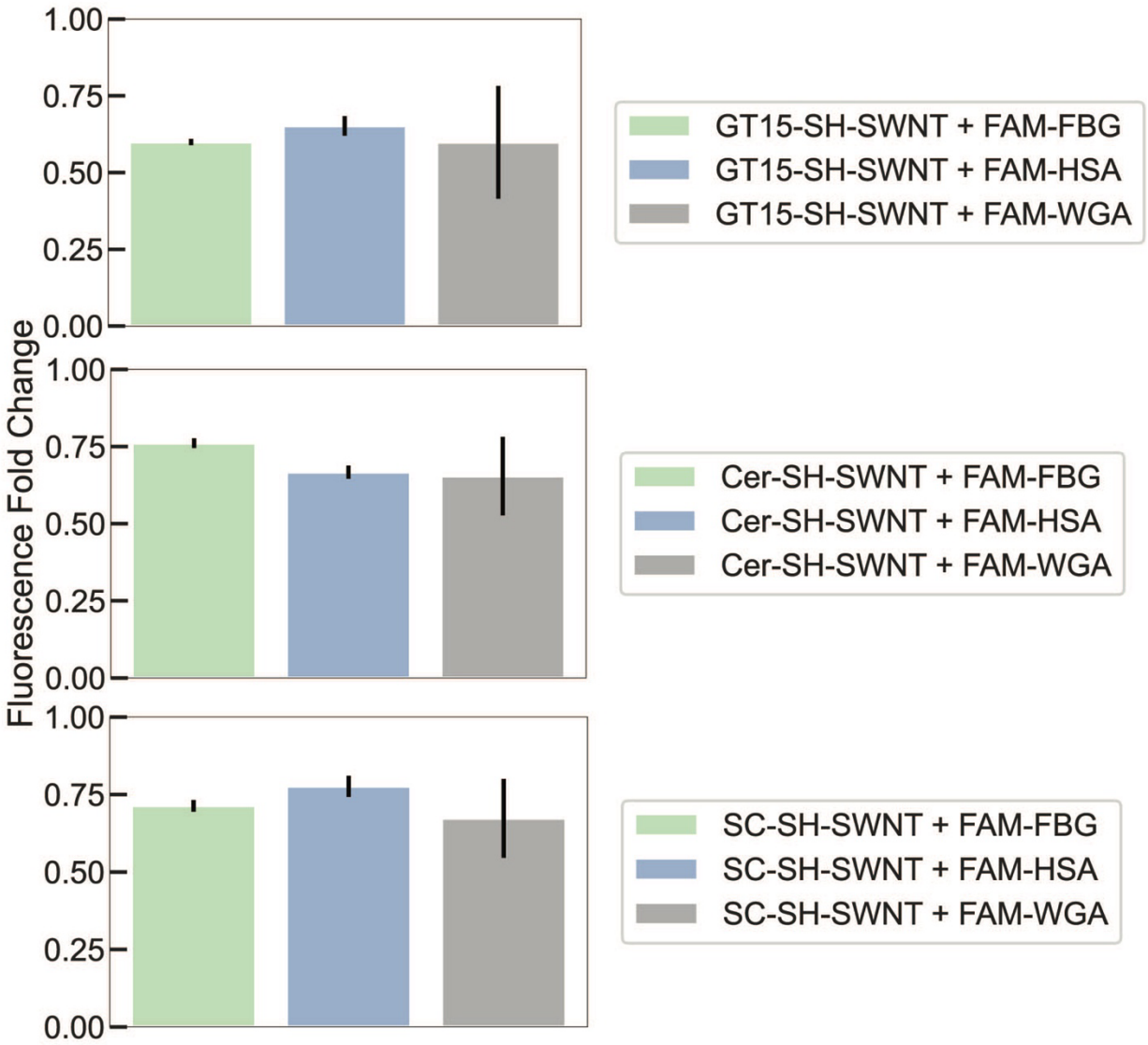

Figure 5.3. Corona exchange dynamics characterization of WGA with dispersed SH-SWCNTs. Corona exchange assay for WGA and control proteins shows similar adsorption to different dispersant-SH-SWCNT samples. Fold change was calculated as the endpoint FAM fluorescence value 60 min after SWCNT addition to FAM-proteins divided by the initial FAM fluorescence for each protein sample. Error bars represent the standard deviation of experimental replicates (n = 3).

As with ConA and Lysozyme, WGA fails to pass the final metric for platform optimization as it shows similar levels of nonspecific adsorption to all SWCNTs tested. These results help validate the use of HRP as a good model protein for development of our platform, as it has so far shown the least adsorption to SWCNTs. Again, it is possible that future optimization to minimize WGA adsorption could be achieved with other SWCNT dispersants and advance WGA-SWCNT generation via this platform. However, these routes were left unexplored and we encourage future researchers to perform more extensive design space exploration to successfully generate covalent WGA-SWCNT conjugates for enhanced cancer therapy and sugar sensing.

5.2.4 CRISPR-Cas9

With the previous proteins all showing prohibitive levels of noncovalent adsorption to SWCNTs, we expanded our candidate protein library to a larger protein in CRISPR-Cas9 (Cas9). Cas9 is an endonuclease protein that selectively cleaves DNA for targeted gene editing, winning the Nobel Prize in Chemistry in 2020. For gene editing applications, the Cas9 protein must be complexed with a guide RNA (gRNA) that binds and interacts with DNA, targeting a specific sequence for cleavage by the enzyme. This complex is referred to as the Cas9 ribonucleoprotein (RNP) and it has an overall molecular weight around 165 kDa.[128] This large size makes RNP delivery to cells difficult since the large and complex structure limits delivery efficiency alone without nanoparticle carriers.[129] Thus, it would be advantageous to pursue covalent attachment of RNP to nanoparticles for enhanced delivery to plant and mammalian cells for targeted gene editing.

In recent years, researchers have heavily pursued advancements in this area, showing enhanced RNP delivery with several nanoparticle systems including gold, lipids, DNA, and chitosan, among others.[130,131] However, RNP delivery with SWCNT has yet to be explored to our knowledge, which could prove advantageous especially for plant gene editing given SWCNT's demonstrated ability to deliver DNA and RNA cargo to plant cells. Though larger in molecular weight than HRP, free RNP can still be separated from SWCNTs with large 300K molecular weight cutoff (MWCO) spin filters. Furthermore, Cas9 features 43 lysine amino acids in its sequence, though several of them experience significant conformational changes as the RNP enzymatically cleaves DNA, so careful optimization of the SMCC reaction must be performed to ensure these lysines remain unmodified.[132] As such, we used the corona exchange dynamics assay to begin Cas9-SWCNT development by assessing noncovalent adsorption of Cas9 to SWCNTs dispersed with $(GT)_{15}$, $(GT)_6$, and Ceramide (Figure 5.4).

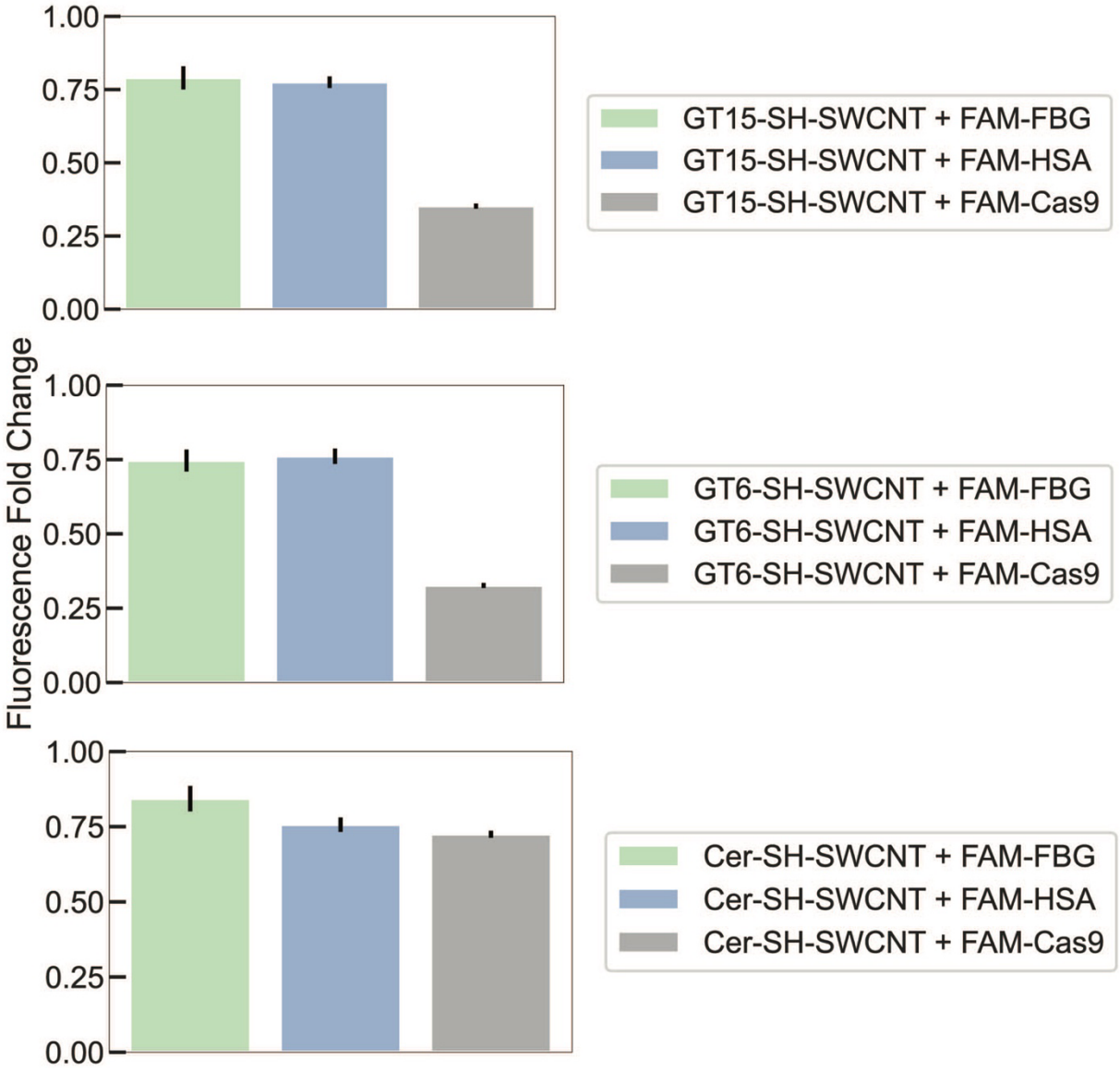

Figure 5.4. Corona exchange dynamics characterization of Cas9 with dispersed SH-SWCNTs. Corona exchange assay shows Cas9 exhibiting strong adsorption to the ssDNA-SH-SWCNT samples relative to control proteins. For Ceramide-SH-SWCNTs, Cas9 shows similar adsorption levels as control proteins. Fold change was calculated as the endpoint FAM fluorescence value 60 min after SWCNT addition to FAM-proteins divided by the initial FAM fluorescence for each protein sample. Error bars represent the standard deviation of experimental replicates (n = 3).

Notably, Cas9 shows very strong adsorption to SWCNTs dispersed with ssDNA compared to control proteins. By contrast, Cas9 shows comparable levels of nonspecific adsorption to Ceramide-SH-SWCNTs as the control proteins, identifying these SWCNTs as the best condition to move forward with through the conjugation platform. As an aside, SC-SH-SWCNTs were avoided for this study out of concerns for the stability of Cas9 in the presence of surfactant.

Out of all the enzymes tested so far, Cas9 represents the best candidate for extension of the platform presented in this dissertation. As such, we proceeded with development of Cas9-SWCNTs for both enhanced delivery for gene editing and potentially as a targeted DNA sensor.

5.3 CRISPR-Cas9 SWCNT Conjugation for Gene Editing

Following successful identification of Ceramide-SH-SWCNTs as best mitigating nonspecific Cas9 adsorption, we modified and optimized our conjugation platform according to the principles detailed in Chapters 2-4 (Figure 5.5).

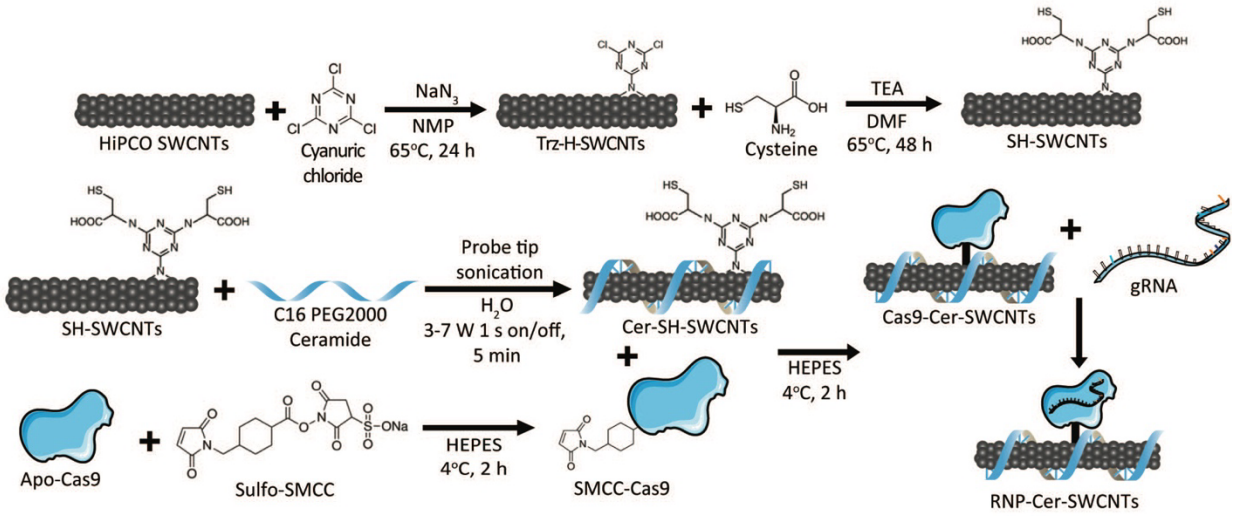

Figure 5.5. Reaction scheme for covalent Cas9-SWCNTs. SH-SWCNTs were probe-tip sonicated with Ceramide to disperse them in solution. Cas9 was then functionalized with Sulfo-SMCC crosslinker for 2 hr at 4 °C in HEPES buffer. Maleimide-functionalized Cas9 was then conjugated to Cer-SH-SWCNTs over 2 hr at 4 °C in HEPES buffer, spin-filtered to remove free unconjugated Cas9, and complexed with guide RNA to form RNP-Cer-SWCNTs.

Specifically, we used probe-tip sonication to disperse SH-SWCNTs with C16-PEG(2000)-Ceramide. An amphiphilic polymer, Ceramide is a PEGylated lipid whose hydrophobic lipid tail binds to the SWCNT surface and hydrophilic PEG chains interface with the aqueous environment to disperse SWCNT in solution. As such, we adjusted probe-tip sonication time from 15 min as used with $(GT)_{15}$ ssDNA to 5 min. For Cas9 functionalization with Sulfo-SMCC, we conducted the reaction in HEPES buffer instead of PBS for greater protein stability as Cas9 exhibited poor stability in PBS buffer. Additionally, the reaction temperature was decreased to 4 °C from 25 °C for increased Cas9 stability. The reaction time was extended to 2 hr from 1 hr accordingly to account for slower reaction kinetics at a lower temperature. The SWCNT-Cas9 conjugation reaction was also performed at these same time and temperature conditions. We experimented with performing the conjugation with Cas9 without gRNA (Apo-Cas9) and with gRNA (RNP) but observed poor conjugation efficiency and final product stability in the latter condition. Therefore, we opted to conjugate Apo-Cas9 to SWCNT first and complex gRNA to the final product.

To confirm that Cas9 conjugated to SWCNT maintains enzymatic activity, we conducted an *in vitro* DNA cleavage assay (Figure 5.6a).

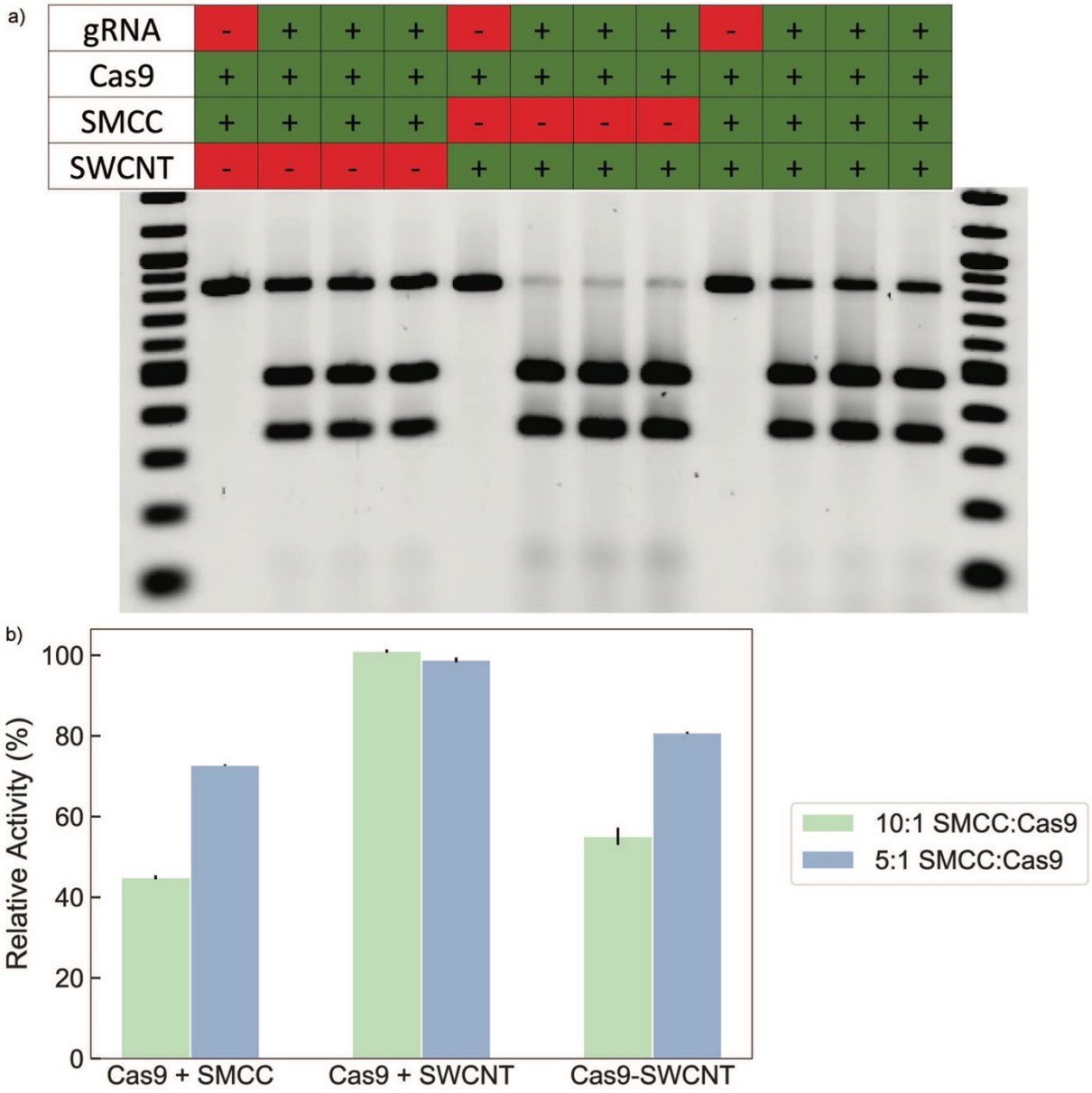

Figure 5.6. *In vitro* cleavage assay for Cas9 enzymatic activity. (a) DNA agarose gel of Cas9 functionalized with SMCC at a 10:1 ratio, mixed with SWCNT, and covalently conjugated to SWCNT shows varying maintenance of Cas9 activity as seen by the relative intensities of uncleaved (upper) and cleaved (lower) DNA bands. (b) Calculating relative activity of Cas9 conditions shown in (a) at two different SMCC:Cas9 ratios reveals better Cas9 activity for the lower SMCC:Cas9 ratio. Error bars represent the standard deviation of experimental replicates (n = 3).

In this assay, a target DNA sequence was incubated with Apo-Cas9-SWCNTs and RNP-SWCNTs for 16 hr at 37 ºC, the optimal temperature for Cas9 activity. The sample was then heated to 80 ºC for 10 min to de-couple DNA from Cas9 and held at 4 ºC before loading onto an agarose gel. For samples without gRNA, the target DNA should appear as a single band on the gel as Cas9 cannot

cleave DNA without gRNA complexed. For samples with gRNA, the cleaved DNA should appear as two separate bands since the cleavage site on the DNA is slightly offset from the middle of the sequence, creating two DNA fragments with different molecular weights. By comparing the band intensities of cleaved and uncleaved DNA, we can calculate the relative activity of Cas9 when conjugated to SWCNTs with the following equation:

$$Relative\ Activity = \frac{Intensity\ of\ Cleaved\ DNA\ Bands\ in\ Lane}{Total\ Intensity\ of\ Bands\ in\ Lane} \times 100\%$$

As seen by the gel results, no Cas9 activity is observed for all conditions without gRNA complexation as expected. SMCC functionalization at a 10:1 molar ratio appears to hinder Cas9 activity slightly compared to unmodified Cas9 in the presence of Cer-SH-SWCNT as seen by the stronger intensity of uncleaved DNA bands. However, cleaved DNA bands still appear in the former condition, indicating some level of Cas9 enzymatic activity is still available when functionalized with SMCC. Similarly, covalently-conjugated Cas9 successfully exhibits DNA cleavage, albeit to a lesser degree than unfunctionalized Cas9 in the presence of SWCNT.

Calculating the cleavage activity for the aforementioned conditions at two different SMCC:Cas9 ratios, we observe increased activity at 5:1 SMCC:Cas9 compared to 10:1 as optimized in the original platform and no difference when Cas9 is unfunctionalized and in the presence of SWCNT (Figure 5.6b). We hypothesize that the 10:1 SMCC:Cas9 condition could result in greater SMCC functionalization of lysine residues critical to the large conformational shift that Cas9 undergoes when binding and cleaving target DNA, sterically hindering activity. At a ratio of 5:1 SMCC:Cas9, fewer crosslinkers would be added per Cas9, avoiding this steric hindrance and better maintaining enzymatic activity as a result. As per our platform, QTOF-MS could be used to confirm this hypothesis and help optimize a SMCC:Cas9 ratio that maximizes both enzymatic activity and conjugation to SWCNT. Potential ratios to examine could reach 1:1 SMCC:Cas9 or even have more protein than SMCC to best ensure singular SMCC functionalization of only the most accessible lysine residues. This optimization should be conducted before proceeding with plant gene editing experiments for maximum resource and labor efficiency.

5.4 Conclusions

Overall, these results demonstrate the possibility of extending our conjugation platform to other proteins of interest. ConA, Lysozyme, and WGA all exhibited high levels of nonspecific adsorption to all SWCNTs tested, highlighting the utility of HRP as a model protein for the original platform optimization and precluding them from nanosensor generation with the group of SWCNT dispersants assessed. Cas9 showed high adsorption to ssDNA-SWCNTs but minimal adsorption to Ceramide-SWCNTs, motivating further investigation for Cas9 delivery via Cer-SWCNT conjugation.

As mentioned previously, the platform conditions for HRP require optimization for each new protein of interest depending on the protein's properties. Accordingly, we adjusted the buffer, time, and temperature of the SMCC functionalization reaction to best preserve Cas9 stability. With these optimized conditions, we conducted *in vitro* DNA cleavage assays to confirm maintained but attenuated Cas9 enzymatic activity when conjugated to SWCNTs. These experiments elucidated a

trend of lower SMCC:Cas9 molar ratio leading to higher enzymatic activity, potentially attributable to steric hindrance imparted by SMCC at a 10:1 ratio. Future experiments in this area should be conducted to further optimize this ratio to best maintain Cas9 activity and can be confirmed with QTOF-MS coupled with the *in vitro* cleavage assay as shown here. With this platform, we anticipate that the development of covalent Cas9-SWCNT conjugates can be accelerated towards efficient targeted gene editing and DNA sensing applications.

5.5 Materials and Methods

Materials: All chemicals unless otherwise stated were purchased from Sigma-Aldrich. Raw high pressure carbon monoxide (HiPco) synthesized SWCNTs were purchased from NanoIntegris (SKU# 1601). C_{16}-PEG2k-Ceramide (N-palmitoyl-sphingosine-1-{succinyl[methoxy(polyethyleneglycol)2000]}) phospholipid was purchased from Avanti Polar Lipids (SKU# 880180P). $(GT)_{15}$ ssDNA was purchased from Integrated DNA Technologies. $(GT)_6$ ssDNA was purchased from Integrated DNA Technologies. Sulfo-SMCC (sulfosuccinimidyl 4-(N-maleimidomethyl)cyclohexane-1-carboxylate) was purchased from ThermoFisher Scientific (Catalog# A39268).

Noncovalent Adsorption of Ceramide to SH-SWCNTs by Probe-Tip Sonication: SH-SWCNTs (1 mg) and Ceramide (1 mg) were dispersed in 1X phosphate buffered saline (PBS) (500 μL, pH 7.4) and bath sonicated for 10 min at 25 ºC. The solution was then probe-tip sonicated with an ultrasonic processor (Cole Parmer) and a 3 mm stepped microtip probe with pulses of 3-7 W for 1 s followed by 2 s of rest for a total sonication time of 15 min. The solution was equilibrated for 1 h at 25 ºC then subsequently centrifuged at 16100 relative centrifugal force (RCF) for 30 min to remove unsuspended SWCNT aggregates. Suspended SWCNTs formed a homogeneous dark gray solution and were measured for concentration by UV-Vis-IR absorbance (Shimadzu UV-3600 Plus) with samples in a 100 μL volume, black-sided quartz cuvette (Thorlabs, Inc.). SWCNT concentration was calculated from absorbance at 632 nm using the Beer-Lambert law with extinction coefficient $\varepsilon_{632} = 0.036$ L mg^{-1} cm^{-1}.[38]

Corona Exchange Dynamics Assay for Protein-SWCNT Adsorption: Corona exchange dynamics studies were conducted as described previously.[58] Briefly, HRP, fibrinogen, and human serum albumin were labeled with a fluorophore (FAM) via N-hydroxysuccinimide ester conjugation (Lumiprobe). Protein (10 mg) in 1X PBS (900 μL) and an 8-fold molar excess of FAM-NHS in dimethyl sulfoxide (DMSO) (100 μL) were gently mixed via end-over-end rotation in a foil-covered tube for 4 h. FAM-protein conjugates were then purified with Zeba 2 mL spin desalting columns with 40 kDa MWCO (Thermo Scientific) to remove excess unreacted FAM-NHS according to manufacturer's instructions. The purified FAM-proteins were measured for concentration and degree of labeling via UV-Vis-IR absorbance at 280 nm for protein and 495 nm for FAM. The degree of labeling was calculated as the molar ratio of FAM to protein in the samples. 200 mg L^{-1} FAM fluorophore-labeled protein (25 μL) was added to 10 mg L^{-1} SH-SWCNTs dispersed with $(GT)_{15}$ ssDNA, C_{16}-PEG2k-Ceramide, and SC (25 μL) in triplicate. The solutions were combined via microchannel pipette in a 96-well PCR plate (Bio-Rad) and mixed by pipetting. The plate was sealed with an optically transparent adhesive seal and gently spun down in a benchtop centrifuge. Fluorescence time series measurements were obtained with a Bio-Rad CFX96 Real Time qPCR System by scanning the FAM channel every 30 s at 25 ºC.

SDS-PAGE of Cas9-SWCNT and Controls: SDS-PAGE was performed according to previously established protocols. Briefly, sample buffer was prepared by combining glycerol (2.5 mL), water (3.75 mL), 0.5 M Tris-HCl buffer pH 6.8 (1.25 mL), and 10% w/v SDS (2 mL). Gel running buffer was prepared with 10X Tris/Glycine/SDS Buffer (50 mL, Bio-Rad) and deionized water (450 mL). Sample (5 μL) was added to sample buffer (7.5 μL) and 6X loading dye (2.5 μL, New England Biosciences) and boiled at 95 ºC for 5 min. Samples were then loaded onto a 4-20% Mini-PROTEAN® TGX™ Precast Protein Gel (Bio-Rad) in a Mini-PROTEAN® Tetra Vertical Electrophorseis Cell (Bio-Rad) with running buffer according to manufacturer's instructions. Gel electrophoresis was run with a Mini-PROTEAN® PowerPac Basic Power Supply (Bio-Rad) at 200 V for 30 min. The finished gel was then stained with Coomassie Brilliant Blue (Thermo Scientific) for 1 hour, shaking gently. The gel was then de-stained overnight with 50% water, 40% methanol, 10% acetic acid (v/v/v) solution. The final gel was rehydrated in water and imaged according to manufacturer's instructions on a Typhoon FLA 9500 laser scanner (Cytiva) in digitization mode with a 532 nm excitation laser and a long-pass green filter. Gel images were processed with imageJ to adjust color contrast and image field of view.

Chapter 6: Conclusions and Future Outlook

The generation of covalent SWCNT-protein conjugates for nanosensor development has gained interest in recent years. One outstanding challenge in the development of SWCNT-based nanosensors lies in identifying suitable molecular recognition elements to provide analyte-selective modulation of SWCNT fluorescence. Direct attachment of protein-based molecular recognition agents would enable a design-based approach to nanosensor development so long as protein function and SWCNT intrinsic fluorescence can both be preserved. In this dissertation, we show that triazine-based SWCNT functionalization can be used to attach HRP enzymes to SWCNTs and demonstrate H_2O_2 sensing as a proof-of-principle demonstration of nanosensor functionality. To generate these sensors, we leveraged triazine-based SWCNT functionalization to attach free thiol groups to pristine SWCNTs while maintaining their optical properties. We determined that the resulting HRP-$(GT)_{15}$-SWCNT nanosensor showed a concentration-dependent turn-on fluorescence response to H_2O_2 in solution, partly due to the quenched SWCNT fluorescence baseline intensity after HRP conjugation. Fitting this response to a cooperative binding model produced estimated kinetic parameters including a solution-phase LOD of 31 μM. Though this value is above typical cellular ROS levels (100 nM-10 μM),[133] the nanosensor showed the ability to sense H_2O_2 when surface-immobilized on glass, presenting an alternate viable sensing form factor for effective H_2O_2 sensing in other systems with higher H_2O_2 levels such as contaminated water samples and food production.[72] In this form factor, the nanosensor showed robust analyte selectivity against similar analytes. Taken together, this study demonstrates the potential of covalent protein-SWCNT nanosensors for sensitive, specific, and stable analyte sensing.

The platform presented here also provides a workflow for assessing new protein candidates for SWCNT conjugation. By selecting proteins that are amenable to SMCC functionalization, are low enough in molecular weight for separation by spin-filtration, and exhibit minimal nonspecific adsorption to SWCNTs, researchers can confidently proceed with conjugate development via this platform. We demonstrated that ConA, Lysozyme, and WGA failed to meet these figures of merit, emphasizing the utility of HRP as a model protein and the use of this workflow for identifying amenable protein candidates.

Preliminary experiments demonstrate that our platform also enables the covalent conjugation of Cas9 to Cer-SWCNTs while maintaining DNA cleavage activity. However, further reaction condition optimization is necessary to maximize the preservation of Cas9 activity after conjugation to SWCNTs. Particularly, the SMCC:Cas9 ratio should be varied systematically and the resulting constructs should be assessed by QTOF-MS and an *in vitro* cleavage assay for singular functionalization and preserved enzymatic activity, respectively. Upon successful reaction optimization, the constructs could be applied for targeted gene editing in plant and animal systems. For proof of concept, Cas9-SWCNTs could be complexed with gRNA that targets a GFP gene expressed in human embryonic kidney (HEK-293) cells. Incubation of the resulting RNP-SWCNTs with HEK-293 cells should show decreased GFP fluorescence compared to RNP and SWCNT alone.[134] If successful, this would motivate studies for cellular delivery of other therapeutic proteins via covalent SWCNT conjugation such as cytokines for immunomodulation and cancer therapy.[135] Furthermore, Cas9-SWCNTs could be applied as selective DNA sensors since Cas9 undergoes large conformational shifts upon DNA binding, cleavage, and release, which

could selectively modulate SWCNT fluorescence emission by RNP's extreme selectivity for target DNA. Potential applications include disease diagnostics by sensing mutated/damaged DNA in cellular samples, infection monitoring by sensing bacterial, yeast, or viral DNA in cellular samples, and many others. If possible, this would accelerate the development of selective SWCNT-based DNA sensing for a multitude of point-of-care diagnostics.

The nanosensor synthesis platform developed here can also be extended to conjugate other proteins and enzymes of interest to generate robust nanosensors for other biologically relevant analytes. Orthogonally, since SWCNTs are also confirmed to be valuable as biomolecule delivery agents,[37,136–138] our conjugation work herein could enable facile protein conjugation to SWCNTs for protein delivery applications. The use of Sulfo-SMCC as the crosslinking agent allows any protein with exposed primary amines to be a candidate for conjugation to SH-SWCNTs. Additionally, the use of Triazine-SWCNT chemistry provides a wide library of available SWCNT functional groups like carboxylic acid (-COOH), primary amine ($-NH_2$), and biotin. These functionalized SWCNTs could thus be used with other crosslinker systems to conjugate proteins that are not amenable to maleimide functionalization via Sulfo-SMCC or otherwise require cargo release to achieve successful delivery. For example, delivery of protein cargo by SWCNT could be optimized with this platform by changing the crosslinker from a stable crosslinker in Sulfo-SMCC to a stimuli-responsive crosslinker such as the pH-sensitive hydrazone group for cargo release within the acidic endosome.[139] Corresponding conjugation functional groups must be added in the triazine substitution reaction to incorporate this responsive crosslinker. Additionally, proteins more amenable to EDC/NHS crosslinking could be conjugated to COOH-SWCNTs with this platform, widening the library of proteins available to generate nanosensors and deliver as cargo.

Other protein targets of interest that can be assessed by this platform are numerous. For example, galectin-3-binding protein could be attached to SWCNTs to detect elevated extracellular levels of galectin 3 for early venous thrombosis diagnosis.[140] Similarly, antibodies are proteins that selectively bind antigens with picomolar efficiency and have been used to enhance targeting of nanoparticles towards specific cell types.[141] Coupling the tissue-penetrative nIR fluorescence of SWCNT with covalently attached antibodies could enable both targeted tissue staining and enhanced cargo delivery. For example, the anti-ErbB2 antibody binds the HER2 receptor, which is overexpressed in certain breast cancer subtypes.[142,143] Anti-ErbB2-SWCNT constructs could enable *in vivo* breast cancer tumor staining for imaging and targeting of anticancer therapeutics toward these cells, improving their efficiency by mitigating off-target effects.

Additionally, other biomolecules could be conjugated to SWCNTs as alternative molecular recognition elements. For example, DNA aptamers are a class of synthetic biomolecules that can adsorb strongly to SWCNT surfaces and modulate SWCNT fluorescence in the presence of their target analyte. However, aptamers adsorbed on SWCNTs suffer from the same stability issues that proteins do, losing stability and thus sensitivity in complex biological environments.[144] Covalent conjugation of the terminal ends of DNA aptamers to triazine-functionalized SWCNTs could enable sensitive and stable fluorescence sensing of analytes such as serotonin, for example, whose altered levels are implicated in the neuropathology of several psychiatric disorders.[145]

While our approach for using covalent conjugation of enzymes to SWCNT could be generalizable for other enzymes and possibly also antibodies, we note that ensuring proper quality control of the nanosensor product is imperative for downstream use. For instance, commercially-procured enzymes and antibodies have been reported to have variable levels of activity, which could compromise the reproducibility of the nanosensor product.[146–150] Furthermore, proteins are also known to have variable levels of intrinsic affinity for the SWCNT surface.[151,152] Therefore, it is important to assess both the level of enzyme non-specific binding to the SWCNT surface and the level of enzymatic or binding activity of the final nanosensor product to ensure the response originates from covalently-attached proteins.[58] Ultimately, we anticipate that this conjugation platform could help advance the use of SWCNTs as nanomaterials for theranostics, delivery, and cellular fluorescence imaging purposes.

References

1. Sim, T. M., Tarini, D., Dheen, S. T., Bay, B. H. & Srinivasan, D. K. Nanoparticle-Based Technology Approaches to the Management of Neurological Disorders. *IJMS* **21**, 6070 (2020).
2. Holzinger, M., Le Goff, A. & Cosnier, S. Nanomaterials for biosensing applications: a review. *Front. Chem.* **2**, (2014).
3. Ramesh, M., Janani, R., Deepa, C. & Rajeshkumar, L. Nanotechnology-Enabled Biosensors: A Review of Fundamentals, Design Principles, Materials, and Applications. *Biosensors* **13**, 40 (2022).
4. Ghosh, T., Raj, G. V. S. B. & Dash, K. K. A comprehensive review on nanotechnology based sensors for monitoring quality and shelf life of food products. *Measurement: Food* **7**, 100049 (2022).
5. Ledesma, F., Ozcan, B., Sun, X., Medina, S. M. & Landry, M. P. Nanomaterial Strategies for Delivery of Therapeutic Cargoes. *Adv Funct Materials* **32**, 2107174 (2022).
6. Maghsoudnia, N., Eftekhari, R. B., Sohi, A. N., Zamzami, A. & Dorkoosh, F. A. Application of nano-based systems for drug delivery and targeting: a review. *J Nanopart Res* **22**, 245 (2020).
7. Mitchell, M. J. *et al.* Engineering precision nanoparticles for drug delivery. *Nat Rev Drug Discov* (2020) doi:10.1038/s41573-020-0090-8.
8. Zhang, C. *et al.* Co-delivery of paclitaxel and survivin siRNA with cationic liposome for lung cancer therapy. *Colloids and Surfaces A: Physicochemical and Engineering Aspects* **585**, 124054 (2020).

9. Singh, A., Neupane, Y. R., Shafi, S., Mangla, B. & Kohli, K. PEGylated liposomes as an emerging therapeutic platform for oral nanomedicine in cancer therapy: in vitro and in vivo assessment. *Journal of Molecular Liquids* **303**, 112649 (2020).

10. Lee, E.-H., Lim, S.-J. & Lee, M.-K. Chitosan-coated liposomes to stabilize and enhance transdermal delivery of indocyanine green for photodynamic therapy of melanoma. *Carbohydrate Polymers* **224**, 115143 (2019).

11. Samaridou, E., Heyes, J. & Lutwyche, P. Lipid nanoparticles for nucleic acid delivery: Current perspectives. *Advanced Drug Delivery Reviews* **154–155**, 37–63 (2020).

12. Han, X., Mitchell, M. J. & Nie, G. Nanomaterials for Therapeutic RNA Delivery. *Matter* **3**, 1948–1975 (2020).

13. Billingsley, M. M. *et al.* Ionizable Lipid Nanoparticle-Mediated mRNA Delivery for Human CAR T Cell Engineering. *Nano Lett.* **20**, 1578–1589 (2020).

14. Ball, R. L., Hajj, K. A., Vizelman, J., Bajaj, P. & Whitehead, K. A. Lipid Nanoparticle Formulations for Enhanced Co-delivery of siRNA and mRNA. *Nano Lett.* **18**, 3814–3822 (2018).

15. Hajj, K. A. *et al.* A Potent Branched-Tail Lipid Nanoparticle Enables Multiplexed mRNA Delivery and Gene Editing *In Vivo*. *Nano Lett.* **20**, 5167–5175 (2020).

16. Luan, X. *et al.* Engineering exosomes as refined biological nanoplatforms for drug delivery. *Acta Pharmacol Sin* **38**, 754–763 (2017).

17. Haney, M. J. *et al.* Exosomes as drug delivery vehicles for Parkinson's disease therapy. *Journal of Controlled Release* **207**, 18–30 (2015).

18. Li, X. *et al.* Challenges and opportunities in exosome research—Perspectives from biology, engineering, and cancer therapy. *APL Bioeng* **3**, (2019).

19. Karlsson, J., Vaughan, H. J. & Green, J. J. Biodegradable Polymeric Nanoparticles for Therapeutic Cancer Treatments. *Annual Review of Chemical and Biomolecular Engineering* **9**, 105–127 (2018).

20. Calzoni, E. *et al.* Biocompatible Polymer Nanoparticles for Drug Delivery Applications in Cancer and Neurodegenerative Disorder Therapies. *JFB* **10**, 4 (2019).

21. Garg, U., Chauhan, S., Nagaich, U. & Jain, N. Current Advances in Chitosan Nanoparticles Based Drug Delivery and Targeting. *Adv Pharm Bull* **9**, 195–204 (2019).

22. Ehlerding, E. B., Chen, F. & Cai, W. Biodegradable and Renal Clearable Inorganic Nanoparticles. *Advanced Science* **3**, 1500223 (2016).

23. Anselmo, A. C. & Mitragotri, S. A Review of Clinical Translation of Inorganic Nanoparticles. *AAPS J* **17**, 1041–1054 (2015).

24. Arias, L. S. *et al.* Iron Oxide Nanoparticles for Biomedical Applications: A Perspective on Synthesis, Drugs, Antimicrobial Activity, and Toxicity. *Antibiotics* **7**, 46 (2018).

25. Stephen, S., Gorain, B., Choudhury, H. & Chatterjee, B. Exploring the role of mesoporous silica nanoparticle in the development of novel drug delivery systems. *Drug Deliv. and Transl. Res.* (2021) doi:10.1007/s13346-021-00935-4.

26. Zhou, H. *et al.* Biodegradable Inorganic Nanoparticles for Cancer Theranostics: Insights into the Degradation Behavior. *Bioconjugate Chem.* **31**, 315–331 (2020).

27. Han, S., Bouchard, R. & Sokolov, K. V. Molecular photoacoustic imaging with ultra-small gold nanoparticles. *Biomed. Opt. Express, BOE* **10**, 3472–3483 (2019).

28. Gunduz, N., Ceylan, H., Guler, M. O. & Tekinay, A. B. Intracellular Accumulation of Gold Nanoparticles Leads to Inhibition of Macropinocytosis to Reduce the Endoplasmic Reticulum Stress. *Scientific Reports* **7**, 40493 (2017).

29. Sun, Y. *et al.* Metal–Organic Framework Nanocarriers for Drug Delivery in Biomedical Applications. *Nano-Micro Lett.* **12**, 103 (2020).

30. Simon-Yarza, T., Mielcarek, A., Couvreur, P. & Serre, C. Nanoparticles of Metal-Organic Frameworks: On the Road to In Vivo Efficacy in Biomedicine. *Advanced Materials* **30**, 1707365 (2018).

31. Bilan, R., Nabiev, I. & Sukhanova, A. Quantum Dot-Based Nanotools for Bioimaging, Diagnostics, and Drug Delivery. *ChemBioChem* **17**, 2103–2114 (2016).

32. Chibh, S., Mishra, J., Kour, A., Chauhan, V. S. & Panda, J. J. Recent advances in the fabrication and bio-medical applications of self-assembled dipeptide nanostructures. *Nanomedicine* nnm-2020-0314 (2021) doi:10.2217/nnm-2020-0314.

33. Boghossian, A. A. *et al.* Near-Infrared Fluorescent Sensors based on Single-Walled Carbon Nanotubes for Life Sciences Applications. *ChemSusChem* **4**, 848–863 (2011).

34. Liu, Z., Tabakman, S., Welsher, K. & Dai, H. Carbon nanotubes in biology and medicine: In vitro and in vivo detection, imaging and drug delivery. *Nano Res.* **2**, 85–120 (2009).

35. Iijima, S. & Ichihashi, T. Single-shell carbon nanotubes of 1-nm diameter. *Nature* **363**, 603–605 (1993).

36. Demirer, G. S. *et al.* High aspect ratio nanomaterials enable delivery of functional genetic material without DNA integration in mature plants. *Nat. Nanotechnol.* **14**, 456–464 (2019).

37. Demirer, G. S. *et al.* Carbon nanocarriers deliver siRNA to intact plant cells for efficient gene knockdown. *Sci. Adv.* **6**, eaaz0495 (2020).

38. Bonis-O'Donnell, J. T. D. *et al.* Dual Near-Infrared Two-Photon Microscopy for Deep-Tissue Dopamine Nanosensor Imaging. *Adv. Funct. Mater.* **27**, 1702112 (2017).

39. Bisker, G. *et al.* Insulin Detection Using a Corona Phase Molecular Recognition Site on Single-Walled Carbon Nanotubes. *ACS Sens.* **3**, 367–377 (2018).

40. Pinals, R. L. *et al.* Rapid SARS-CoV-2 Spike Protein Detection by Carbon Nanotube-Based Near-Infrared Nanosensors. *Nano Lett.* **21**, 2272–2280 (2021).

41. Dresselhaus, M. S., Dresselhaus, G. & Saito, R. Physics of carbon nanotubes. *Carbon* **33**, 883–891 (1995).

42. Bachilo, S. M. *et al.* Structure-Assigned Optical Spectra of Single-Walled Carbon Nanotubes. *Science* **298**, 2361–2366 (2002).

43. Jorio, A. *et al.* Carbon Nanotube Photophysics. *MRS BULLETIN* (2004).

44. Dresselhaus, M. S., Dresselhaus, G., Saito, R. & Jorio, A. Exciton Photophysics of Carbon Nanotubes. *Annu. Rev. Phys. Chem.* **58**, 719–747 (2007).

45. Kruss, S. *et al.* Neurotransmitter Detection Using Corona Phase Molecular Recognition on Fluorescent Single-Walled Carbon Nanotube Sensors. *J. Am. Chem. Soc.* **136**, 713–724 (2014).

46. Jeong, S. *et al.* High-throughput evolution of near-infrared serotonin nanosensors. *SCIENCE ADVANCES* **5**, (2019).

47. O'Connell, M. J. *et al.* Band Gap Fluorescence from Individual Single-Walled Carbon Nanotubes. *Science* **297**, 593–596 (2002).

48. Frangioni, J. In vivo near-infrared fluorescence imaging. *Current Opinion in Chemical Biology* **7**, 626–634 (2003).

49. Zhang, J. *et al.* Molecular recognition using corona phase complexes made of synthetic polymers adsorbed on carbon nanotubes. *Nature Nanotech* **8**, 959–968 (2013).

50. Ackermann, J., Metternich, J. T., Herbertz, S. & Kruss, S. Biosensing with Fluorescent Carbon Nanotubes. *Angew Chem Int Ed* **61**, (2022).

51. Bisker, G. *et al.* Protein-targeted corona phase molecular recognition. *Nat Commun* **7**, 10241 (2016).

52. Chio, L. *et al.* Electrostatic Assemblies of Single-Walled Carbon Nanotubes and Sequence-Tunable Peptoid Polymers Detect a Lectin Protein and Its Target Sugars. *Nano Lett.* **19**, 7563–7572 (2019).

53. Antonucci, A., Kupis-Rozmysłowicz, J. & Boghossian, A. A. Noncovalent Protein and Peptide Functionalization of Single-Walled Carbon Nanotubes for Biodelivery and Optical Sensing Applications. *ACS Appl. Mater. Interfaces* **9**, 11321–11331 (2017).

54. Barone, P. W., Baik, S., Heller, D. A. & Strano, M. S. Near-infrared optical sensors based on single-walled carbon nanotubes. *Nature Mater* **4**, 86–92 (2005).

55. Karajanagi, S. S., Vertegel, A. A., Kane, R. S. & Dordick, J. S. Structure and Function of Enzymes Adsorbed onto Single-Walled Carbon Nanotubes. *Langmuir* **20**, 11594–11599 (2004).

56. Matsuura, K. *et al.* Selectivity of water-soluble proteins in single-walled carbon nanotube dispersions. *Chemical Physics Letters* **429**, 497–502 (2006).

57. Graff, R. A. *et al.* Achieving Individual-Nanotube Dispersion at High Loading in Single-Walled Carbon Nanotube Composites. *Adv. Mater.* **17**, 980–984 (2005).

58. Pinals, R. L., Yang, D., Lui, A., Cao, W. & Landry, M. P. Corona Exchange Dynamics on Carbon Nanotubes by Multiplexed Fluorescence Monitoring. *J. Am. Chem. Soc.* **142**, 1254–1264 (2020).

59. Palwai, N. R. *et al.* Retention of biological activity and near-infrared absorbance upon adsorption of horseradish peroxidase on single-walled carbon nanotubes. *Nanotechnology* **18**, 235601 (2007).

60. Noor, M. M., Goswami, J. & Davis, V. A. Comparison of Attachment and Antibacterial Activity of Covalent and Noncovalent Lysozyme-Functionalized Single-Walled Carbon Nanotubes. *ACS Omega* **5**, 2254–2259 (2020).

61. Kruss, S. *et al.* Carbon nanotubes as optical biomedical sensors. *Advanced Drug Delivery Reviews* **65**, 1933–1950 (2013).

62. Hirsch, A. Functionalization of Single-Walled Carbon Nanotubes. *Angew. Chem. Int. Ed.* **41**, 1853 (2002).

63. Cognet, L. *et al.* Stepwise Quenching of Exciton Fluorescence in Carbon Nanotubes by Single-Molecule Reactions. *Science* **316**, 1465–1468 (2007).

64. Ghosh, S., Bachilo, S. M., Simonette, R. A., Beckingham, K. M. & Weisman, R. B. Oxygen Doping Modifies Near-Infrared Band Gaps in Fluorescent Single-Walled Carbon Nanotubes. *Science* **330**, 1656–1659 (2010).

65. Piao, Y. *et al.* Brightening of carbon nanotube photoluminescence through the incorporation of sp3 defects. *Nature Chem* **5**, 840–845 (2013).

66. Mann, F. A., Herrmann, N., Opazo, F. & Kruss, S. Quantum Defects as a Toolbox for the Covalent Functionalization of Carbon Nanotubes with Peptides and Proteins. *Angew. Chem. Int. Ed.* **59**, 17732–17738 (2020).

67. Mann, F. A., Galonska, P., Herrmann, N. & Kruss, S. Quantum defects as versatile anchors for carbon nanotube functionalization. *Nat Protoc* **17**, 727–747 (2022).

68. Setaro, A. *et al.* Preserving π-conjugation in covalently functionalized carbon nanotubes for optoelectronic applications. *Nat Commun* **8**, 14281 (2017).

69. Godin, A. G. *et al.* Photoswitchable single-walled carbon nanotubes for super-resolution microscopy in the near-infrared. *Sci. Adv.* **5**, eaax1166 (2019).

70. Chio, L., Pinals, R. L., Murali, A., Goh, N. S. & Landry, M. P. Covalent Surface Modification Effects on Single-Walled Carbon Nanotubes for Targeted Sensing and Optical Imaging. *Adv. Funct. Mater.* **30**, 1910556 (2020).

71. Woolley, J. F., Stanicka, J. & Cotter, T. G. Recent advances in reactive oxygen species measurement in biological systems. *Trends in Biochemical Sciences* **38**, 556–565 (2013).

72. Giaretta, J. E. *et al.* Flexible Sensors for Hydrogen Peroxide Detection: A Critical Review. *ACS Appl. Mater. Interfaces* **14**, 20491–20505 (2022).

73. Gajhede, M., Schuller, D. J., Henriksen, A., Smith, A. T. & Poulos, T. L. Crystal structure of horseradish peroxidase C at 2.15 Å resolution. *Nat Struct Mol Biol* **4**, 1032–1038 (1997).

74. O'Brien, A. M., Ó'Fágáin, C., Nielsen, P. F. & Welinder, K. G. Location of crosslinks in chemically stabilized horseradish peroxidase: Implications for design of crosslinks. *Biotechnol. Bioeng.* **76**, 277–284 (2001).

75. Nishitani, S., Tran, T., Puglise, A., Yang, S. & Landry, M. P. Engineered Glucose Oxidase-Carbon Nanotube Conjugates for Tissue-Translatable Glucose Nanosensors. *Angewandte Chemie* e202311476 (2023) doi:10.1002/ange.202311476.

76. Lew, T. T. S. *et al.* Real-time detection of wound-induced H2O2 signalling waves in plants with optical nanosensors. *Nat. Plants* **6**, 404–415 (2020).

77. Heller, D. A. *et al.* Peptide secondary structure modulates single-walled carbon nanotube fluorescence as a chaperone sensor for nitroaromatics. *Proceedings of the National Academy of Sciences* **108**, 8544–8549 (2011).

78. Brege, J. J., Gallaway, C. & Barron, A. R. Fluorescence Quenching of Single-Walled Carbon Nanotubes in SDBS Surfactant Suspension by Metal Ions: Quenching Efficiency as a Function of Metal and Nanotube Identity. *J. Phys. Chem. C* **111**, 17812–17820 (2007).

79. Horoszko, C. P. *et al.* Non-Covalent Coatings on Carbon Nanotubes Mediate Photosensitizer Interactions. *ACS Appl. Mater. Interfaces* **13**, 51343–51350 (2021).

80. Welinder, K. G. Amino Acid Sequence Studies of Horseradish Peroxidase: Amino and Carboxyl Termini, Cyanogen Bromide and Tryptic Fragments, the Complete Sequence, and Some Structural Characteristics of Horseradish Peroxidase C. *European Journal of Biochemistry* **96**, 483–502 (1979).

81. Kessler, A. *et al.* Adsorption of Horseradish Peroxidase on Metallic Nanoparticles: Effects on Reactive Oxygen Species Detection Using 2′,7′-Dichlorofluorescin Diacetate. *Chem. Res. Toxicol.* **34**, 1481–1495 (2021).

82. Ivanov, Yu. D. *et al.* Irreversible chemical AFM-based fishing for detection of low-copied proteins. *Biochem. Moscow Suppl. Ser. B* **7**, 46–61 (2013).

83. Ivanov, Y. D. *et al.* Investigation of the Influence of Liquid Motion in a Flow-based System on an Enzyme Aggregation State with an Atomic Force Microscopy Sensor: The Effect of Water Flow. *Applied Sciences* **10**, 4560 (2020).

84. Zhu, H., Jia, Z., Trush, M. & Li, Y. R. A Highly Sensitive Chemiluminometric Assay for Real-Time Detection of Biological Hydrogen Peroxide Formation. *ROS* 216–227 (2016) doi:10.20455/ros.2016.841.

85. Sariri, R., Sajedi, R. H. & Jafarian, V. Inhibition of horseradish peroxidase activity by thiol type inhibitors. *Journal of Molecular Liquids* **123**, 20–23 (2006).

86. Ochoe de Aspuru, E. & Lourdes Zatón, A. M. Effect of glutathione on horseradish peroxidase activity. *Spectrochimica Acta Part A: Molecular and Biomolecular Spectroscopy* **55**, 2343–2346 (1999).

87. Heck, D. E., Shakarjian, M., Kim, H. D., Laskin, J. D. & Vetrano, A. M. Mechanisms of oxidant generation by catalase. *Annals of the New York Academy of Sciences* **1203**, 120–125 (2010).

88. Rodríguez-López, J. N. *et al.* Mechanism of Reaction of Hydrogen Peroxide with Horseradish Peroxidase: Identification of Intermediates in the Catalytic Cycle. *J. Am. Chem. Soc.* **123**, 11838–11847 (2001).

89. Bollella, P. *et al.* Highly sensitive, stable and selective hydrogen peroxide amperometric biosensors based on peroxidases from different sources wired by Os-polymer: A comparative study. *Solid State Ionics* **314**, 178–186 (2018).

90. Ruan, C., Yang, F., Lei, C. & Deng, J. Thionine Covalently Tethered to Multilayer Horseradish Peroxidase in a Self-Assembled Monolayer as an Electron-Transfer Mediator. *Anal. Chem.* **70**, 1721–1725 (1998).

91. Kruusma, J., Sammelselg, V. & Banks, C. E. A systematic study of the electrochemical determination of hydrogen peroxide at single-walled carbon nanotube ensemble networks. *Electrochemistry Communications* **10**, 1872–1875 (2008).

92. Navas Díaz, A., Ramos Peinado, M. C. & Torijas Minguez, M. C. Sol–gel horseradish peroxidase biosensor for hydrogen peroxide detection by chemiluminescence. *Analytica Chimica Acta* **363**, 221–227 (1998).

93. Jiao, L. *et al.* Fe–N–C Single-Atom Nanozymes for the Intracellular Hydrogen Peroxide Detection. *Anal. Chem.* **91**, 11994–11999 (2019).

94. Qian, P. *et al.* A hierarchical cobalt/carbon nanotube hybrid nanocomplex-based ratiometric fluorescent nanosensor for ultrasensitive detection of hydrogen peroxide and glucose in human serum. *Anal Bioanal Chem* **411**, 1517–1524 (2019).

95. Tagad, C. K. *et al.* Green synthesis of silver nanoparticles and their application for the development of optical fiber based hydrogen peroxide sensor. *Sensors and Actuators B: Chemical* **183**, 144–149 (2013).

96. Kimura, M., Umemoto, Y. & Kawano, T. Hydrogen peroxide-independent generation of superoxide by plant peroxidase: hypotheses and supportive data employing ferrous ion as a model stimulus. *Front. Plant Sci.* **5**, (2014).

97. Metodiewa, D. & Dunford, H. B. The reactions of horseradish peroxidase, lactoperoxidase, and myeloperoxidase with enzymatically generated superoxide. *Archives of Biochemistry and Biophysics* **272**, 245–253 (1989).

98. Bauduin, P. *et al.* Hofmeister specific-ion effects on enzyme activity and buffer pH: Horseradish peroxidase in citrate buffer. *Journal of Molecular Liquids* **123**, 14–19 (2006).

99. Bhandari, A., Kim, W. & Hohn, K. Luminol-Based Enhanced Chemiluminescence Assay for Quantification of Peroxidase and Hydrogen Peroxide in Aqueous Solutions: Effect of Reagent pH and Ionic Strength. *J. Environ. Eng.* **136**, 1147–1152 (2010).

100. Sun, W., Ji, X., Kricka, L. J. & Dunford, H. B. Rate constants for reactions of horseradish peroxidase compounds I and II with 4-substituted arylboronic acids. *Can. J. Chem.* **72**, 2159–2162 (1994).

101. Morales-Urrea, D., López-Córdoba, A. & Contreras, E. M. Inactivation kinetics of horseradish peroxidase (HRP) by hydrogen peroxide. *Sci Rep* **13**, 13363 (2023).

102. Nazari, K., Mahmoudi, A., Shahrooz, M., Khodafarin, R. & Moosavi-Movahedi, A. A. Suicide-peroxide inactivation of horseradish peroxidase in the presence of *Sodium n-Dodecyl Sulphate* : A study of the enzyme deactivation kinetics. *Journal of Enzyme Inhibition and Medicinal Chemistry* **20**, 285–292 (2005).

103. Vlasits, J. *et al.* Mechanisms of catalase activity of heme peroxidases. *Archives of Biochemistry and Biophysics* **500**, 74–81 (2010).

104. Hernández-Ruiz, J., Arnao, M. B., Hiner, A. N. P., García-Cánovas, F. & Acosta, M. Catalase-like activity of horseradish peroxidase: relationship to enzyme inactivation by H2O2. *Biochemical Journal* **354**, 107–114 (2001).

105. Mao, L., Luo, S., Huang, Q. & Lu, J. Horseradish Peroxidase Inactivation: Heme Destruction and Influence of Polyethylene Glycol. *Sci Rep* **3**, 3126 (2013).

106. Han, S., Cui, Y. & Helbing, D. L. Inactivation of Horseradish Peroxidase by Acid for Sequential Chemiluminescent Western Blot. *Biotechnology Journal* **15**, 1900397 (2020).

107. Orlova, M. A. *et al.* Comparative study of the inactivation of horseradish peroxidase under the effect of H202 and ionizing radiation. *Russ. Chem.Bull.* **44**, (1995).

108. Baynton, K. J., Bewtra, J. K., Biswas, N. & Taylor, K. E. Inactivation of horseradish peroxidase by phenol and hydrogen peroxide: a kinetic investigation. *Biochimica et Biophysica Acta (BBA) - Protein Structure and Molecular Enzymology* **1206**, 272–278 (1994).

109. Nakajima, R. & Yamazaki, I. The mechanism of oxyperoxidase formation from ferryl peroxidase and hydrogen peroxide. *Journal of Biological Chemistry* **262**, 2576–2581 (1987).

110. Malomo, S. O. *et al.* Suicide inactivation of horseradish peroxidase by excess hydrogen peroxide: The effects of reaction pH, buffer ion concentration, and redox mediation. *Biokemistri* **23**, 124–128 (2011).

111. Kawano, T., Muto, S., Adachi, M., Hosoya, H. & Lapeyrie, F. Spectroscopic Evidence in Support of Horseradish Peroxidase Compound II-catalyzed Oxidation of Salicylic Acid but Not of Phenylethylamine. *Bioscience, Biotechnology, and Biochemistry* **66**, 651–654 (2002).

112. Kawano, T., Muto, S., Adachi, M., Hosoya, H. & Lapeyrie, F. Spectroscopic Evidence That Salicylic Acid Converts a Temporally Inactivated Form of Horseradish Peroxidase (Compound III) to the Irreversibly Inactivated Verdohemoprotein (P-670). *Bioscience, Biotechnology, and Biochemistry* **66**, 646–650 (2002).

113. Chamchoy, K., Pakotiprapha, D., Pumirat, P., Leartsakulpanich, U. & Boonyuen, U. Application of WST-8 based colorimetric NAD(P)H detection for quantitative dehydrogenase assays. *BMC Biochem* **20**, 4 (2019).

114. Steenken, S. & Jovanovic, S. V. How Easily Oxidizable Is DNA? One-Electron Reduction Potentials of Adenosine and Guanosine Radicals in Aqueous Solution. *J. Am. Chem. Soc.* **119**, 617–618 (1997).

115. Moosavi-Movahedi, A. A., Nazari, K. & Saboury, A. A. Thermodynamics of denaturation of horseradish peroxidase with sodium n-dodecyl sulphate and n-dodecyl trimethylammonium bromide. *Colloids and Surfaces B: Biointerfaces* **9**, 123–130 (1997).

116. Hardman, K. D. & Ainsworth, C. F. Structure of concanavalin A at 2.4-Ang resolution. *Biochemistry* **11**, 4910–4919 (1972).

117. Ballerstadt, R., Evans, C., McNichols, R. & Gowda, A. Concanavalin A for in vivo glucose sensing: A biotoxicity review. *Biosensors and Bioelectronics* **22**, 275–284 (2006).

118. Bercea, M. & Lupu, A. Recent Insights into Glucose-Responsive Concanavalin A-Based Smart Hydrogels for Controlled Insulin Delivery. *Gels* **10**, 260 (2024).

119. Russell, R. J., Pishko, M. V., Gefrides, C. C., McShane, M. J. & Coté, G. L. A Fluorescence-Based Glucose Biosensor Using Concanavalin A and Dextran Encapsulated in a Poly(ethylene glycol) Hydrogel. *Anal. Chem.* **71**, 3126–3132 (1999).

120. Locke, A. K., Cummins, B. M., Abraham, A. A. & Coté, G. L. PEGylation of Concanavalin A to Improve Its Stability for an *In Vivo* Glucose Sensing Assay. *Anal. Chem.* **86**, 9091–9097 (2014).

121. Ferraboschi, P., Ciceri, S. & Grisenti, P. Applications of Lysozyme, an Innate Immune Defense Factor, as an Alternative Antibiotic. *Antibiotics* **10**, 1534 (2021).

122. Wu, T. *et al.* Formation of hydrogels based on chitosan/alginate for the delivery of lysozyme and their antibacterial activity. *Food Chemistry* **240**, 361–369 (2018).

123. Wu, T. *et al.* Integration of lysozyme into chitosan nanoparticles for improving antibacterial activity. *Carbohydrate Polymers* **155**, 192–200 (2017).

124. Monsigny, M., Roche, A., Sene, C., Maget-Dana, R. & Delmotte, F. Sugar-Lectin Interactions: How Does Wheat-Germ Agglutinin Bind Sialoglycoconjugates? *European Journal of Biochemistry* **104**, 147–153 (1980).

125. Ryva, B. *et al.* Wheat Germ Agglutinin as a Potential Therapeutic Agent for Leukemia. *Front. Oncol.* **9**, 100 (2019).

126. Balčiūnaitė-Murzienė, G. & Dzikaras, M. Wheat Germ Agglutinin—From Toxicity to Biomedical Applications. *Applied Sciences* **11**, 884 (2021).

127. Nagata, Y. & Burger, M. M. Wheat Germ Agglutinin. *Journal of Biological Chemistry* **247**, 2248–2250 (1972).

128. Cheng, Q. *et al.* CRISPR/Cas9 ribonucleoprotein (RNP) complex enables higher viability of transfected cells in genome editing of acute myeloid cells. *Ann Transl Med* **10**, 862–862 (2022).

129. Zhang, S., Shen, J., Li, D. & Cheng, Y. Strategies in the delivery of Cas9 ribonucleoprotein for CRISPR/Cas9 genome editing. *Theranostics* **11**, 614–648 (2021).

130. Duan, L. *et al.* Nanoparticle Delivery of CRISPR/Cas9 for Genome Editing. *Front. Genet.* **12**, 673286 (2021).

131. Mout, R. *et al.* Direct Cytosolic Delivery of CRISPR/Cas9-Ribonucleoprotein for Efficient Gene Editing. *ACS Nano* **11**, 2452–2458 (2017).

132. Hemphill, J., Borchardt, E. K., Brown, K., Asokan, A. & Deiters, A. Optical Control of CRISPR/Cas9 Gene Editing. *J. Am. Chem. Soc.* **137**, 5642–5645 (2015).

133. Giorgio, M., Trinei, M., Migliaccio, E. & Pelicci, P. G. Hydrogen peroxide: a metabolic by-product or a common mediator of ageing signals? *Nat Rev Mol Cell Biol* **8**, 722–728 (2007).

134. Rui, Y. *et al.* Carboxylated branched poly(β-amino ester) nanoparticles enable robust cytosolic protein delivery and CRISPR-Cas9 gene editing. *Sci. Adv.* **5**, eaay3255 (2019).

135. Gonçalves, A., Machado, R., Gomes, A. C. & Costa, A. da. Nanotechnology Solutions for Controlled Cytokine Delivery: An Applied Perspective. *Applied Sciences* **10**, 7098 (2020).

136. Zare, H. *et al.* Carbon Nanotubes: Smart Drug/Gene Delivery Carriers. *IJN* **Volume 16**, 1681–1706 (2021).

137. Demirer, G. S. *et al.* High aspect ratio nanomaterials enable delivery of functional genetic material without DNA integration in mature plants. *Nat. Nanotechnol.* **14**, 456–464 (2019).

138. Chen, J. *et al.* Functionalized Single-Walled Carbon Nanotubes as Rationally Designed Vehicles for Tumor-Targeted Drug Delivery. *J. Am. Chem. Soc.* **130**, 16778–16785 (2008).

139. Pinals, R. L., Chio, L., Ledesma, F. & Landry, M. P. Engineering at the nano-bio interface: harnessing the protein corona towards nanoparticle design and function. *Analyst* **145**, 5090–5112 (2020).

140. DeRoo, E. P. *et al.* The role of galectin-3 and galectin-3–binding protein in venous thrombosis. *Blood* **125**, 1813–1821 (2015).

141. Pinals, R. L., Chio, L., Ledesma, F. & Landry, M. P. Engineering at the nano-bio interface: harnessing the protein corona towards nanoparticle design and function. 23 (2020).

142. Mitri, Z., Constantine, T. & O'Regan, R. The HER2 Receptor in Breast Cancer: Pathophysiology, Clinical Use, and New Advances in Therapy. *Chemotherapy Research and Practice* **2012**, 1–7 (2012).

143. Shukla, R. *et al.* HER2 Specific Tumor Targeting with Dendrimer Conjugated Anti-HER2 mAb. *Bioconjugate Chem.* **17**, 1109–1115 (2006).

144. Lee, K., Nojoomi, A., Jeon, J., Lee, C. Y. & Yum, K. Near-Infrared Fluorescence Modulation of Refolded DNA Aptamer-Functionalized Single-Walled Carbon Nanotubes for Optical Sensing. *ACS Appl. Nano Mater.* **1**, 5327–5336 (2018).

145. Nakatsuka, N. *et al.* Sensing serotonin secreted from human serotonergic neurons using aptamer-modified nanopipettes. *Mol Psychiatry* (2021) doi:10.1038/s41380-021-01066-5.

146. Scott, J. E. & Williams, K. P. Validating Identity, Mass Purity and Enzymatic Purity of Enzyme Preparations. in *Assay Guidance Manual* (eds. Markossian, S. et al.) (Eli Lilly & Company and the National Center for Advancing Translational Sciences, Bethesda (MD), 2004).

147. Rosalki, S. B. Quality Control of Enzyme Determinations. *Ann Clin Biochem* **17**, 74–77 (1980).

148. Brandariz-Fontes, C. *et al.* Effect of the enzyme and PCR conditions on the quality of high-throughput DNA sequencing results. *Sci Rep* **5**, 8056 (2015).

149. Acharya, P., Quinlan, A. & Neumeister, V. The ABCs of finding a good antibody: How to find a good antibody, validate it, and publish meaningful data. *F1000Res* **6**, 851 (2017).

150. Luo, Y. *et al.* Lot-to-Lot Variance in Immunoassays—Causes, Consequences, and Solutions. *Diagnostics* **13**, 1835 (2023).

151. Pinals, R. L. *et al.* Quantitative Protein Corona Composition and Dynamics on Carbon Nanotubes in Biological Environments. *Angew Chem Int Ed* **59**, 23668–23677 (2020).

152. Ouassil, N., Pinals, R. L., Del Bonis-O'Donnell, J. T., Wang, J. W. & Landry, M. P. Supervised learning model predicts protein adsorption to carbon nanotubes. *Sci. Adv.* **8**, eabm0898 (2022).